Dynamics and structural complexity of framework materials

Quentin Guéroult

Balliol College

A thesis submitted to the University of Oxford
for the degree of Doctor of Philosophy

Supervisors: Prof. Andrew L. Goodwin and Prof. Volker L. Deringer

Inorganic Chemistry Laboratory
University of Oxford

June 2025

Declaration

The work presented in this thesis was carried out beween October 2021 and June 2025 in the Inorganic Chemistry Laboratory, University of Oxford, under the joint supervision of Prof. Andrew L. Goodwin and Prof. Volker L. Deringer. This dissertation is the result of my own work, and where it draws on the work of others, this is acknowledged at appropriate points in the text. This dissertation has not been submitted in whole or in part for a degree at this or any other institution.

Quentin Guéroult

Abstract

This thesis aims to understand the key phonon modes and chemical interactions that drive phase transitions and thermal expansion in a series of relatively simple inorganic solids. Coarse-graining and thermal diffuse scattering are used to help rationalise the key interactions involved. There are five studies.

The first uses a combination of DFT phonon calculations, inelastic neutron scattering and thermal diffuse scattering to probe the low-energy dynamics of $Rb_2Zn(CN)_4$ and $K_2Zn(CN)_4$. The A-site (Rb^+ and K^+) pyrochlore sublattice is shown to play an important role in the dynamics of these systems.

The second concerns dicalcium barium propionate and the origin of its diffuse scattering. Dicalcium barium propionate has a complex structure that makes *ab initio* phonon calculations intractable. Parallels are drawn between its underlying $Ba(Ca)_2$ framework and SiO_2 cristobalite to build a coarse-grained model. Molecular dynamics simulations are then used to understand the nature of the diffuse scattering of dicalcium barium propionate.

The third addresses the negative thermal expansion behaviour of $Zn(CN)_2$ and $Cd(CN)_2$. A combination of neutron total scattering measurements and *ab initio* phonon calculations are used to reassess the microscopic origin that drives the dominant lattice dynamics. A simple, coarse-grained model turns out to capture the key negative thermal expansion behaviour of $M(CN)_2$, especially at low temperatures.

The fourth investigates whether an automated, coarse-grained approach can capture the low-energy dynamics of framework materials in more general terms. Its effectiveness is then discussed for a variety of chemically-different framework materials namely: MOF-5, $[NH_4][Zn(HCOO)_3]$ and $Zn(CN)_2$.

The fifth tackles the disordered stacking arrangement of $Ni(CN)_2$. An interlayer potential that encodes the effective interactions between layers is derived. The stacking behaviour of $Ni(CN)_2$ is then re-cast as a pseudo-spin model. Monte Carlo simulations at different temperatures are then run, and the final configurations directly compared to experiment.

Acknowledgements

A tremendous thank you to both my supervisors, Andrew Goodwin and Volker Deringer for receiving me into their groups. I have been extremely fortunate to work in such a rewarding field and in such a positive environment, with extremely bright and considerate people.

Particular thanks to past and present Goodwin group members. Arianna and Nikolaj showed extraordinary patience with my questions during my first few months in our shared office; Emily, John, Johny and Tom expertly set the example on how to pursue a DPhil; Johny—your joie de vivre made our beamtimes and syntheses always entertaining; Tom—your kindness and calmness are an inspiration. From a brief postdoc hiatus to four: Hunter, Nim, Theo and Tristan—our numerous coffees have been delightful. A particular merci to Hunter for proof reading the initial drafts of the results chapters. Elodie—your aesthetic eye is unparalleled, I hope a few of the figures meet your standards; Rob—our collaboration with Prof. Kageyama will be a treasured memory; Helena—your positivity in the mornings is a joy; Guy—thank you for the numerous lunches and train journeys. Thank you to the many Part IIs over the years for the energy they bring to the group.

Special thanks to the many friends in Oxford and elsewhere who have made these DPhil years fulfilling. Job, Ellen, Alec, Fabian, Rhys, Adan, Bob, Nick, Henry, James, and Elena—thank you for the many lunches, squash or tennis matches. Many thanks also to the LMH, SPC and Magdalen tutors for the opportunity to teach at their colleges.

Un immense merci à la famille Guéroult. Une mention tout à fait spéciale pour mon petit frère (mais grand en esprit), Jean Guéroult, dont la joie et la bonne humeur sont une inspiration. Cette thèse, d'une certaine manière, est une extension du makila de MGP: 'Kisifrotsipik'. Très bonne lecture!

Contents

List of Figures

List of Tables

List of Abbreviations

BFGS . . . . . Broyden–Fletcher–Goldfarb–Shann
BLBQ . . . . . Bilinear Biquadratic
DBP . . . . . Dicalcium Barium Propionate
DFPT . . . . . Density Functional Perturbation Theory
DFT . . . . . Density Functional Theory
DOS . . . . . Density of States
DSP . . . . . Dibarium Strontium Propionate
GGA . . . . . Generalise Gradient Approximation
HPC . . . . . Hybrid Photon Counting
INS . . . . . Inelastic Neutron Scattering
IXS . . . . . Inelastic X-ray Scattering
IReps . . . . . Irreducible Representations
GULP . . . . . General Utility Lattice Program
LA . . . . . Longitudinal Acoustic
LAMMPS . . Large-scale Atomic/Molecular Massively Parallel Simulator
LDA . . . . . Local Density Approximation
LO . . . . . Longitudinal Optic
MC . . . . . Monte Carlo
MP . . . . . Monkhorst Packing
MOF . . . . . Metal Organic Framework
NTE . . . . . Negative Thermal Expansion
PDF . . . . . Pair Distribution Function
PES . . . . . Potential Energy Surface
PXRD . . . . . Powder X-ray Diffraction
RMC . . . . . Reverse Monte Carlo
RUM . . . . . Rigid Unit Model
TDS . . . . . Thermal Diffuse Scattering
TA . . . . . Transverse Acoustic
TO . . . . . Transverse Optic

1 Introduction

1.1 Atomic Motion

The ancient Greek and Roman atomist philosophers were convinced that any aggregate of atoms had to be in constant "vibration (παλμός) even when the whole is at rest".[1] For them, this atomic motion occurred in all solid objects and was necessary to describe change in the physical world. Lucretius, a Roman atomist, describes how this hidden motion of atoms could be thought of as a distant army manoeuvring, where the men are mobile, while the army itself "appears to be at rest, and lie [...] quiet on the plains".[2,3] It is surprising how apt this analogy still is today.

It took around two thousand years for the established scientific consensus to agree with these ancient philosophers. The specific heat models of solids developed by Einstein and Debye in the early 20$^{\text{th}}$ century both required vibrating atoms.[4,5] It was, in fact, a major concern that this thermal motion might be too significant and potentially prevent any clear interference phenomena in Laue's original X-ray diffraction experiment in 1913. Arnold Sommerfeld, Laue's supervisor, was sceptical that the atoms would retain a regular arrangement necessary for reflection conditions to be met.[6] Fortunately, the small amplitudes of the thermal oscillations meant that Laue's X-ray diffraction experiment was a success. The temperature-dependent Debye-Waller factor was developed soon after, allowing the crystallographer to approximate the signature of these thermal motions and refine a good, albeit static, structure model to their experimental diffraction patterns.[7–9] Even today, X-ray diffraction experiments

are often held at low-temperatures (100 K) to minimise the atomic vibrations and associated thermal diffuse scattering (TDS). These static average structure solutions have worked well for the traditional crystallographer and predict most chemical and electronic properties of materials well. Yet, there are many phenomena where the dynamics play a fundamental role: key examples include phase transitions, thermal expansion, and conductivity.[10,11] The atomic motions that govern these processes are not random and are closely related to the interatomic forces of the system.

This thesis is predominantly concerned with understanding the key lattice vibrations for a range of systems and their corresponding temperature-dependent properties. Coarse-graining is used to identify the important vibrational modes that drive the studied phenomena. Several temperature-dependent properties are explored in this thesis with this coarse-grained approach: phase transitions within the cyanospinel family (chapter 3) and dicalcium barium propionate (chapter 4) and negative thermal expansion (NTE) in metal dicyanides (chapter 5). The last two results chapters have coarse-graining as a common theme. One describes a general methodology for calculating the low-energy modes of framework materials (chapter 6), whilst the other models the disordered layer structure of $Ni(CN)_2$.

This introduction begins with the theory of lattice dynamics. The key physics behind our properties of interest—viz. phase transitions and thermal expansion—are then covered. We finish with a description of the rigid unit mode (RUM) model and how coarse-graining can help in understanding important phonon modes and structural complexity.

1.2 Lattice Dynamics

Thermal excitations and zero-point motion keep atoms in solids constantly oscillating about their equilibrium position.[10,11] The whole crystal can be understood as a set of 3D oscillators that result in waves characterised by a frequency (ω) and a wave-vector ($\mathbf{q}$) that sets the periodicity and direction. These waves have discrete energies where the fundamental quantum for a specific wave is called a phonon. The atomic displacements in solids are therefore collective and complex since they are the superposition of all the thermally accessible phonon modes weighted by their population factor. The displacement of an atom κ can be expressed as follows:

$$u_\kappa(t) = \sum_{j\mathbf{q}} \tilde{u}_\kappa \exp\left[\mathrm{i}(\mathbf{q}\cdot\mathbf{r}_\kappa - \omega_j(\mathbf{q})t)\right], \tag{1.1}$$

where $\tilde{u}_\kappa$ is the amplitude of a given mode, $\omega_j(\mathbf{q})$ its angular frequency and $\mathbf{r}_\kappa$ is the position of atom κ. The summation is for all modes j over all wave-vectors $\mathbf{q}$. Since $\mathbf{q}$ is periodic, waves that differ by a reciprocal lattice vector give identical displacements. All unique waves can therefore be contained within a unit cell in reciprocal space called the Brillouin zone that contains the Γ-point ($\mathbf{q} = (0,0,0)$) at its centre. An exact, quantitative framework of phonon modes can be derived with some simplifying approximations. Importantly, the theory that follows forms the basis of many lattice dynamical codes used in this thesis and in the literature to simulate thermal properties. The convention here follows that of Ref. 12.

1.2.1 Theory

One begins by considering the κ^{th} atom in the l^{th} unit cell of a crystal composed of n cells and N atoms in each unit cell. It oscillates around its equilibrium position, $\mathbf{r}_{\kappa l}$ by a small displacement $\mathbf{u}_{\kappa l}$ such that:

$$\mathbf{u}_{\kappa l}(t) = \mathbf{r}_{\kappa l}(t) - \langle \mathbf{r}_{\kappa l} \rangle, \tag{1.2}$$

where $\langle \ldots \rangle$ represents an average over time.

The potential energy of the crystal, U, can be expressed as a Taylor expansion in terms of these atomic displacements:

$$\begin{aligned} U = U_0 + \sum_{\kappa l,\alpha} \Phi^{\alpha}_{\kappa l} u^{\alpha}_{\kappa l} + \frac{1}{2!} \sum_{\substack{\kappa l,\kappa' l' \\ \alpha\beta}} \Phi^{\alpha\beta}_{\kappa l,\kappa' l'} u^{\alpha}_{\kappa l} u^{\beta}_{\kappa' l'} \\ + \frac{1}{3!} \sum_{\substack{\kappa l,\kappa' l',\kappa'' l'' \\ \alpha\beta\gamma}} \Phi^{\alpha\beta\gamma}_{\kappa l,\kappa' l',\kappa'' l''} u^{\alpha}_{\kappa l} u^{\beta}_{\kappa' l'} u^{\gamma}_{\kappa'' l''} + \ldots \end{aligned} \tag{1.3}$$

The coefficients are the first-order ($\Phi^{\alpha}_{\kappa l}$), second-order ($\Phi^{\alpha\beta}_{\kappa l,\kappa' l'}$), third-order ($\Phi^{\alpha\beta\gamma}_{\kappa l,\kappa' l',\kappa'' l''}$) force constant components where:

$$\Phi^{\alpha}_{\kappa l} \equiv \left(\frac{\partial U}{\partial u^{\alpha}_{\kappa l}} \right), \quad \Phi^{\alpha\beta}_{\kappa l,\kappa' l'} \equiv \left(\frac{\partial^2 U}{\partial u^{\alpha}_{\kappa l} \partial u^{\beta}_{\kappa' l'}} \right), \quad \Phi^{\alpha\beta\gamma}_{\kappa l,\kappa' l',\kappa'' l''} \equiv \left(\frac{\partial^3 U}{\partial u^{\alpha}_{\kappa l} \partial u^{\beta}_{\kappa' l'} \partial u^{\gamma}_{\kappa'' l''}} \right). \tag{1.4}$$

Due to translational symmetry, these components only depend on the relative positions of the unit cells (e.g., $\Phi^{\alpha\beta}_{\kappa l,\kappa' l'} = \Phi^{\alpha\beta}_{\kappa\kappa'}(l - l')$) whilst α, β, γ denote the Cartesian directions.

For Eq. (1.3), U_0 is an arbitrary constant that can be neglected. The first-order term is zero since the expansion is performed about the equilibrium positions, such that the residual force on each atom is zero. If the displacements are small, the harmonic approximation can then be used where the terms above the second order are truncated so that the interatomic forces are considered purely harmonic.

Equating Newton's 2nd law and the derivative of the potential energy allows the equation of motion to be:

$$m_\kappa \ddot{u}^\alpha_{\kappa l} = -\sum_{\kappa' l', \beta} \Phi^{\alpha\beta}_{\kappa l, \kappa' l'} u^\beta_{\kappa' l'}, \tag{1.5}$$

where m_κ is the atomic mass and $\ddot{u}^\alpha_{\kappa l}$ is the acceleration.

The solution for this equation of motion is the general wave-equation shown previously. Here, the amplitude of the mode, $\tilde{u}_\kappa$, is expanded out:

$$u^\alpha_{\kappa l}(t) = \sum_{j\mathbf{q}} A_{j\mathbf{q}} m_\kappa^{-1/2} e^\alpha_{\kappa j}(\mathbf{q}) \exp\left[\mathrm{i}(\mathbf{q}\cdot\mathbf{r}_{\kappa l} - \omega_j(\mathbf{q})t)\right], \tag{1.6}$$

where $e^\alpha_{\kappa j}(\mathbf{q})$ is the eigenvector that represents the associated atomic displacements of the given mode and $A_{j\mathbf{q}}$ is the normalisation constant. Eq. (2.22) can then be substituted back into the equation of motion (Eq. (1.5)), and with some rearrangement one arrives at the dynamical equation:

$$\mathbf{D}(\mathbf{q})\mathbf{e}_j(\mathbf{q}) = \omega_j^2(\mathbf{q})\mathbf{e}_j(\mathbf{q}), \tag{1.7}$$

where

$$D^{\alpha\beta}_{\kappa\kappa'}(\mathbf{q}) = \frac{1}{\sqrt{m_\kappa m_{\kappa'}}} \sum_{l''} \Phi^{\alpha\beta}_{\kappa\kappa'}(l'') \exp(\mathrm{i}\mathbf{q}\cdot\mathbf{r}_{l''}). \tag{1.8}$$

The dynamical matrix is the mass-normalized Fourier transform of the force constant matrix $\Phi^{\alpha\beta}_{\kappa\kappa'}(l'')$. It is a $3N \times 3N$ matrix such that there are $3N$ modes at each wave-vector $\mathbf{q}$ since each atom has three degree of freedoms (x, y, z) in which it can oscillate. $\mathbf{D}(\mathbf{q})$ is Hermitian such that its eigenvalues $(\omega_j^2(\mathbf{q}))$ are always real. Negative eigenvalue solutions, lead to imaginary values of ω and point to a dynamic instability for the structure at that wave-vector. In addition the mode eigenvectors, $e^\alpha_{\kappa j}(\mathbf{q})$ contain a description of the atomic displacement patterns associated with each normal mode. Solving the dynamical matrix gives the dependence between the phonon mode frequencies and their wave-vectors. These are plotted in phonon dispersion curves.

1.2.2 Phonon Dispersion Curves

Phonon dispersion curves will always have $3N$ branches. Of these, three are acoustic branches whilst the rest are called optic branches. The acoustic phonons are defined as having their $\omega \to 0$ as $\mathbf{q} \to 0$ and are more easily discerned at the Γ-point. As they approach the long-wavelength limit, their frequencies tend to zero linearly and their phase velocity ($\omega/\mathbf{q}$) is the speed of sound. The elastic constants of a solid can therefore be derived from its acoustic modes. Of the three acoustic modes, two are transverse acoustic modes (TA) where the atomic displacements are perpendicular to the wave-vector direction and one is the longitudinal acoustic mode (LA) with atomic displacements parallel to $\mathbf{q}$. Often, the transverse acoustic modes are lower in energy as there is less bond-stretching involved with the associated atomic displacements.

The optic phonons have finite frequencies at the Γ-point. Similarly to the acoustic modes, they can be sorted between longitudinal optic (LO) and transverse optic modes (TO). These are split near the Γ-point in polar crystals and cannot be modelled with short-range force-constant parameters such that non-analytical corrections are often required in addition for phonon calculations to adequately model the LO-TO splitting.

The phonon dispersion curves for MgO are shown in Fig. 1.1 as an example. MgO adopts the rock-salt structure with $Fm\bar{3}m$ symmetry. There are two atoms in the primitive cell and consequently, there are six branches in the phonon dispersion curves. Degeneracy can occur for both the TA and TO modes along certain paths in reciprocal space as a result of crystal symmetries. Whilst the X and X′ points are equivalent in reciprocal space, this phonon dispersion curve shows how the path taken in reciprocal space also matters. Hence, whilst the path $\Gamma \to \mathrm{X}$ is along the [100] direction such that both the TA and TO modes are degenerate; the $\Gamma \to \mathrm{X}'$ path is along the

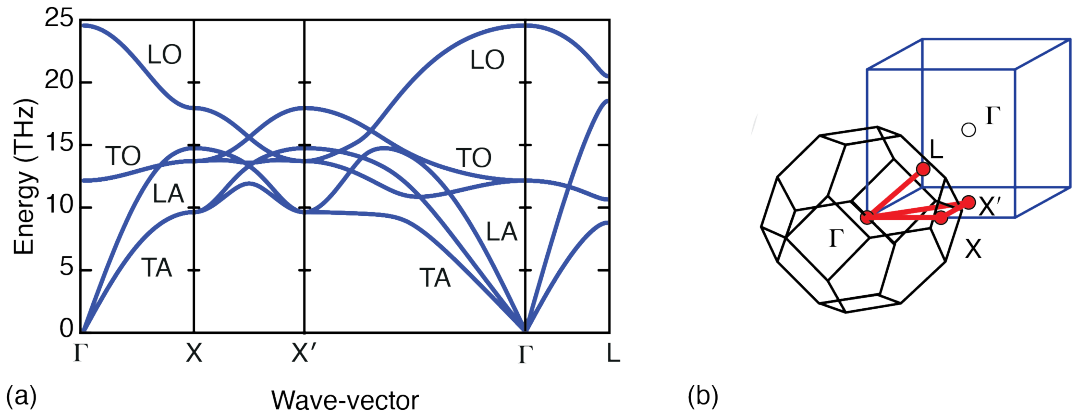

Figure 1.1: (a) MgO phonon dispersion curve calculated using the default core-shell potential found in the General Utility Lattice Program.[13,14] (b) A schematic representation of the path in reciprocal space. The Brillouin zone for a face-centred cubic structure is a truncated octahedron.

[110] direction and samples different points in reciprocal space. In this direction, each TA and TO mode has a distinct energy.

1.2.3 Anharmonic Effects

The harmonic approximation works well with small atomic displacements and at low temperature. It is perhaps surprising that such a crude model gives so many features of lattice dynamics such as the relationship between the wave-vector and frequency for phonon modes. There are, of course, phonon-mediated phenomena that cannot be explained by the harmonic model—such as thermal expansion, phase transitions and thermal conductivity—since harmonic phonon mode frequencies are neither temperature- nor pressure-dependent.

1.3 Thermal Expansion

Provided atomic displacements are not large, anharmonic terms can be added as perturbations to the harmonic model. These allow properties such as thermal expansion to be captured in the harmonic model framework. The pure harmonic model predicts

zero thermal expansion, since as the temperature increases, the average position of the atom remains unchanged. The Grüneisen formalism uses a quasi-harmonic approximation to derive thermal expansion coefficients: the interatomic force constants are assumed to be volume-dependent such that the phonon frequencies change with the crystal volume.[10,11,15] In a way, this approach is minimising the crystal free energy at a given temperature where the energy cost of expanding or contracting the lattice is balanced by the vibrational entropy associated with the change in phonon frequencies. The mode Grüneisen parameters can be defined as follows:[15]

$$\gamma(j,\mathbf{q}) = -\frac{\mathrm{d}\ln\omega(j,\mathbf{q})}{\mathrm{d}\ln V} = -\frac{V}{\omega(j,\mathbf{q})}\frac{\partial\omega(j,\mathbf{q})}{\partial V}. \tag{1.9}$$

This definition captures the sensitivity of the angular frequency (ω) of a mode (j) at each wave-vector ($\mathbf{q}$) to changes in crystal volume (V). Modes with $\gamma < 0$ soften at lower volumes and favour NTE, whilst modes with $\gamma > 0$ drive positive thermal expansion (PTE). This formalism provides a direct link between the macroscopic property of thermal expansion with the phonon modes of the system.

The mode Grüneisen parameters can then be combined to give a temperature-dependent bulk Grüneisen parameter:

$$\overline{\gamma}(T) = \frac{\sum_j \gamma_j C_V(j,T)}{\sum_j C_V(j,T)}, \tag{1.10}$$

where $C_V(\omega_i, T)$ is the mode-specific heat capacity. From these mode Grüneisen parameters, α_V, the volumetric thermal expansion coefficient can be calculated as follows:

$$\alpha_V(T) = \frac{1}{V}\left(\frac{\partial V}{\partial T}\right)_P = \frac{1}{BV}\sum_j \gamma_j C_{V,j}(T), \tag{1.11}$$

where B is the bulk modulus, and the summation is over all phonons, j.[16]

1.3.1 Negative Thermal Expansion

This thesis will come to explore in detail the phonon-mediated NTE mechanism of $M(CN)_2$ (M=Zn or Cd) in Chapter 5. Phonon-mediated NTE occurs over a larger temperature range, albeit with a smaller magnitude of α_V compared to NTE caused by charge transfer, or magnetic ordering mechanisms.[17–20] The local picture for phonon-mediated NTE is the tension effect (Fig. 1.2).[21–23] Here, for linear linkages of atoms where the bond lengths distort minimally, transverse displacements of the atoms lead to a volume decrease. For NTE to occur, there must be a sufficient population of NTE modes that outweigh the PTE modes over the whole of reciprocal space. It is often difficult to understand the underlying cause of NTE for a system, even with access to the full phonon dispersion relations. There is significant debate, for example, on the underlying mechanism that drives the NTE in ScF_3.[24–26] ScF_3 is a relatively simple system that adopts the cubic space group $Pm\bar{3}m$ with only 15 branches in its phonon dispersion curve. As a result, conceptual frameworks are of particular importance to rationalise lattice dynamics. The Rigid Unit Mode (RUM) model has proven to be successful for a series of different systems.[27–29]

1.4 The RUM Model

RUMs are phonon modes that preserve metal coordination geometries and bond lengths in the structural polyhedra of a given structure. RUMs rely on collective and cooperative rotations and translations of the structural polyhedra. The central idea is that these modes are often low-energy and are key in driving the thermal properties of network materials, predominantly silicates such as quartz,[30,31] cristobalite and zeolites.[33–36] A short description of the RUM model and its application to NTE and displacive phase transitions is given below. For further detail on the development and

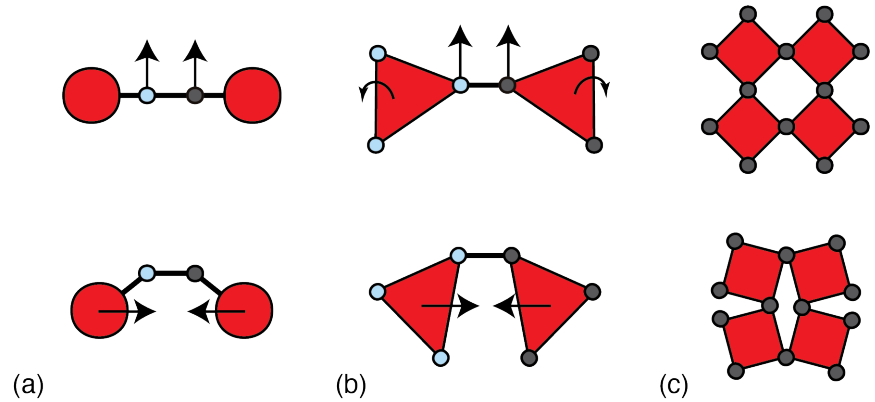

Figure 1.2: (a) The local tension effect. If the bonds are rigid, any transverse displacements of the central atoms leads inward displacements of the end-atoms. (b) A pictorial representation of how RUM rotations can also be considered as mechanisms for the tension effect. (c) For maximally expanded structures such as perovskites, RUM rotations can lead to an overall volume contraction and promote NTE.

applications of RUMs—such as local flexibility in zeolites—the interested reader is directed to the extensive review of the RUM model in Ref. 37.

The RUM model relies on the fact that the energy required to distort structural polyhedra is often much larger than the energy associated with flexing the linkage between two connected polyhedra. RUMs are therefore generally of low energy and exist along lines, planes or even curved surfaces in the Brillouin zone.[38,39] For certain zeolites, RUMs can be present at every wave-vector.[37]

1.4.1 NTE and the RUM Model

RUMs in NTE materials often have large negative Grüneisen parameters. Their motions geometrically lead to a decrease in volume when the structure is maximally expanded—as in the diamondoid or perovskite structures (Fig. 1.2 (c)). Indeed, many RUM motions would qualify for the local "tension effect" mechanism.[40,41] Yet, pure RUMs are often not sufficient in driving NTE since they often exist in very small fractions of reciprocal space. This is the case for ScF_3: in this system, the RUMs have

the lowest energies and largest magnitude in $-\gamma$, yet they only exist along specific lines in reciprocal space ($M \rightarrow R$) and hence cannot effect overall NTE on their own.[42,43] In these situations, quasi-RUMs or qRUMs become important. These qRUMs are phonon modes that are close to RUMs in reciprocal space whilst retaining sufficient rotational character such that they are of low frequency with a negative γ. For ScF_3, the qRUMs provide the necessary density of states to drive macroscopic NTE.[25,26]

The RUM model is governed by two force constants: one governing the stiffness of the structural polyhedra and the other governing the flexing at their linkage.[44] Perhaps interestingly, a finite polyhedral stiffness allowing some polyhedral distortion is considered key for NTE. This finite polyhedral stiffness allows qRUMs to exist over a broader range of wave-vectors near the RUMs whilst maintaining a low frequency. If the polyhedra were too stiff, the qRUMs frequency would be too high to contribute and lead to overall NTE.[26,37] In fact, if the polyhedra were infinitely rigid, there would be no NTE. The differences in the stiffness of their constituent polyhedra explains why NTE is observed in ScF_3 and not the oxide perovskites. The F–Sc–F linkage is flexible enough to allow a large number of qRUMs with a low frequency and $-\gamma$. For the oxide perovskites, the O–M–O linkage is much stiffer, driving the qRUM frequencies up and leading to an overall PTE.[26,37]

1.4.2 Limitations of the NTE RUM Model

RUMs and qRUMs provide low-energy pathways for cooperative polyhedral motions that often play a role in NTE. Yet, the presence of these modes does not necessarily guarantee that they are relevant to a system's NTE. $Zn(CN)_2$ is an example, and an alternative mechanism to understand its NTE is described in Chapter 5. $Zn(CN)_2$ adopts the cubic space group $Pn\bar{3}m$ where the Zn^{2+} ions are tetrahedrally coordinated

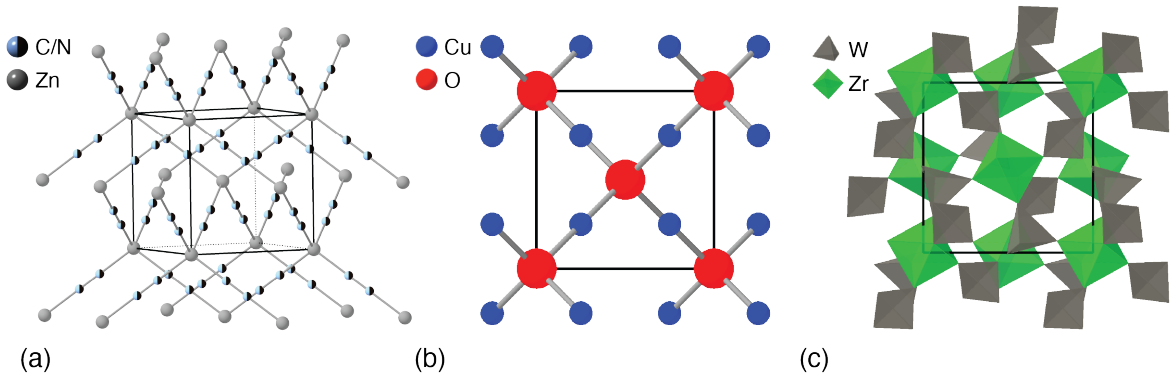

Figure 1.3: (a) Structure of $Zn(CN)_2$. Each Zn^{2+} ion is tetrahedrally coordinated to four CN^- ion that exhibit head-to-tail disorder. (b) Cu_2O structure which is analogous to that of $Zn(CN)_2$. (c) ZrW_2O_8 structure can be displayed as connected ZrO_6 octahedra and WO_4 tetrahedra. Some WO_4 tetrahedra are under-coordinated, such that there is some degree of flexibility in the network structure.

to the CN^- ions that exhibit head-to-tail disorder (Fig. 1.3 (a)). There are 8 RUMs at every wave-vector for $Zn(CN)_2$ and yet, only the two acoustic RUMs contribute meaningfully to NTE at low temperature.[45] There is a strong energy penalty associated with flexing the linear CN–Zn–CN linkage such that the usual rotational RUM modes are pushed to relatively high frequencies and do not contribute much to the overall NTE.

Cu_2O is a further system that displays NTE and where RUMs play a secondary role.[46,47] Cu_2O adopts the cubic space group $Pn\bar{3}m$ with a structure analogous to that of $Zn(CN)_2$ (where the O^{2-} ions replace the Zn^{2+} cations and the Cu^+ ions the CN^- ions (Fig. 1.3 (b))). The distance between Cu^+ ions in adjacent tetrahedra is constant, regardless of whether these tetrahedra belong to the same structural framework or to different ones. This dense arrangement ensures that the RUMs are not the lowest frequency phonon modes. The modes that contribute the most to NTE for Cu_2O involve atomic displacements where the O–Cu–O linkages remain linear and rigid rather than the RUMs.[48–50]

More complex, low-symmetry structures with large numbers of atoms in the unit cell can also make RUM analysis more difficult. ZrW_2O_8, for example, adopts the cubic space group $P2_13$ and has 132 phonon branches due to its 44-atom unit cell (Fig. 1.3 (c)). The low-symmetry of the structure leads to extensive mode-mixing, and makes it difficult to assign RUM character to the different modes that drive its NTE. The low frequency negative Grüneisen modes mostly involve rigid WO_4 tetrahedra coupled with distortions of the ZrO_6 octahedra.[51–53] Whilst some of these modes are qRUMs, one cannot decidedly prove that the NTE present in ZrW_2O_8 is RUM-driven.[54] In fact, distortions of the network structure of ZrW_2O_8 have been shown to be key in its NTE behaviour. Recent work describes a 'spaghetti dynamics' mechanism for NTE, related to W–O–W strings within the structure rather than a rigid unit mode picture.[55]

1.4.3 Displacive Phase Transitions

The RUM model was originally developed to describe displacive phase transitions in tetrahedral network structures such as quartz, cristobalite and tridymite and in this sense it is particularly successful.[37] For a displacive phase transition, the distorted structure can be described as a symmetry-lowering deviation from the parent structure.[56–58] This distortion can be related to the symmetry modes of the irreducible representations (IReps) of the parent space-group symmetry at the relevant wave-vector. These symmetry modes directly correspond to phonon modes of the high-symmetry phase. A phase transition occurs when the timescale of oscillation of one or more of these modes goes to zero and the low symmetry structure is formed, with the atomic displacements of the modes "frozen-in".[11,59] The modes responsible are said to "soften" as they decrease in frequency when approaching T_c and can be followed experimentally *via* inelastic scattering.

These 'soft-modes' need to be of sufficiently low energy for anharmonic effects to effectively stabilize the high-temperature phase and enable the transition. RUMs are great candidates for playing this role in corner-sharing polyhedral networks. Many phase transitions have therefore been related to specific RUMs, including incommensurate instabilities.[60–62] In addition, the lack of RUMs in structures that are overly constrained such as fully-connected octahedral networks (garnets, Al_2O_3, TiO_2) may indicate why there is a lack of phase transitions in many of these systems.[63] Perovskites are an exception, since their high symmetry leads to degeneracies among the constraints in their structural networks. This flexibility can also be related to the many perovskite distortions and associated tilts.[64,65]

1.4.4 The $\alpha \rightarrow \beta$ phase transition of cristobalite

An important structure studied in detail with the RUM model is that of β-cristobalite, the high-temperature polymorph of silica. In chapter 4 of this thesis, parallels are drawn between β-cristobalite and dicalcium barium propionate (DBP), with similarities in their low-energy dynamics and phase transitions. β-cristobalite crystallises in the cubic space group $Fd\bar{3}m$, and undergoes a displacive phase transition to α-cristobalite (tetragonal chiral space group $P4_12_12/P4_32_12$) at around 540 K.[66,67] The apparent average structure of β-cristobalite has unphysical linear O–Si–O angles, contrary to the usual 145° angle that most silicates display[68] (Fig. 1.4).

Analysis of total scattering data showed significant orientational fluctuations of the SiO_4 tetrahedra.[201] The instantaneous Si–O bond length was shown to be much greater than the nearest Si–Si distances, consistent with a bent O–Si–O angle. The O atoms have significant structural disorder such that the local picture differs significantly from the average structure with the idealised linear O–Si–O angle. Initially, the high

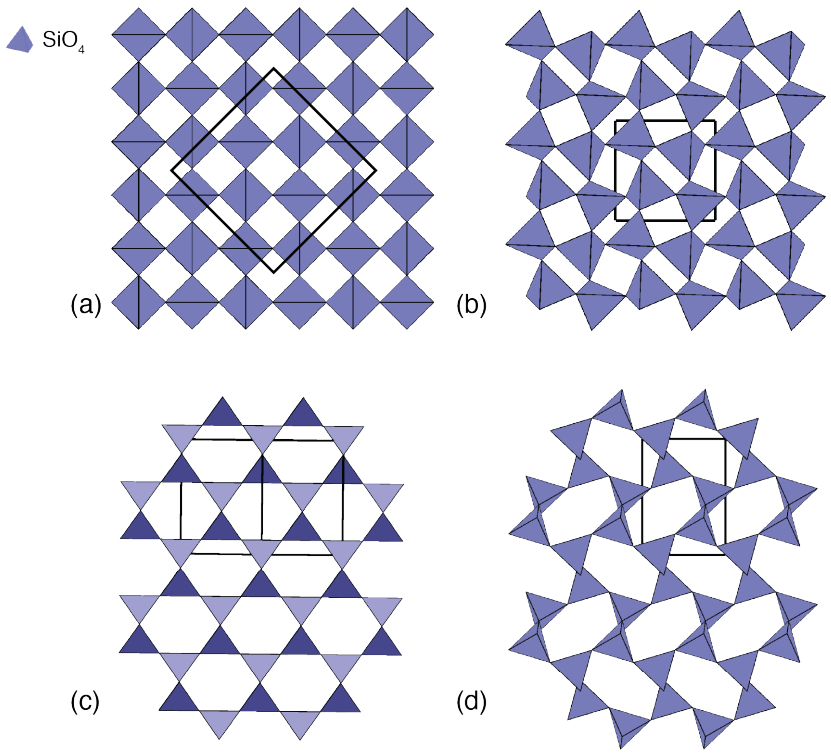

Figure 1.4: Structure of cristobalite in its $Fd\bar{3}m$ β-phase ((a) and (c)) and $P4_32_12$ α-phase ((b) and (d)) looking down the [001] ((a) and (b)) and [010] ((c) and (d)) directions of the orthorhombic cell. The cubic and orthorhombic unit cells are displayed as solid black lines in (a) and (b).

symmetry structure of β-cristobalite was proposed to consist of many small domains of the low-temperature phase or other lower symmetry space groups.[66,199] The problem with these interpretations is the high energy penalty of distorting SiO_4 tetrahedra required for these domains to form. An alternative picture uses the RUM model, where thermal population of low-energy RUMs in β-cristobalite are responsible for the disorder in tetrahedral orientations.

To quantify the role of RUMs, previous work calculated the phonon dispersion curves for β-cristobalite and identified the RUM modes using an SiO_2 potential developed by Sanders et al.[37,69] Certain difficulties arise when determining the phonon dispersion curves for high-temperature structures. Phonon calculations within the

harmonic approximation are being calculated at 0 K, such that the dispersion curves of high-temperature structures often contain several modes with imaginary frequencies. Phonon calculations may be undertaken with expanded unit cells (effectively negative pressure) to increase the phonon frequencies.[17] In real systems, these modes would be renormalised at higher temperatures *via* anharmonic processes such as fourth-order phonon coupling interactions.

For β-cristobalite, 2 RUMs were shown to lie along the $\langle 100 \rangle$ directions and 3 RUMs along the $\langle 111 \rangle$ directions (Fig. 1.5). These RUMs were found to be consistent with the diffuse scattering seen for β-cristobalite and with the atomic displacements associated with the Reverse Monte Carlo (RMC) configurations derived from the total scattering data.[70] In addition, inelastic neutron scattering data measured at the MARI spectrometer at ISIS showed a clear increase in intensity for low energy phonon modes (< 1 Thz) across the $\alpha \rightarrow \beta$ phase transition.[37] This population increase in low energy phonon modes is in line with the RUM model interpretation. Here, whilst the RUMs are low-energy modes in the β-cristobalite phase, they are renormalised and are of much higher energy in the α-phase. There are only 2 RUMs along the tetragonal $\langle 110 \rangle$ directions for α-cristobalite such that it does not exhibit the same degree of disorder in its SiO_4 tetrahedral orientations. It is the lower symmetry of the α-phase that leads the phonon modes that were previously RUMs in β-cristobalite to couple linearly to strain. As a result, their frequency increases rapidly below T_c. It is likely that the phase transition from $\beta \rightarrow \alpha$ for cristobalite is a dynamic effect with the softening of different RUMs.[27,201] RUMs have been shown to act as soft-modes in a series of systems including quartz,[71] $SrTiO_3$[72] and ScF_3.[73]

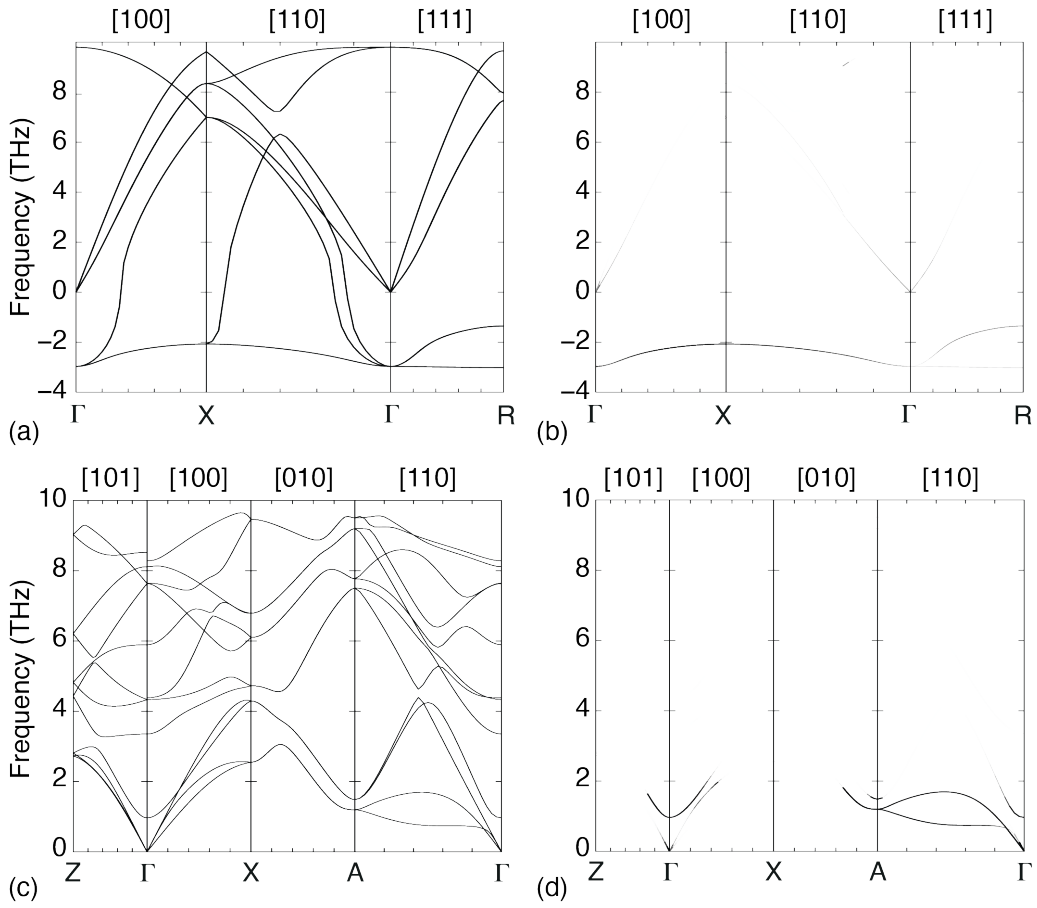

Figure 1.5: (a) Phonon dispersion curves calculated for β-cristobalite ((a)–(b)) and α-cristobalite ((c)–(d)). The phonon dispersion curves in (b) and (d) are coloured by their RUM character. The RUMs are renormalised in α-cristobalite to a much greater energy. Figure adapted and reproduced with permission from Ref. 37.

1.4.5 Coarse-grained potentials

Systems that undergo phase transitions can be described as experiencing local double-well potentials. Of course, the ratio between the depth of the well and the spring constant defines whether the phase transition is more proper displacive or order-disorder (Fig. 1.6).

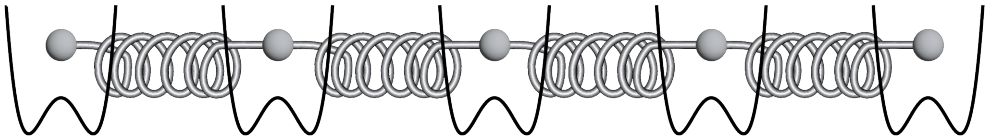

Figure 1.6: Pictorial representation of atoms that experience a local double-well potential.

Generally for systems with RUMs, the phase transitions are best described as displacive. As derived in Ref 37, the potential energy function for phase transitions described by RUMs can be defined as follows:

$$E = \frac{1}{2}J\sum_{\langle j,j'\rangle}(\varphi_j + \varphi_{j'})^2 - \frac{1}{2}\kappa_2\sum_j \varphi_j^2 + \frac{1}{4}\kappa_4\sum_j \varphi_j^4, \tag{1.12}$$

where φ_j is one rotational variable per polyhedral site, with j labelling the site. Hence, $\frac{1}{2}J\sum_{\langle j,j'\rangle}(\varphi_j + \varphi_{j'})^2$ supports RUM-like distortions, where neighbouring polyhedra rotate in opposite senses ($\varphi_j = -\varphi_{j'}$) whilst J is a measure of the polyhedral stiffness. The $-\frac{1}{2}\kappa_2\sum_j \varphi_j^2$ term favours polyhedral rotation whilst $\frac{1}{4}\kappa_4\sum_j \varphi_j^4$ is a higher-order term that limits the distortion at high φ_j.

The strength of these simple models is the conclusions that can be drawn from them. Here, it can be shown that $T_c \propto J\varphi_0^2$, such that the transition temperature is directly related to the stiffness of the polyhedra and φ_0, the value of $\langle\varphi\rangle$ at zero temperature. Both stiff polyhedra and phase transitions with large degrees of distortion lead to a high T_c. Close linear relationships between distortions and T_c have been shown for

$NaAlSi_3O_8$ (Na^+ being replaced with K^+)[74] and $KAlSi_2O_6$ (replacing K^+ with Rb^+ and Cs^+).[75] For the cyanospinel family described in Chapter 1, $Rb_2Hg(CN)_4$ has a considerably larger transition temperature than $K_2Hg(CN)_4$ (398 K compared with 111 K). The degree of distortion is greater for the Rb^+ case and may be indicative of displacive 'RUM-like' phase transitions occurring for these systems.[76]

1.5 Selecting the Appropriate Coarse-grained Model

The RUM model works well by abstracting network structures in terms of their structural polyhedra. This allows one to rationalise the atomic displacements of key phonon modes, and associated phenomena such as phase transitions and NTE. Effective coarse-graining relies on reducing the number of degrees of freedom of the problem at hand whilst still capturing the key physics. For an atomic structure, the total number of degrees of freedom is $3N$ where N is the total number of atoms in the structure. Coarse-grained approaches rely on reducing the overall number of degrees of freedom. The RUM model reduces $3N$, by treating groups of atoms that form structural polyhedra as collective objects. Each structural polyhedron composed of n atoms has six degrees of freedom (three translational and three rotational) and therefore leads to a reduction of $3n - 6$ in the total degrees of freedom. For certain structural problems, alternative coarse-graining approaches to the RUM model may be more appropriate. These can lead to an even greater reduction in the degrees of freedom and provide a better insight into the phenomena of interest. The choice of the most appropriate coarse-graining approach is informed by the structure. The RUM model works well for structures composed of connected and well-defined structural polyhedra. Similarly, for a layered system, treating its layers as whole collective objects will probably be most useful. Coarse-graining the layers leads to a much greater reduction

in the total number of degrees of freedom compared to a RUM model approach.

Distinct problems are explored in chapter 6 and 7 each with their own coarse-grained approach: one uses a simple, harmonic spring model to capture the low-energy dynamics of framework materials, whilst the other attempts to describe the disordered, layered structure of $Ni(CN)_2$ *via* a potential governed by the effective interactions between layers. For the interlayer potential of $Ni(CN)_2$, the next and next-nearest layer interactions are required to model its disordered stacking behaviour. For both chapters, coarse-grained approaches are fundamental in defining effective interactions and simplified potentials for each system similar to Eq. (1.12).

1.6 Aims of the Thesis

This thesis aims to understand the phonon modes or chemical interactions that drive phase transitions, NTE and complex stacking behaviour in a select number of relatively simple systems. Generally, these systems contain key low energy phonons that are investigated in detail in this thesis *via* both experimental and computational techniques. For each of these systems, additional background material is given at the beginning of their respective results chapters. Coarse-graining is used extensively in this thesis to simplify complex structures and phonon dispersion curves which facilitates the rationalisation of the microscopic origins of the observed phenomena. Thermal diffuse scattering (TDS) is employed throughout this thesis as a technique to probe the low-energy dynamics of our systems. A detailed description of TDS lies in the methods section, together with background on further techniques used in this thesis.

The results section starts with chapter 3. This chapter details a study of the low-energy dynamics of the cyanospinels $Rb_2Zn(CN)_4$ and $K_2Zn(CN)_4$. Whilst neither

undergo a temperature-dependent phase transition at atmospheric pressure, related members of the cyanospinel family do undergo displacive phase transitions. For these, a key L_1^- mode has been identified to change in frequency when approaching T_c. Using a combination of inelastic neutron scattering (INS), single crystal TDS and *ab initio* phonon dispersion calculations, the low-energy dynamics of $Rb_2Zn(CN)_4$ and $K_2Zn(CN)_4$ are investigated with a focus on the low-energy L-point optic modes.

DBP, the system of chapter 4, does undergo a phase transition at 267 K. Its complex unit cell makes *ab initio* calculations of its phonons intractable. Here, coarse-graining is used to understand the dynamics. Parallels are drawn between the $Ba(Ca)_2$ framework of DBP and SiO_2 cristobalite. The high temperature phase of DBP is exactly analogous to beta-cristobalite ($Fd\bar{3}m$). Molecular dynamics (MD) simulations are used to help build a microscopic understanding of this system.

The next chapter focuses on the transition-metal dicyanides $M(CN)_2$ (M = Zn, Cd) and their large, isotropic, NTE behaviour. In this chapter, a combination of neutron total scattering measurements and *ab initio* calculations is used to reassess the vibrational behaviour of the $M(CN)_2$ family. A simple, coarse-grained model turns out to capture the key NTE behaviour of $M(CN)_2$, especially at low temperatures.

Chapter 6 investigates whether an automated, coarse-grained approach can capture the low-energy dynamics of framework materials in a complementary fashion to the RUM model. This method, which only requires a structure as an input, allows for a straightforward approach in approximating TDS and for its interpretation in terms of whole-framework breathing and/or flexing modes. Its effectiveness is then discussed for a variety of chemically different framework materials, namely: TDS for MOF-5,

the mechanical flexibility of $[NH_4][Zn(HCOO)_3]$ and the NTE behaviour of $Zn(CN)_2$.

The last results chapter also uses coarse graining, but instead of dynamics, the disordered stacking arrangement of $Ni(CN)_2$ is tackled here. The 2-D layers of $Ni(CN)_2$ are treated as collective objects to create a pseudo-spin model that encodes the effective layer interactions. From Monte Carlo (MC) simulations, the powder X-ray diffraction (PXRD) patterns are then simulated and compared to experiment.

The conclusion discusses the main results in this thesis and how these coarse-graining methodologies may be applicable to new areas of research.

2
Methods

This section provides a theoretical background on the experimental and computational techniques used in this thesis. The atomic structure of a material dictates its physical properties and lattice dynamics. In turn, these determine the possible applications of a material. A good understanding of the atomic structure of one's system of interest is therefore key for the rational design of materials. The results in this thesis are mainly based on X-ray scattering techniques. This chapter begins with a general description of scattering theory, TDS, and INS. This is followed by descriptions of *ab initio* phonon calculations, MD, and MC simulations.

2.1 Scattering Theory

We start with the key scattering equations and follow the notation of Willis and Pryor found in Ref. 12. The fundamental quantity describing the scattered wave is the scattering amplitude, $Y(\mathbf{Q})$, which depends on the scattering vector $\mathbf{Q} = \mathbf{k}_i - \mathbf{k}_f$ where $\mathbf{k}_i$ and $\mathbf{k}_f$ are the wave-vectors of the incident and scattered waves respectively. X-rays are scattered by the electrons around the nucleus, such that the scattering from the atom is described by the atomic form factor:

$$f(\mathbf{Q}) = \int \rho(\mathbf{r}) \exp(\mathrm{i}\mathbf{Q} \cdot \mathbf{r}) d\mathbf{r}, \tag{2.1}$$

where $\rho(\mathbf{r})$ denotes the continuous distribution of electron density around the nucleus. For neutrons, the neutron scattering length, b, is often considered constant with no $\mathbf{Q}$-dependence since neutrons interact with the atomic nucleus rather than the electron density.

For a system of atoms, the amplitude is the coherent sum of waves scattered by each atom:

$$Y(\mathbf{Q}) = \sum_{\kappa} f_{\kappa}(\mathbf{Q}) \exp\left[\mathrm{i}\mathbf{Q} \cdot (\mathbf{r}_{\kappa})\right], \tag{2.2}$$

where κ is the atomic label, and r_{κ} denotes the position of the atom.

Experimentally, it is not the complex scattering amplitude $Y(\mathbf{Q})$ that is measured, but the scattering intensity, $I(\mathbf{Q})$, which is proportional to the square of the amplitude's magnitude:

$$I(\mathbf{Q}) \propto |Y(\mathbf{Q})|^2. \tag{2.3}$$

As a result, the scattering intensity measured during an experiment has lost the phase information contained in $Y(\mathbf{Q})$. This phase information is needed to recover the complete electron density and prevents a direct structure solution from crystallographic data. For a collection of atoms, the measured intensity is therefore given by:

$$I(\mathbf{Q}) \propto |Y(\mathbf{Q})|^2 = \sum_{\kappa} \sum_{\kappa'} f_{\kappa}(\mathbf{Q}) f_{\kappa'}(\mathbf{Q}) \exp\left[\mathrm{i}\mathbf{Q} \cdot (\mathbf{r}_{\kappa} - \mathbf{r}_{\kappa'})\right]. \tag{2.4}$$

The effect of average thermal displacements is also important and is captured by the Debye-Waller factor ($\exp(-W_{\kappa}(\mathbf{Q}))$). The Debye-Waller factor accounts for the reduction in Bragg intensities due to the thermal population of phonon modes in the crystal. Including the Debye-Waller factors in Eq. (2.4) leads to the following:

$$\begin{aligned} I(\mathbf{Q}) &= \sum_{\kappa} \sum_{\kappa'} f_{\kappa}(\mathbf{Q}) e^{-W_{\kappa}(\mathbf{Q})} f_{\kappa'}(\mathbf{Q}) e^{-W_{\kappa'}(\mathbf{Q})} e^{i\mathbf{Q}\cdot(\mathbf{r}_{\kappa}-\mathbf{r}_{\kappa'})} \\ &= \left| \sum_{\kappa} f_{\kappa}(\mathbf{Q}) e^{-W_{\kappa}(\mathbf{Q})} e^{i\mathbf{Q}\cdot\mathbf{r}_{\kappa}} \right|^2. \end{aligned} \tag{2.5}$$

2.1.1 Total Scattering

Total scattering techniques are particularly useful to build up a local atomic picture of the system of interest. A few key definitions are given here and relate to chapter

5, that studies the NTE mechanism of $M(CN)_2$. A more extensive account of these scattering equation can be found in Ref. 77.

For isotropic systems such as powders, the intensity depends only on the magnitude $Q = |\mathbf{Q}|$ since the intensity is averaged over all orientations. The intensity becomes the Debye Scattering Equation:

$$I(Q) = \sum_{\kappa} \sum_{\kappa'} f_{\kappa}(Q) f_{\kappa'}(Q) \frac{\sin(Qr_{\kappa,\kappa'})}{Qr_{\kappa,\kappa'}}, \tag{2.6}$$

where the phase term $\exp[i\mathbf{Q} \cdot (\mathbf{r}_{\kappa} - \mathbf{r}_{\kappa'})]$ has been averaged to $\frac{\sin(Qr_{\kappa,\kappa'})}{Qr_{\kappa,\kappa'}}$.

The structure function $S(Q)$ relates the coherent scattering intensity to the atomic structure. It can be defined as follows:

$$S(Q) = 1 + \frac{I_{coh}(Q)/N - \langle f(Q)^2 \rangle}{\langle f(Q) \rangle^2}, \tag{2.7}$$

where $\langle f(Q) \rangle = \sum c_{\kappa} f_{\kappa}(Q)$ (c_{κ} is the atomic fraction). This definition has $S(Q) \to 1$ as $Q \to \infty$. I often needs to be corrected to isolate the elastic, coherently scattered signal I_{coh}. Other contributions to I can come from incoherent scattering intensity (Compton scattering) or background intensity.

The reduced total scattering structure function $F(Q)$ emphasizes the oscillatory part of $S(Q)$:

$$F(Q) = Q[S(Q) - 1]. \tag{2.8}$$

The pair distribution function (PDF), $G(r)$, provides real-space information about interatomic distances and is obtained *via* a Fourier transform of $F(Q)$:

$$G(r) = \frac{2}{\pi} \int_{Q_{min}}^{Q_{max}} F(Q) \sin(Qr) \mathrm{d}Q = \frac{2}{\pi} \int_{Q_{min}}^{Q_{max}} Q[S(Q) - 1] \sin(Qr) \mathrm{d}Q. \tag{2.9}$$

$G(r)$ reflects the probability of finding pairs of atoms separated by distance r. It is often related to the radial distribution function $g(r)$ and the average number density ρ_0. The $D(r)$ function shown in chapter 5 is defined as follows:

$$D(r) = \frac{2}{\pi}\int_0^\infty QF(Q)\sin(Qr)\mathrm{d}Q,$$

where

$$D(r) = 4\pi r\rho_0 G(r).$$

2.2 X-ray Thermal Diffuse Scattering

X-ray TDS is a technique that is used throughout this thesis to measure the low-energy dynamics of a series of systems. A review of TDS and its theoretical background is given here.

Traditionally, the gold standard for the experimental measurement of phonon dispersion relations has been INS and inelastic X-ray scattering (IXS). For both, the energy and wave-vector of the phonons can be directly determined by comparing the difference in energy and direction between the incident and scattered neutrons or X-ray photons. However, both INS and IXS have their limitations. Both require access and beam-time at national facilities and necessitate a successful scientific proposal in an often competitive process. In addition, INS usually requires a large sample and is unsuitable for materials with high neutron absorption cross-sections. Meanwhile, for IXS, a high-energy resolution necessitates a low incident photon flux such that the data collection for a single point may take hours. For a full phonon dispersion curve mapping this may take several weeks.[78]

X-ray TDS is an attractive alternative. The measured scattered intensity away from the Bragg reflections (diffuse scattering) carries information about the population (hence energy) and polarisation of phonons. The advantage of X-ray TDS is the simple experimental set-up now possible on laboratory single-crystal X-ray diffractometers and its relatively fast acquisition rate of several hours. X-ray TDS is therefore an excellent probe for the low-energy dynamics of materials and a complementary technique to that of INS and IXS. This technique is used extensively in this thesis as an experimental probe of the low-energy dynamics of systems.

2.2.1 Historical Overview

The early reviews of Born[79] and Lonsdale[80] had high hopes that TDS would become a routine technique to measure phonon dispersion curves and elastic constants of crystals. This brief history of TDS is instructive in understanding why it has remained a relatively niche technique and is based on Refs. 78,81,82.

From the start of X-ray diffraction, diffuse streaks of intensity in addition to the expected Bragg reflections were observed on well-exposed X-ray Laue plates (Fig. 2.1).[86–88] In her review, Lonsdale relates how the terms "diffuse, anomalous, extra, subsidiary, background, temperature, modified, dynamic, quantum, non-Laue" were all used for this additional scattering.[80] By the early 1920s, the Faxen-Waller theory had been developed, linking these "extra reflections" to atomic displacements away from their mean position.[8,89] Lonsdale memorably describes how "the only criticism that can be made is that the experimental and theoretical agreement found is almost too good." Importantly, the theory showed how TDS depended on the elastic constants of a crystal and that the TDS intensity was not the smearing of Bragg peaks, whose sharpness was not affected by temperature.

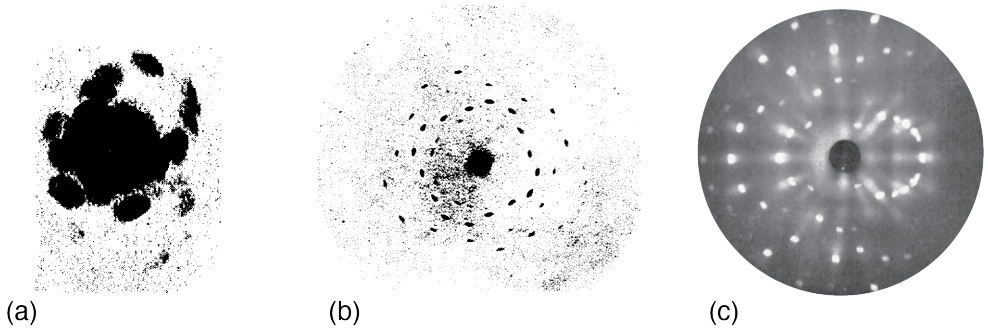

Figure 2.1: (a) First X-ray diffraction pattern measured by Friedrich and Knipping, using a $CuSO_4$ crystal. No specific orientation was used. (b) X-ray diffraction pattern of $CuSO_4$ when irradiated down its four-fold axis by Friedrich and Knipping. (c) X-ray diffraction pattern of KCl, with both Bragg reflections and TDS. Figures adapted and reproduced with permission from Ref. 6 for (a)–(b) and from Ref. 80 for (c).

Comprehensive experimental studies by Laval in the late 1930s made several further key observations: the TDS intensity was much lower than that of the Bragg reflections, the TDS intensity increased with temperature, the decay in intensity for TDS was much slower than the corresponding Bragg reflections when going further out in reciprocal space and the TDS varied from one substance to another, "even for planes of equal intrinsic reflecting power".[90–92]

In 1948, the first phonon dispersion curve was derived *via* experimental TDS[93] where the $\Gamma \rightarrow X$ region was successfully mapped out for Al (Fig. 2.2). Following this experiment, a number of systems such as α-Fe,[94] Cu,[95] Zn,[96] V,[97] Ge,[98] AgCl,[99] KCl[100] and ZnS[101] were investigated during the 1950s and had their elastic constants derived from their TDS. Unfortunately for TDS, it was quickly supplanted by the development of inelastic neutron and X-ray scattering techniques as more accurate methods of phonon study. In addition, ultrasonic experiments had greater accuracy when measuring elastic constants.[82] The inefficiency and weak signal-to-noise ratio of TDS were two factors that led to its relative demise from the start of the 1960s.

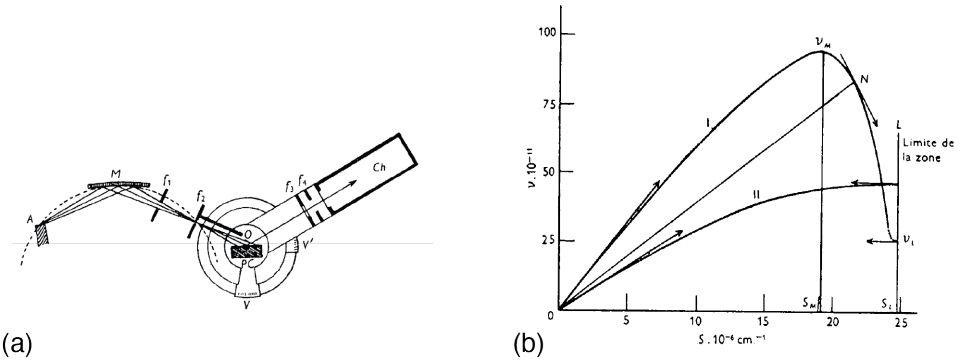

Figure 2.2: (a) Olmer's experimental set-up consisted of a normal X-ray diffraction experiment (b) Olmer's phonon dispersion curve derived from the TDS intensity measured for Al. Figure adapted and reproduced with permission from Ref. 93.

The study of diffuse scattering suffered from the 1960s to the 1990s as a result of the widespread usage of automated single point (0-D) X-ray detectors with electronic counters.[82] These detectors allowed for high quantum efficiency, low dead time and accurate quantitative measurement of the Bragg intensities. Yet, these detectors came at the cost of missing out the diffuse scattering away from the Bragg peaks. Previous photographic methods had made diffuse scattering visible whilst single-point detection allowed the collection of Bragg intensities without having to map out the regions of reciprocal space in between.

The advent of area X-ray detectors enabled a renaissance for diffuse scattering with the possibility of measuring it accurately and even in a laboratory setting. Of the several types of area detectors, hybrid photon counting (HPC) detectors are now considered the best in class.[83–85] Unlike charge-coupled devices or image plate detectors, there are minimal saturation effects (little streaking or blooming artefacts) that may affect the diffuse scattering. The HPC detectors are able to directly measure the X-ray intensities by counting the electron-hole pairs generated by the incident photons. These detectors are dynamic and thus wavelength sensitive such that fluorescence

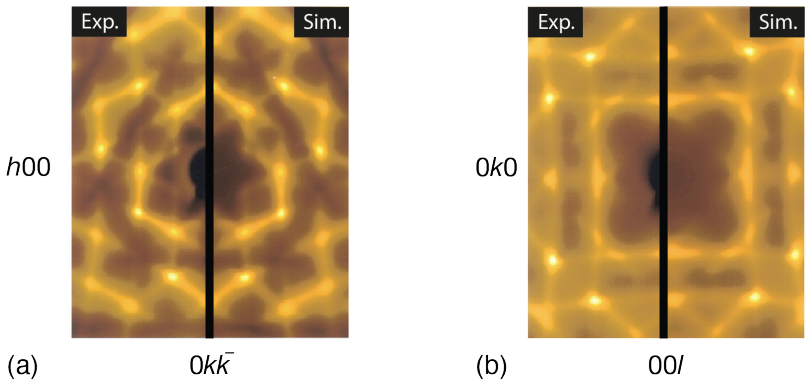

Figure 2.3: (a) Experimental and simulated transmission X-ray scattering taken for (a) Si(111) and (b) Si(100). Here, by virtue of the wavelength selected, the Bragg condition is never satisfied over the entire area of detection. A logarithmic intensity scale is used to prevent the low-**q** TA modes from dominating. Figure adapted and reproduced with permission from Ref. 104.

radiation can also be suppressed. HPC detectors have their readout electronics and semiconductor sensors separate, hence the term 'hybrid'. The in-house Rigaku XtaLAB Synergy-S Dualflex diffractometer, used for TDS measurements in this thesis, has an Dectris EIGER R 1M HPC detector. This detector has an active area of 1 million pixels of size $75\,\mu m \times 75\,\mu m$.[102]

These developments led to X-ray TDS being re-examined. In 1999, TDS patterns from a single crystal of Si were obtained *via* synchrotron X-rays and were well explained by the known Si phonon dispersion curves.[103] It was found that only the acoustic branches were needed to simulate the structured TDS intensity. Advances in accuracy and better spatial resolution in the early 2000s also allowed phonon dispersion curves to be derived from TDS, by fitting a Born–von Karman force constant model for both Si[104] (Fig. 2.3) and Nb.[122] Since then, several studies have been used TDS to describe the lattice dynamics for systems such as coesite,[105] Sn-polymorphs,[106] ice I_h,[107] α-cristobalite,[108] KCl_xBr_{1-x}[109] and TiO_2.[110] In addition, a model-free method to extract the full elasticity tensor for crystals from TDS measurements at two temperature

points was developed and shown to work on calcite, MgO[111] and thiourea.[112] Codes such as *ab2tds*[113] and *tds2el*[114] have also been developed to help simulate TDS and extract elastic constants from it.

2.2.2 Understanding TDS

The intensity of TDS can be directly derived given the phonon mode energies, phonon mode eigenvectors and atomic structure. For a given crystal, the total scattered intensity during an X-ray diffraction experiment, I, can be decomposed into different orders of scattering:

$$I(\mathbf{Q}) = I_0 + I_1 + I_2 + \ldots, \tag{2.10}$$

where I_0 is the zeroth-order (Bragg) scattering, I_1 is the first-order TDS, I_2 is the second-order TDS, etc.

The dominant contribution to TDS is its first order term I_1, which is defined as follows:[12,78]

$$I_1(\mathbf{Q}) = \frac{N\hbar}{2} \sum_{j\mathbf{q}} \frac{1}{\omega_j(\mathbf{q})} \coth\left[\frac{\hbar\omega_j(\mathbf{q})}{2k_\mathrm{B}T}\right] |F_j(\mathbf{Q})|^2, \tag{2.11}$$

where $F_j(\mathbf{Q})$ is the one-phonon structure factor defined as:

$$F_j(\mathbf{Q}) = \sum_\kappa \frac{f_\kappa(\mathbf{Q})}{(m_\kappa)^{1/2}} [\mathbf{Q}\cdot\mathbf{e}_{kj}(\mathbf{q})] \exp\left[-W_\kappa(\mathbf{Q})\right] \exp\left[i\mathbf{Q}\cdot\mathbf{r}_\kappa\right]. \tag{2.12}$$

For the first equation defining $I_1(\mathbf{Q})$, N is the number of unit cells, $\hbar$ is the reduced Planck's constant, the sum runs over phonon branches j and wave-vectors $\mathbf{q}$, $\omega_j(\mathbf{q})$ is the angular frequency, k_B is the Boltzmann constant, and T is the absolute temperature. For the second equation defining $F_j(\mathbf{Q})$, the sum runs over atoms κ in the unit cell, $f_\kappa(\mathbf{Q})$ is the atomic form factor, m_κ is the atomic mass, $\mathbf{e}_{\kappa j}(\mathbf{q})$ is the eigenvector component for atom κ, $W_\kappa(\mathbf{Q})$ is the exponent of the Debye-Waller factor, $\mathbf{r}_\kappa$ is

the atomic position vector, and the scattering vector $\mathbf{Q}$ relates to the phonon wavevector contained within the first Brillouin zone, $\mathbf{q}$, and the nearest reciprocal lattice vector $\mathbf{G}$ *via* $\mathbf{Q} = \mathbf{G} + \mathbf{q}$.

Several factors affect the intensity distribution of first-order TDS (and therefore TDS more generally) in reciprocal space. The first is the frequency dependence where:

$$I_1(\mathbf{Q}) \propto \sum_{j\mathbf{q}} \frac{1}{\omega_j(\mathbf{q})} \coth\left[\frac{\hbar\omega_j(\mathbf{q})}{2k_\mathrm{B}T}\right]. \tag{2.13}$$

At high temperature T or low frequency $\omega_j(\mathbf{q})$, the argument $x = \frac{\hbar\omega_j(\mathbf{q})}{2k_\mathrm{B}T}$ is small ($x \ll 1$). In this limit, the hyperbolic cotangent can be approximated as $\coth(x) \approx 1/x$ such that:

$$I_1(\mathbf{Q}) \propto \sum_{j\mathbf{q}} \frac{1}{\omega_j(\mathbf{q})^2} \quad \text{(for high } T \text{ or low } \omega\text{)}. \tag{2.14}$$

In any case, low-frequency modes generally contribute the most to the TDS intensity. The greatest TDS intensity is often near the Bragg reflections, since the frequencies of the acoustic modes tend to zero ($\omega \to 0$ as $\mathbf{q} \to 0$). As a result, TDS is particularly sensitive to the low-energy dynamics of systems.

The intensity is further modulated by the structure factor term. The 'shape' of the diffuse is determined by the $\mathbf{Q} \cdot \mathbf{e}_{kj}(\mathbf{q})$ term. Here, the eigenvectors of the mode are important. For modes where the eigenvectors are perpendicular to the scattering vector, there is no contribution to the intensity. It is therefore possible to choose points in reciprocal space where only transverse or longitudinal modes contribute to the TDS. This fact is often used when extracting the elastic constants of the crystal directly from TDS.[114]

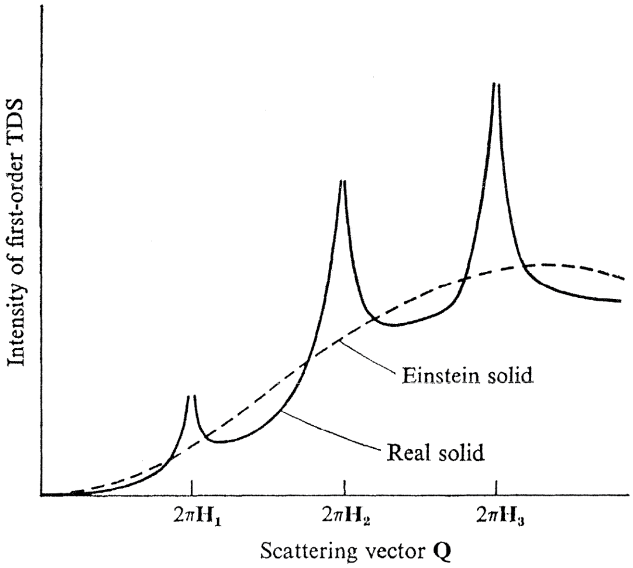

Figure 2.4: (a) The first-order TDS intensity for an Einstein solid and for a real solid. The long-range $Q = \langle u^2 \rangle^{-\frac{1}{2}}$ of the Einstein solid is modified by the phonon modes in a real crystal, with intensity increases near the Bragg points, here denoted by $n\pi\mathbf{H}$. Figure adapted and reproduced with permission from Ref. 12.

Lastly, there is a long range **Q**-dependence. Assuming that all the atoms in the unit cell have the same isotropic thermal displacement then $W_\kappa = W = \frac{1}{2}Q^2\langle u^2 \rangle$ such that:

$$I_1(\mathbf{Q}) \propto Q^2 \exp\left[-Q^2\langle u^2 \rangle\right]. \tag{2.15}$$

The general shape of this is shown in Fig. 2.4. Here, the TDS intensity increases to a maximum that occurs when $Q = \langle u^2 \rangle^{-\frac{1}{2}}$.

It is perhaps instructive to compare a simulated and experimental TDS pattern, together with a full phonon dispersion curve (Fig. 2.5). Here, the experimental diffuse scattering of hexagonal I_h is compared to the simulated TDS of its ordered polymorph Ice XI that has an orthorhombic space group $Cmc2_1$.[107] It is clear that the low-energy TA modes dominate the intensity of the TDS. The TDS intensity near the Bragg points is spread perpendicular to the direction of the scattering vector–this is a signature of the TA atomic displacements and is highlighted by the red boxes

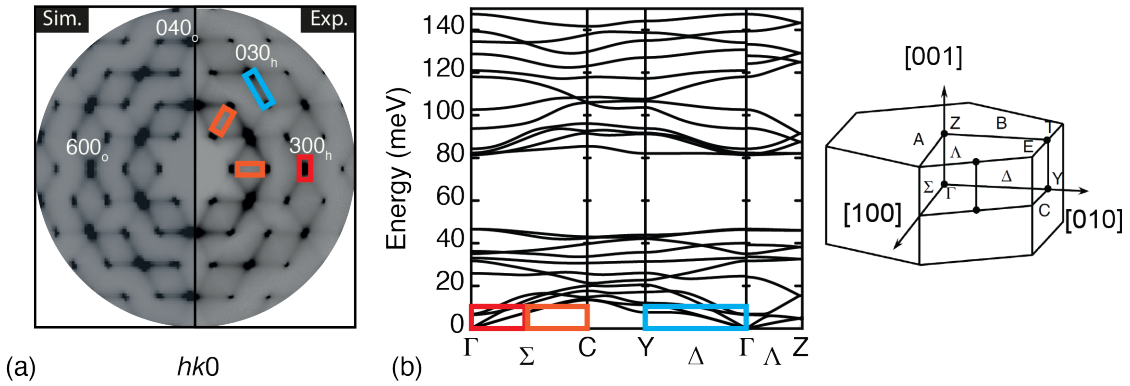

Figure 2.5: (a) Simulated and experimental diffuse scattering of orthorhombic Ice XI and hexagonal I_h respectively. (b) Calculated phonon dispersion curve for Ice XI along the symmetry path for hexagonal I_h. Figure adapted and reproduced with permission from Ref. 107

in Fig. 2.5. Moving further away from the Γ-point along the [100] (Σ) direction, the energies of the TA modes increase, and the TDS intensity decreases. In fact, it seems that any mode greater than 10 meV has a minimal contribution to the TDS intensity. This effect is highlighted by the orange boxes. Lastly, the TA modes remain comparatively low in energy along the $\Gamma \xrightarrow{\Delta} Y$ direction (blue boxes); this is reflected by the greater TDS intensity along this direction.

2.2.3 Simulating TDS

TDS has been simulated in this thesis directly from phonon calculations or by averaging configurations from MD simulations. For the direct method, the program *ab2tds*[107] can simulate TDS planes using output from DFT programs such as CASTEP[115,116] and *Phonopy*.[117,118] The program *ab2tds* models first-order TDS and has been used for the simulated TDS of the cyanospinels in Chapter 3 and $Zn(CN)_2$ in Chapter 5. Phonon calculations from other lattice dynamical codes such as GULP can be also be used by *ab2tds* once their outputs have been converted into the correct format. To model TDS from MD simulations, the program *Scatty*[121] allows one to average the scattering intensities that arise from a series of configurations, as long as the

individual atomic displacements are not too large. The benefit here is that the MD also includes anharmonic effects at temperature. This MD method has been employed for the simulated TDS of dicalcium barium propionate in Chapter 4 and the coarse-grained framework systems in Chapter 6.

2.2.4 First-order TDS Derivation

A complete derivation of TDS is given below. This derivation follows the nomenclature found in Willis and Pryor in Ref. 12. The final substitution steps link the derivation of Willis and Pryor with that of Xu and Chiang described in Ref. 122. A series of assumptions are used in this classical theory of deriving the intensity for TDS such as the adiabtaic approximation, where electrons are assumed to follow the atomic positions instantaneously.

The starting point for deriving the TDS intensity begins with the general expression for scattered intensity:

$$I(\mathbf{Q}) = \langle Y^*(\mathbf{Q})Y(\mathbf{Q})\rangle, \tag{2.16}$$

where $\langle ...\rangle$ is the time-average value. The scattering amplitude $Y(\mathbf{Q})$ is given by:

$$Y(\mathbf{Q}) = \sum_{\kappa l} f_\kappa(\mathbf{Q}) \exp\left[i\mathbf{Q}\cdot(\mathbf{r}_{\kappa l} + \mathbf{u}_{\kappa l})\right]. \tag{2.17}$$

Here $f_\kappa(\mathbf{Q})$ is the atomic form factor for κ^{th} atom in the l^{th} unit cell, $\mathbf{r}_{\kappa l}$ its equilibrium position, and $\mathbf{u}_{\kappa l}$ its displacement. The only difference here with Eq. (2.2), lies in separating $\mathbf{r}_\kappa$ into its $\mathbf{r}_{\kappa l}$ and $\mathbf{u}_{\kappa l}$ components.

One can then separate the time-dependent and time-independent terms to arrive at the following expression for the intensity:

$$I(\mathbf{Q}) = \sum_{\kappa l}\sum_{\kappa' l'} f_\kappa(\mathbf{Q}) f_{\kappa'}(\mathbf{Q}) \exp\left[i\mathbf{Q}\cdot(\mathbf{r}_{\kappa l} - \mathbf{r}_{\kappa' l'})\right] \ \langle \exp\left[i\mathbf{Q}\cdot(\mathbf{u}_{\kappa l} - \mathbf{u}_{\kappa' l'})\right]\rangle. \tag{2.18}$$

The thermal motion is captured by the term involving the average $\langle ... \rangle$. This is the important term for the TDS intensity. A key step relies on the Gaussian approximation for harmonic crystals, relating the average of the exponential phase factor to an exponential involving the mean square displacement:

$$\langle \exp\left[i\mathbf{Q}\cdot(\mathbf{u}_{\kappa l}-\mathbf{u}_{\kappa' l'})\right]\rangle = \exp\left[-\frac{1}{2}\langle(\mathbf{Q}\cdot[\mathbf{u}_{\kappa l}-\mathbf{u}_{\kappa' l'}])^2\rangle\right]. \tag{2.19}$$

This relation $\langle \exp(iA)\rangle = \exp(-\frac{1}{2}\langle A^2\rangle)$ occurs when A follows a Gaussian distribution with mean 0. For a harmonic crystal, $A = \mathbf{Q}\cdot[\mathbf{u}_{\kappa l}-\mathbf{u}_{\kappa' l'}]$.

In addition, $\langle(\mathbf{Q}\cdot[\mathbf{u}_{\kappa l}-\mathbf{u}_{\kappa' l'}])^2\rangle$ can be expanded:

$$\begin{aligned}\langle(\mathbf{Q}\cdot[\mathbf{u}_{\kappa l}-\mathbf{u}_{\kappa' l'}])^2\rangle = \langle|(\mathbf{Q}\cdot\mathbf{u}_{\kappa l})|^2 - (\mathbf{Q}\cdot\mathbf{u}^*_{\kappa l})(\mathbf{Q}\cdot\mathbf{u}_{\kappa' l'}) \\ -(\mathbf{Q}\cdot\mathbf{u}_{\kappa l})(\mathbf{Q}\cdot\mathbf{u}^*_{\kappa' l'}) + |(\mathbf{Q}\cdot\mathbf{u}_{\kappa' l'})|^2\rangle.\end{aligned} \tag{2.20}$$

One can define the Debye-Waller term, $W_\kappa(\mathbf{Q})$, as the mean squared displacement of the atom projected onto $\mathbf{Q}$:

$$W_\kappa(\mathbf{Q}) = \frac{1}{2}\langle|(\mathbf{Q}\cdot\mathbf{u}_{\kappa l})|^2\rangle. \tag{2.21}$$

Recalling from the Introduction that the displacement for each atom, $u_{\kappa l}(t)$, is given by:

$$u_{\kappa l}(t) = \sum_{j\mathbf{q}} A_{j\mathbf{q}} m_\kappa^{-1/2} e_{\kappa j}(\mathbf{q}) \exp\left[\mathrm{i}(\mathbf{q}\cdot\mathbf{r}_{\kappa l} - \omega_j(\mathbf{q})t)\right], \tag{2.22}$$

one can substitute this expression for $u_{\kappa l}(t)$, to rewrite the Debye-Waller factor as follows:

$$W_\kappa(\mathbf{Q}) = \frac{1}{2Nm_\kappa}\sum_{j\mathbf{q}}\left(\frac{E_j(\mathbf{q})}{\omega_j^2(\mathbf{q})}\right)|\mathbf{Q}\cdot\mathbf{e}_{kj}(\mathbf{q})|^2, \tag{2.23}$$

where $A_{j\mathbf{q}}$ has been split into several different terms, namely: N, the number of unit cells, $E_j(\mathbf{q})$, the average energy of the lattice mode and $\omega_j(\mathbf{q})$, the angular frequency of the phonon mode.

Substituting this definition of W_κ into Eq. (2.19) gives the following expression for the thermal average term:

$$\begin{aligned}\langle \exp\left[i\mathbf{Q}\cdot(\mathbf{u}_{\kappa l}-\mathbf{u}_{\kappa' l'})\right]\rangle &= \exp\left[-W_\kappa(\mathbf{Q})\right]\exp\left[-W_{\kappa'}(\mathbf{Q})\right] \\ &\quad\times\exp\left\{\frac{1}{2}\langle(\mathbf{Q}\cdot\mathbf{u}^*_{\kappa l})(\mathbf{Q}\cdot\mathbf{u}_{\kappa' l'})+(\mathbf{Q}\cdot\mathbf{u}_{\kappa l})(\mathbf{Q}\cdot\mathbf{u}^*_{\kappa' l'})\rangle\right\} \\ &= \exp\left[-W_\kappa(\mathbf{Q})\right]\exp\left[-W_{\kappa'}(\mathbf{Q})\right] \\ &\quad\times\exp\left\{\frac{1}{N}(m_\kappa m_{\kappa'})^{-\frac{1}{2}}\sum_{j\mathbf{q}}\frac{E_j(\mathbf{q})}{\omega_j^2(\mathbf{q})}\right. \\ &\qquad\times\frac{1}{2}\Big[(\mathbf{Q}\cdot\mathbf{e}_{kj}(\mathbf{q}))(\mathbf{Q}\cdot\mathbf{e}^*_{k'j}(\mathbf{q}))\exp\left[i\mathbf{q}\cdot(\mathbf{r}_{\kappa l}-\mathbf{r}_{\kappa' l'})\right] \\ &\qquad\left.+(\mathbf{Q}\cdot\mathbf{e}^*_{kj}(\mathbf{q}))(\mathbf{Q}\cdot\mathbf{e}_{k'j}(\mathbf{q}))\exp\left[-i\mathbf{q}\cdot(\mathbf{r}_{\kappa l}-\mathbf{r}_{\kappa' l'})\right]\Big]\right\}.\end{aligned} \tag{2.24}$$

Substituting this whole expression back into Eq. (2.18) gives the full expression for $I(\mathbf{Q})$. For practical calculations, the final exponential term containing the cross-terms (dynamic correlations) is expanded as a Taylor series $e^x \approx 1 + x + \frac{x^2}{2!} + \ldots$. This expansion separates the intensity into different orders of scattering as shown previously in Eq. (2.25):

$$I(\mathbf{Q}) = I_0 + I_1 + I_2 + \ldots, \tag{2.25}$$

where I_0 is the zeroth-order (Bragg) scattering, I_1 is the first-order TDS, I_2 is the second-order TDS, etc.

The zeroth-order term I_0 arises from the first term in the Taylor expansion:

$$\begin{aligned}I_0 &= \sum_{\kappa l}\sum_{\kappa' l'} f_\kappa(\mathbf{Q})\exp\left[-W_\kappa(\mathbf{Q})\right] f_{\kappa'}(\mathbf{Q})\exp\left[-W_{\kappa'}(\mathbf{Q})\right]\exp\left[i\mathbf{Q}\cdot(\mathbf{r}_{\kappa l}-\mathbf{r}_{\kappa' l'})\right] \\ &= \left|\sum_{\kappa l} f_\kappa(\mathbf{Q})\exp\left[-W_\kappa(\mathbf{Q})\right]\exp\left[i\mathbf{Q}\cdot\mathbf{r}_{\kappa l}\right]\right|^2 \\ &= \underbrace{\left|\sum_{\kappa} f_\kappa(\mathbf{Q})\exp\left[-W_\kappa(\mathbf{Q})\right]\exp\left[i\mathbf{Q}\cdot\mathbf{r}_{\kappa}\right]\right|^2}_{\text{Structure Factor Squared}}\underbrace{\left|\sum_{l}\exp\left[i\mathbf{Q}\cdot\mathbf{r}_{l}\right]\right|^2}_{\text{Lattice Sum Squared}}.\end{aligned} \tag{2.26}$$

This is the standard Bragg scattering equation. The intensity is proportional to the squared magnitude of the unit cell structure factor (including the Debye-Waller

reduction $\exp[-W_\kappa]$) multiplied by the lattice sum squared. The lattice sum yields delta functions only when the Bragg condition $\mathbf{Q} = \mathbf{G}$ (the reciprocal lattice vector) is satisfied, such that I_0 is zero elsewhere.

The first-order TDS term I_1 arises from the second term in the Taylor expansion:

$$\begin{aligned} I_1 = &\sum_{\kappa l}\sum_{\kappa' l'} f_\kappa(\mathbf{Q})\exp\left[-W_\kappa(\mathbf{Q})\right] f_{\kappa'}(\mathbf{Q})\exp\left[-W_{\kappa'}(\mathbf{Q})\right] \\ &\times \frac{1}{2N}(m_\kappa m_{\kappa'})^{-\frac{1}{2}}\sum_{jq}\frac{E_j(\mathbf{q})}{\omega_j^2(\mathbf{q})}(\mathbf{Q}\cdot\mathbf{e}_{kj}(\mathbf{q}))(\mathbf{Q}\cdot\mathbf{e}^*_{k'j}(\mathbf{q})) \\ &\times \{\exp\left[i(\mathbf{Q}+\mathbf{q})\cdot(\mathbf{r}_{\kappa l}-\mathbf{r}_{\kappa' l'})\right] + \exp\left[i(\mathbf{Q}-\mathbf{q})\cdot(\mathbf{r}_{\kappa l}-\mathbf{r}_{\kappa' l'})\right]\} \\ = &\frac{1}{N}\sum_{j\mathbf{q}}\frac{E_j(\mathbf{q})}{\omega_j^2(\mathbf{q})}\left|\sum_{\kappa l} m_\kappa^{-\frac{1}{2}} f_\kappa(\mathbf{Q})\exp\left[-W_\kappa(\mathbf{Q})\right](\mathbf{Q}\cdot\mathbf{e}_{kj}(\mathbf{q}))\exp\left[i(\mathbf{Q}-\mathbf{q})\cdot\mathbf{r}_{\kappa l}\right]\right|^2. \end{aligned} \tag{2.27}$$

The derivation relies on recognising the symmetry between the $\mathbf{q}$ and $-\mathbf{q}$ terms. Both the energy and angular frequency terms are even functions with respect to $\mathbf{q}$, whilst $\mathbf{e}_{kj}(\mathbf{q}) = \mathbf{e}^*_{kj}(-\mathbf{q})$. The lattice sum contained within the absolute square in the final line of Eq. (2.27) imposes scattering conditions. Again, one can separate $\mathbf{r}_{\kappa l} = \mathbf{r}_\kappa + \mathbf{r}_l$ and look at the sum over l:

$$\left|\sum_l \exp\left[i(\mathbf{Q}-\mathbf{q})\cdot\mathbf{r}_l\right]\right|^2 = C\sum_{\mathbf{G}}\delta(\mathbf{Q}\mp\mathbf{q}-\mathbf{G}), \tag{2.28}$$

where C is a constant. The delta function enforces the condition for first-order phonon scattering: $\mathbf{Q} = \mathbf{G} + \mathbf{q}$, recalling that $\mathbf{G}$ is the nearest reciprocal lattice vector and $\mathbf{q}$ is a phonon wave-vector within the first Brillouin zone. TDS intensity, therefore, exists throughout reciprocal space, not just at Bragg reflections.

The commonly cited final form, enforces this delta function condition such that:

$$I_1(\mathbf{Q}) = N\sum_{j\mathbf{q}}\frac{E_j(\mathbf{q})}{\omega_j^2(\mathbf{q})}\left|\sum_\kappa \frac{f_\kappa(\mathbf{Q})}{\sqrt{m_\kappa}}\exp\left[-W_\kappa(\mathbf{Q})\right](\mathbf{Q}\cdot\mathbf{e}_{kj}(\mathbf{q}))\exp\left[i\mathbf{G}\cdot\mathbf{r}_\kappa\right]\right|^2. \tag{2.29}$$

Note that $\mathbf{q} = \mathbf{Q} - \mathbf{G}$ is implicit within this equation.

To link Eq. (2.29) to expressions involving temperature explicitly as seen in Ref. 122, one needs to substitute the thermal energy of a phonon mode:

$$\begin{aligned} E_j(\mathbf{q}) &= \hbar\omega_j(\mathbf{q}) \left(\frac{1}{\exp\left[\frac{\hbar\omega_j(\mathbf{q})}{k_B T}\right] - 1} + \frac{1}{2} \right) \\ &= \frac{1}{2}\hbar\omega_j(\mathbf{q}) \coth\left[\frac{\hbar\omega_j(\mathbf{q})}{2k_B T}\right]. \end{aligned} \tag{2.30}$$

With this substitution, one arrives at the final expression:

$$I_1(\mathbf{Q}) = \frac{N\hbar}{2} \sum_{j\mathbf{q}} \frac{1}{\omega_j(\mathbf{q})} \coth\left[\frac{\hbar\omega_j(\mathbf{q})}{2k_{\mathrm{B}}T}\right] |F_j(\mathbf{Q})|^2, \tag{2.31}$$

where $F_j(\mathbf{Q})$ is the one-phonon structure factor defined as:

$$F_j(\mathbf{Q}) = \sum_{\kappa} \frac{f_\kappa(\mathbf{Q})}{(m_\kappa)^{1/2}} [\mathbf{Q}\cdot\mathbf{e}_{kj}(\mathbf{q})] \exp\left[-W_\kappa(\mathbf{Q})\right] \exp\left[i\mathbf{Q}\cdot\mathbf{r}_\kappa\right]. \tag{2.32}$$

2.3 Inelastic Neutron Scattering

TDS is energy-integrated. The energies of X-rays are on the keV energy scale, whilst phonons are at much lower (meV) energies. Energy-resolved experiments using X-rays such as IXS are particularly difficult. Neutrons, however, have an energy scale similar to phonons, and are excellent incident particles to measure both phonon energies and momenta.

The dynamic structure factor for neutrons, $S(\mathbf{Q}, E)$, is similar to the Eq. (2.31) derived previously for TDS :

$$\begin{aligned} S(\mathbf{Q}, E) = \frac{N\hbar}{2} \sum_{j,\mathbf{q}} \frac{1}{\omega_j(\mathbf{q})} |F_j(\mathbf{Q})|^2 \delta(\mathbf{Q} \mp \mathbf{q} - \mathbf{G}) \\ \times \{(n(\omega_j(\mathbf{q}), T) + 1)\delta(E - \hbar\omega_j(\mathbf{q})) \\ + n(\omega_j(\mathbf{q}), T)\delta(E + \hbar\omega_j(\mathbf{q}))\}, \end{aligned} \tag{2.33}$$

where:

$$F_j(\mathbf{Q}) = \sum_{\kappa} \frac{b_\kappa}{\sqrt{m_\kappa}} [\mathbf{Q}\cdot\mathbf{e}_{\kappa j}(\mathbf{q})] e^{-W_\kappa(\mathbf{Q})} e^{i\mathbf{G}\cdot\mathbf{r}_\kappa}. \tag{2.34}$$

There are in fact only two differences. The neutron scattering length (b_κ) is used rather than the **Q**-dependent X-ray atomic scattering factor ($f_k(\mathbf{Q})$. The second difference are the energy terms. These represent intensities from 'phonon creation' (energy loss of the neutron—$((n(\omega_j(\mathbf{q}),T)+1)\delta(E-\hbar\omega_j(\mathbf{q})))$ or from 'phonon annihilation' $((n(\omega_j(\mathbf{q}),T))\delta(E+\hbar\omega_j(\mathbf{q})))$ events. The annihilation of a phonon mode is directly related to the thermal population of the phonon modes ($(n(\omega_j(\mathbf{q}),T))$. For phonon mode creation, however, this can occur *via* both spontaneous (1) or stimulated emission ($(n(\omega_j(\mathbf{q}),T))$, such that the overall energy loss term is weighted by a factor of $(n(\omega_j(\mathbf{q}),T)+1)$. At low temperature, a phonon annihilation event is more unlikely since there are fewer phonons that have the required energy. The Dirac energy functions enforce energy conservation. In contrast, X-ray TDS, is not energy resolved such that the corresponding intensity is effectively integrating $S(\mathbf{Q},E)$ over all energy transfers.

Powder INS experiments in this thesis were performed at the ISIS neutron source. The neutrons in ISIS are generated *via* spallation, where pulses of protons travelling at 84 % of the speed of light collide with a heavy metal target composed of a core of W clad with Ta. The pulses of neutrons generated are then passed through a moderator and a series of choppers that selectively choose a set of incident energies. In this thesis, the MARI time-of-flight spectrometer was used on the powder samples of $K_2Zn(CN)_4$ and $Rb_2Zn(CN)_4$[123,124] and can select three incident energies of 100 meV, 23 meV and 10 meV. Once the neutrons of known incident energy impact the sample, they scatter and either gain or lose speed. These speeds can be measured by the detectors, and the corresponding gain or loss in neutron energy can be calculated.

The experiment on the cyanospinel powder samples was carried out with the spectrometer in high resolution mode (chopper at 400 Hz), with a flux of around

2×10^4 n cm^{-2} s^{-1} and a resolution of 3 meV for $E_i = 100$ meV and 0.2 meV for $E_i = 10$ meV. Two temperature points were used for each incident energy: 50 K and 300 K, with each measurement lasting 6 hours. The Mantid workstation was used to perform reconstruction, background subtraction and normalisation.[125] The Mslice tool was used to generate planes and cuts through S(Q,E). *Euphonic*[126,127] was used to simulate the inelastic neutron scattering from DFT phonon calculations.

2.4 DFT Phonon Calculations

DFT is an *ab initio* technique that determines the structure and properties of many-electron systems by solving for the electron density.[128,129] Effectively, DFT maps the insoluble many-body Schrödinger equation onto an effective one-electron problem. A key assumption is that the true ground-state electron density minimises the total energy functional of the system.[128,129] Solving for the electron density results in a series of approximations. The energy of the system can be expressed as:

$$E[\rho] = T_s[\rho] + \int V_{\text{ext}}(\mathbf{r})\rho(\mathbf{r})d\mathbf{r} + E_H[\rho] + E_{\text{xc}}[\rho], \tag{2.35}$$

where ρ is the electron density, $T_s[\rho]$ is the kinetic energy of the non-interacting electrons, $V_{\text{ext}}(\mathbf{r})$ is the external potential (often due to the atomic nuclei), $E_H[\rho]$ represents the Coulombic interaction the electron density has with itself (this is modelled as a self-interacting classical charge distribution) and $E_{\text{xc}}[\rho]$ is the exchange correlation functional. $E_{\text{xc}}[\rho]$ cannot be exactly identified and is system dependent. A series of different exchange correlation functionals can be used such as local density approximations (LDA) functionals,[130] generalised gradient approximations (GGA) functionals[131] and meta-generalised gradient approximation (meta-GGA) functionals.[132] LDA functionals depend only on the electron density, GGA functionals also take the derivatives of the electron density into account and are better for

modelling correlation effects. Bond strengths are typically overestimated when using LDA functionals. Lastly, meta-GGAs also include the local kinetic energy density for improved accuracy. Framework materials with long-range interactions often require additional dispersion corrections.

For the DFT calculations in this thesis, the GGA functional PBEsol[133] the transition metal dicyanides ($Cd(CN)_2$ and $Zn(CN)_2$) in Chapter 5. The meta-GGA functional rSCAN[134] was used for the cyanospinels ($K_2Zn(CN)_4$ and $Rb_2Zn(CN)_4$) in Chapter 3 and for the modelling the potential energy surface (PES) of the layer interactions for $Ni(CN)_2$ in Chapter 7. DFT allows for geometry optimisations of systems of interest by finding local minima in the PES. For all geometry optimisations in this thesis, the Broyden–Fletcher–Goldfarb–Shanno (BFGS) algorithm is used.[135] The BFGS algorithm uses the curvature of the PES to find the energy minima for the structure, iteratively changing lattice parameters and atomic positions. A high-precision geometry optimisation is a pre-requisite for any accurate phonon calculation.

Two methods have been used in this thesis to calculate phonons using DFT: the Supercell Method[119] and Density Functional Perturbation Theory (DFPT).[120] Whenever *Phonopy*[117,118] has been used, the phonon calculation is the Supercell Method.

The Supercell Method is conceptually simple. It calculates the force constants directly by constructing supercells, displacing an atom and calculating forces induced on all other atoms in the supercell.[119] This process is done for a series of displacements to build up the complete force-constant matrix for the supercell. If the supercell is large enough, the supercell force-constant matrix can be mapped onto the "real" force-constant matrix of the primitive cell such that phonons can be calculated at

any **q**. In this thesis, the supercell method was used for the phonon dispersion curves of $Zn(CN)_2$ and $Cd(CN)_2$.

DFPT can compute the phonons using the primitive unit cell at any arbitrary wave-vector **q**.[120] It does this directly, by calculating the effect of the perturbation phonon modes at specific wave-vectors **q** have on the electron density and the second derivatives of the energy. DFPT can then calculate the force-constant matrix. As a result, DFPT avoids the need for supercells and is better when their are long-range interactions in the system. In CASTEP this is implemented for GGA-functionals such as PBEsol and is used for the cyanospinels phonon calculations of this thesis.

2.5 General Utility Lattice Program

The General Utility Lattice Program (GULP)[13,14] can perform a variety of simulations on materials defined with boundary conditions. The focus is on using analytical solutions through the use of lattice dynamics and empirical potentials. A variety of force fields are available including the shell model for ionic materials, the embedded atom model for metals and molecular mechanics for organic systems.

In this thesis, GULP is used to calculate bulk elastic properties, and the phonon modes of framework materials. We use this code for our general 'framework modes' potential in Chapter 6, since the defined interatomic harmonic potentials can be implemented easily with GULP. GULP allows these potentials to be defined flexibly and in an additive fashion. Connectivity between atoms can be defined with keywords such as "connect" or alternatively, by using radial distance cut-offs. In chapter 6, harmonic two-body terms between atoms κ and κ' are defined by the deviation away

from an ideal length r_0 and a force constant k_{harm}:

$$E^{\text{harm}}_{\kappa\kappa'} = \frac{1}{2}k_{\text{harm}}[(r - r_0)]^2, \tag{2.36}$$

whilst the three-body terms:

$$E^{\text{harm}}_{\kappa\kappa'\kappa''} = \frac{1}{2}k_{\text{bend}}[(\theta - \theta_0)]^2, \tag{2.37}$$

are defined with respect to an ideal angle, θ_0 between three atoms.

Whilst a harmonic potential may be a good approximation for a bond between two atoms, a more accurate potential that encodes anharmonicity is given by the Morse potential:

$$E^{\text{Morse}}_{\kappa\kappa'} = D_e[1 - \exp(-a(r - r_0))]^2, \tag{2.38}$$

where r is the distance between the atoms, r_0 is the equilibrium bond distance, D_e is the well depth, and a relates to the 'width' of the potential.

Longer-range dispersion interactions such as the Lennard-Jones or Buckingham potential can also be implemented. Longer range electrostatic interactions are also included within GULP. For these interactions, GULP uses the Ewald summation technique to ensure rapid convergence.[136] This involves splitting the electrostatic potential into two convergent series with one in real space and the other in reciprocal space.

GULP is also used in this thesis to calculate phonon dispersion curves. For these phonon calculations, GULP performs geometry optimisations using the defined interatomic potentials, followed by calculation and diagonalisation of the dynamical matrix. For its geometry optimisations, GULP uses the Newton-Raphson optimisation method and finds the local minimum on the PES to which the starting coordinates

lie closest.[137] This optimisation method updates the positions of each cycle by the displacement vector, Δx, given by the expression:

$$\Delta x = -\alpha \mathbf{H}^{-1}\mathbf{g}, \tag{2.39}$$

where α is a scalar quantity. The gradient vector $\mathbf{g}$ and the Hessian matrix $\mathbf{H}$ are the first and second derivatives of the internal energy with respect to the atomic coordinates. The most expensive step is to calculate the inverse of the Hessian matrix. GULP uses the BFGS algorithm to update the Hessian matrix efficiently. Once geometry optimisation has occurred, GULP can calculate phonon mode frequencies and eigenvectors at user-specified $\mathbf{q}$ points.

2.6 MD Simulations

MD simulations can be used to model the dynamics of systems at a given temperature. The Large-scale Atomic/Molecular Massively Parallel Simulator (LAMMPS) program[144] has been used in this thesis. Once supercells with associated interatomic potentials have been defined, initial velocities related to the starting temperature are supplied to the atoms. Following this, at each timestep, the forces acting on each atom can be calculated and an integration algorithm is used to solve Newton's equations of motion. These are then used to update the new positions and velocities of all atoms at each discrete timestep. Thermostat (NVT ensemble) and barostat (NPT ensemble) algorithms can also be applied to maintain temperatures and pressures during the simulations. The MD simulations in this thesis all start with an equilibration period at a constant temperature. MD simulations are used in Chapter 4, when modelling the phase-transition behaviour of DBP and for calculating the TDS of the coarse-grained framework systems in Chapter 6.

2.7 Monte Carlo Simulations

MC simulations generate representative atomistic models for a given interaction model. The following overview follows that of Ref. 138. MC simulations do not require an exactly solvable model or a unique ground state. In addition, the derived configurations from MC simulations are explicit atomic configurations. These configurations can be used to compare directly to experimental diffraction patterns, for example. As a result, MC simulations are a technique of choice to gain insights about particular structural features of disordered systems.[139–141]

In this thesis, the initial state for all MC simulations is generated with a random configuration of our features of interest. The energies of the configurations of our system are defined by a given Hamiltonian. Starting from the initial state (ν), with a defined potential, trial moves are accepted whenever the final state (μ) has a lower energy. If the move leads to an increase in the energy of the system, then this move is accepted with a probability of $\exp(\frac{-\Delta E}{k_{\mathrm{B}}T})$. Effectively, the condition of moving from state $\mu \rightarrow \nu$ is defined as:

$$P(\mu \rightarrow \nu) = \min\left\{1, \exp\left(\frac{E_\mu - E_\nu}{k_{\mathrm{B}}T}\right)\right\}. \tag{2.40}$$

For this thesis, the MC simulations are of the Markov chain variant where the next state only depends on the present state.[142] The acceptance probability ensures ergodicity, such that there is a non-zero possibility of moving from any state μ to any other state ν, whilst also ensuring that the MC simulations do not get stuck in local minima. In this way, once equilibration is reached with a sufficient number of steps, MC simulations are effectively sampling a series of states where the probability of being in a particular state is proportional to its Boltzmann weight.

The number of moves required for equilibration varies according to the MC simulation, although it is usually sufficient to use $\sim 10^3$ more moves than spins in the simulation. Often, to ensure that the system is equilibrated, a spin-autocorrelation function is used:[143]

$$\langle \mathbf{S}(0) \cdot \mathbf{S}(t) \rangle = \frac{1}{N} \sum_i \mathbf{S}_i(0) \cdot \mathbf{S}_i(t), \tag{2.41}$$

where $\mathbf{S}(0)$ are the initial spin states at a given temperature, and $\mathbf{S}(t)$ the spin states at time t. The number of steps taken for $\frac{1}{N}\sum_i \mathbf{S}_i(0) \cdot \mathbf{S}_i(t)$ to reach zero can be defined as t_0. After this time, the system can be considered to be decorrelated from its initial state. In this thesis, to ensure that equilibration has occurred, the simulation is initially run for $\sim 10t_0$ before sampling the MC configurations.

Slow simulated annealing also helps to find ground state structures. Rapid quenching in MC simulations can lead to the formation of defects and disordered domains. To avoid this issue, the temperature can be multiplicatively varied in an MC simulation such that $T_{i+1} = (1 - \alpha)T_i$ where i is the cooling step after equilibration at each temperature point. The constant α governs the rate of temperature decrease.

MC simulations have been used in this thesis to model the disordered layered structure of $Ni(CN)_2$ in Chapter 7. The disordered layer structure of $Ni(CN)_2$ is re-cast as a chain of interacting 4-D pseudo-spins with a defined Hamiltonian. These pseudo-spins have phase-angles that are varied each step. Once equilibration has occurred at a given temperature, these 4-D pseudo-spin chains were related back to the atomistic structure of $Ni(CN)_2$ and the diffraction patterns were simulated to compare with experimental data.

3

Low-energy Dynamics in $A_2Zn(CN)_4$ Cyanospinels

3.1 Introduction and Acknowledgements

This chapter focuses on the low-energy dynamics of the cyanospinels $Rb_2Zn(CN)_4$ and $K_2Zn(CN)_4$. INS measurements are used in conjunction with TDS and *ab initio* phonon calculations to build up a picture of the important phonon modes within this family. In addition, symmetry analysis of the key vibrations is performed. These modes are compared with the L_1^- mode that has been previously assigned as responsible for the ferroelastic transition under pressure for $K_2Hg(CN)_4$. The alkali cation sublattice is shown to play a greater role than previously thought in the low-energy dynamics of cyanospinels.

Powder inelastic neutron scattering measurements were undertaken on the MARI spectrometer at the ISIS Neutron and Muon Spallation Source. Dr Johnathan M. Bulled accompanied me on the beamtime. The beamline scientists were Dr Duc Le and Dr Mohamed Aouane. Mr Guy Greenbaum helped with the Pawley and Rietveld refinements for the X-ray powder diffraction measurements.

3.2 Background

3.2.1 The Cyanospinel Family

The $A_2B(CN)_4$ cyanospinels are an intriguing family of hybrid materials, the structures of which are comprised of a pyrochlore lattice of A^+ cations surrounding

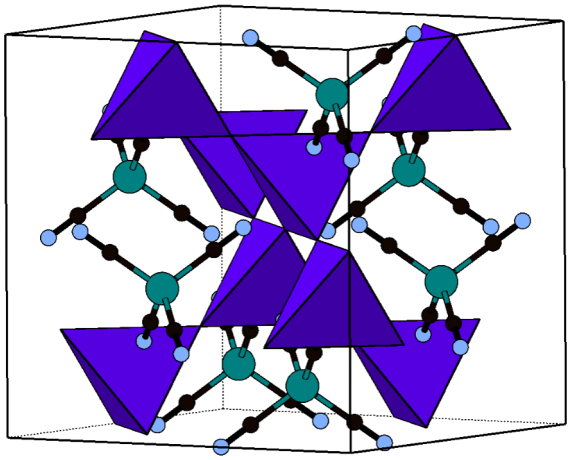

Figure 3.1: The cyanospinel structure type. It contains a pyrochlore network of A-site cations surrounding molecular $[B(CN)_4]^{2-}$ tetrahedra. Note that in this representation, the A-site cations are at the vertices of the tetrahedra and that there are no atoms in their interior.

molecular $[B(CN)_4]^{2-}$ tetrahedra (see Fig. 3.1).[145–147] Cyanospinels have historically been used as model systems for understanding the bonding in cyanometallate complexes and the way in which this bonding is affected by composition. Several studies, for example, have varied the B-site metal (using 3d vs 4d vs 5d transition-metals).[148–150] Most cyanospinels adopt $Fd\bar{3}m$ symmetry. The space group symmetries of all synthesised cyanospinels at room temperature and pressure are summarised in Table 3.1 based on information found in Ref. 151. Blanks occur when cyanospinels containing both cations have not been synthesised in the literature.

Table 3.1: Space group symmetries of cyanospinels at room temperature and pressure based on information in Ref. 151.

	Na^+	K^+	Rb^+	Cs^+	Tl^+
Zn^{2+}	$Fd\bar{3}m$	$Fd\bar{3}m$	$Fd\bar{3}m$	$C2/c$	$F\bar{4}3c$
Cd^{2+}		$Fd\bar{3}m$	$Fd\bar{3}m$		
Hg^{2+}		$Fd\bar{3}m$	$R\bar{3}c$		$Fd\bar{3}m$

At room temperature and pressure, there are two known cyanospinels that do not adopt a cubic spinel type structure: $Cs_2Zn(CN)_4$ and $Rb_2Hg(CN)_4$. These have structures with symmetries described by the space groups $C2/c$ and $R\bar{3}c$, respectively.[151,152]

$Cs_2Zn(CN)_4$ is the only cyanospinel to have the A^+ cation in an eight-coordinate square prismatic coordination geometry rather than a six-coordinate octahedral coordination geometry.[151] This is probably due to the large relative size of the Cs^+ cation compared to that of the Zn^{2+} cation. The radius ratio of $\frac{r_{Cs^+}}{r_{Zn^{2+}}}$ (2.45) is too large to be accommodated in a cubic spinel type structure, where the typical radius ratio is of 1.8.

The low radius ratio of 1.51 for $Rb_2Hg(CN)_4$ has been proposed as one possible driving force for its adoption of an $R\bar{3}c$ structure; however, there are multiple exceptions to the radius-ratio rules that undermine this explanation. For example, $Tl_2Hg(CN)_4$ crystallises with a cubic spinel structure ($Fd\bar{3}m$) when its $\frac{r_{A^+}}{r_{B^{2+}}}$ ratio is smaller than that of $Rb_2Hg(CN)_4$ (1.49 vs 1.51). Instead, an alternative, dynamic effect seems more plausible.

3.2.2 Ferroelastic Instabilities in Cyanospinels

Indeed, the cubic aristotype (space group $Fd\bar{3}m$) shows a variety of competing ferroelastic instabilities that can be controlled through judicious choice of composition, temperature, and pressure.[153,154] These instabilities are usually discussed in terms of correlated rigid-body rotations of the $[B(CN)_4]^{2-}$ tetrahedra.

At atmospheric pressure and variable temperature, both $Rb_2Hg(CN)_4$ ($T_c = 398\,K$) and $K_2Hg(CN)_4$ ($T_c = 111\,K$) exhibit ferroelastic phase transitions.[155] A ferroelastic

Table 3.2: Phase transition pressures at 298 K for $K_2M(CN)_4$ where M = Zn^{2+}, Cd^{2+}, and Hg^{2+}.

	Zn^{2+}	Cd^{2+}	Hg^{2+}
p_{c1} (kbar)	4	3	1.5
p_{c2} (kbar)	14	8	8.5

phase transition leads to spontaneous strain in the material and is the mechanical analogue to ferroelectric and ferromagnetic phase transitions. Multiple experiments have measured ferroelastic transitions in cyanospinels using a variety of techniques such as nuclear quadrupole measurements, Brillouin measurements, and Raman spectroscopy.[156–159] In addition, under variable pressures, phase transitions have also been observed for $K_2Cd(CN)_4$[160] and $K_2Zn(CN)_4$.[161] All of these phase transitions show the same symmetry lowering, namely a trigonal distortion from cubic $Fd\bar{3}m$ to trigonal $R\bar{3}c$. Furthermore, at elevated pressures additional first-order transitions became possible as shown in Table 3.2. The Hausmanite ($CuCr_2O_4$) structure type gave the best fit to the higher pressure structure that occurs after the second phase transition.[162]

These phase transitions from $Fd\bar{3}m$ to $R\bar{3}c$ correspond to a distinct alternating twist of modestly distorted $[B(CN)_4]^{2-}$ tetrahedra around the trigonal c axis (previously the cubic body diagonal) accompanied by a shift in the K^+ positions. In fact, these $[B(CN)_4]^{2-}$ tetrahedra rotate in an antiphase twist by 7.09° from their previously staggered configurations with minimal distortion of the structural polyhedra (Fig. 3.2).

These correlated tilts have been considered the driving force of the ferroelastic transition. Looking down the trigonal axis, it is also interesting how the K^+ ions also displace in much the same way as the $[B(CN)_4]^{2-}$ tetrahedra, effectively mirroring the CN^- ions. There is perhaps an electrostatic argument where the negatively charged

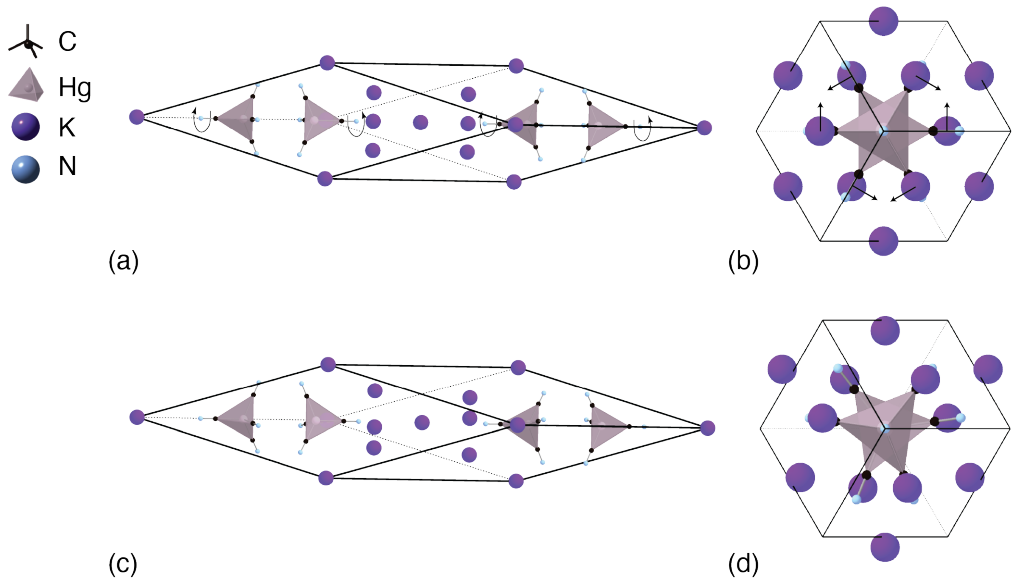

Figure 3.2: Ferroelastic phase transition for $K_2Hg(CN)_4$. The correlated tilts of the $[Hg(CN)_4]^{2-}$ tetrahedra have been highlighted as these are considered key factors in driving the ferroelastic phase transition: (a) and (b) are the high symmetry, high temperature structure in perspective view and along the trigonal axis, respectively; (c) and (d) are the rhombohedral structure after the ferroelastic phase transition. The arrows in (a) and (b) show the required displacements for the transition.

cyanides follow the positively charged potassium ions (and vice versa).

3.2.3 Symmetry Analysis of the Distortions

Using the published structures of the parent $Fd\bar{3}m$ and distorted $R\bar{3}c$ phases, one can arrive at a group theoretical description of the distortion modes relevant to the phase transition for $K_2Hg(CN)_4$. Symmetry analysis using the ISODISTORT software[163,164] showed three symmetry allowed modes: two Γ-point strain modes and an L-point displacement mode. The Γ_1^+ mode is completely symmetric and does not affect the space group symmetry. The Γ_5^+ mode captures the rhombohedral distortion and by itself it would lower the symmetry from $Fd\bar{3}m \rightarrow R\bar{3}m$. Displacements of the C and N atoms are allowed in Γ_5^+, whilst the Hg^{2+} and K^+ ions remain fixed. Lastly, the L_1^- mode leads to a lowering of symmetry from $R\bar{3}m$ to $R\bar{3}c$. Its wave-vector is at

$(\frac{1}{2},\frac{1}{2},\frac{1}{2})$ since it is at the L-point. This is the mode responsible for the slight alternating twist of the $M(CN)_4{}^{2-}$ tetrahedra along the c-axis together with the associated K^+ displacements, whilst the Hg^{2+} ions remained fixed. The L_1^- mode is the primary order parameter: activation of this mode also encompasses the distortion driven by the Γ_5^+ mode and the lowering of symmetry from $Fd\bar{3}m \rightarrow R\bar{3}c$.

There is only a single previous triple-axis inelastic neutron scattering measurement of a cyanospinel: the temperature-dependence of the scattering intensity for an L-point soft-mode in $K_2Hg(CN)_4$, which suggested the ferroelastic transition in that system to be of the soft-mode type.[165] The mode chosen to be followed had eigenvectors that were associated with $M(CN)_4{}^{2-}$ tetrahedral rotations. It was found that as the temperature was lowered towards the transition temperature, the frequency of the mode softened and decreased to zero such that the associated atomic displacements were frozen in. The cubic to trigonal (ferroelastic) phase transition was therefore concluded to be a dynamic effect. It was postulated that the cubic symmetry at higher temperatures may be a dynamic averaging of the rotations of the $[B(CN)_4]^{2-}$ tetrahedra. The charge density of the B^{2+} ion would be important in determining the energy required for rotations of the tetrahedra. This may explain why $K_2Hg(CN)_4$ undergoes a phase transition whilst $K_2Zn(CN)_4$ and $K_2Cd(CN)_4$ do not under atmospheric pressure.

3.2.4 The Importance of the Pyrochlore A-site Sublattice

Whilst much of the earlier focus was on intramolecular dynamics, it seems the pyrochlore A-site sublattice plays an important role in the lattice dynamics.[166–169] After all, the interactions between tetracyanometallate units are mediated by this A-site sublattice. A variety of alkali metal cations can be used, including Na^+, K^+, Rb^+, and Cs^+.[170] By comparison with the chemical environment in conventional alkali

metal cyanides (e.g., LiCN, NaCN, KCN etc.), these A-site cations are coordinatively unsaturated. The large (relative) A-site mass and the weak local bonding mean that correlated A-site motion is associated with low-energy phonon branches (2–10 meV) that mix heavily with the rigid-body $[B(CN)_4]^{2-}$ rotations.[171] The greater mass of Rb^+ compared to K^+ would explain why $Rb_2Hg(CN)_4$ has a considerably larger transition temperature than $K_2Hg(CN)_4$. The transition temperature for the $Fd\bar{3}m \rightarrow R\bar{3}c$ transition can even be varied between 111 K to 398 K by composition alone. This variation in T_c was explored with the $Rb_xK_{2-x}Hg(CN)_4$ series for $0 < x < 0.77$.[76] Lattice constants, densities, and pressure derivatives varied linearly with composition in line with Vegard's law.

The lower transition temperature of $Rb_2Hg(CN)_4$ may be intuitively explained by how the cation alkali sublattice affects the energy of the phonon mode that drives the phase transition. The angular frequency of a given mode, ω is governed by the following relation: $\omega \propto \sqrt{\frac{k}{\mu}}$, where k is the force constant and μ the reduced mass of the atoms involved. Increasing the mass ($M_{r(Rb^+)} \approx 2M_{r(K^+)}$) or weakening the strength of the interatomic interactions results in a reduction in the frequency of a mode. This would intuitively explain why $Rb_2Hg(CN)_4$ has a greater transition temperature than $K_2Hg(CN)_4$. This reasoning is reinforced by the distortion amplitudes: the antiphase rotations of the $[B(CN)_4{}^{2-}]$ tetrahedra are of a smaller magnitude for $K_2Hg(CN)_4$ (7.1°) compared to its Rb^+ counterpart (10.6°).[172] Taking a closer look at the distorted rhombohedral structure, the alkali sublattice is distorting heavily during the phase transition. The K^+ ion displacements are of a similar magnitude to the corresponding N atom displacements. The K^+ ion displacements preserve the original K^+ ion distances in a quasi-rigid unit-like motion of the kagome layers (Fig. 3.3).

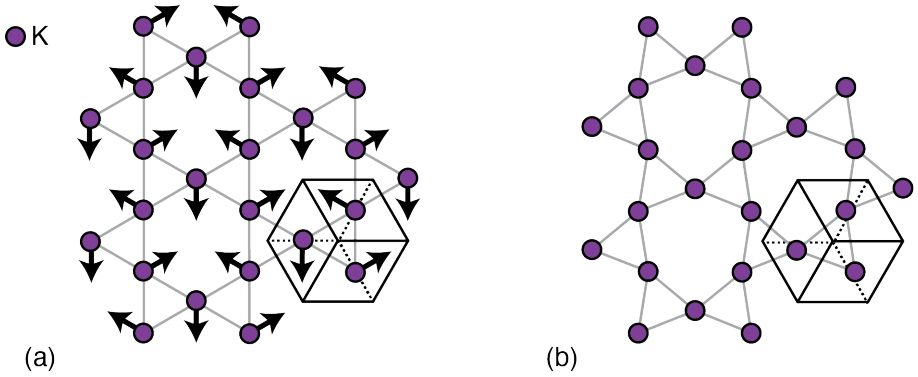

Figure 3.3: K^+ sublattice (a) above the phase transition and (b) below. The distances are preserved in a rigid-unit like distortion of the kagome layers when viewed down the trigonal axis of the rhombohedral cell.

3.3 Results

This chapter aims to reassess the role of the A-site sublattice in the low-energy dynamics of two key cyanospinels: $Rb_2Zn(CN)_4$ and $K_2Zn(CN)_4$. *Ab initio* phonon calculations are used in conjunction with powder INS and single-crystal TDS measurements to build up a picture of the low-energy dynamics within this family and the role of the A-site sublattice. We start with the phonon dispersions of the two cyanospinels themselves and compare the simulated powder INS measurements with those obtained from experiment. TDS measurements are qualitatively linked to the phonon modes, their respective energies, and dispersions. Finally, RUM and symmetry analysis of the low-energy modes are carried out and compared to the L_1^- mode that has been previously assigned for the pressure-induced ferroelastic transition of $K_2Hg(CN)_4$.

3.3.1 Synthesis and Powder Fits

Both powders and single crystals of $K_2Zn(CN)_4$ and $Rb_2Zn(CN)_4$ were used. $K_2Zn(CN)_4$ was purchased from Sigma-Aldrich and used as received for grinding into a fine powder. $Rb_2Zn(CN)_4$ was synthesised from $K_2Zn(CN)_4$ by ion-exchange of an aqueous solution of $K_2Zn(CN)_4$ with a 2 M solution of RbOH. An ion-exchange

column was loaded with 100 g of DOWEX (50 W X8). After rinsing with distilled water, the column was saturated with the 2 M RbOH solution over several washes. $K_2Zn(CN)_4$ (2.00 g) was dissolved in distilled water (50 mL) and passed through this column. This process was repeated twice, regenerating the column with aqueous RbOH in between. The combined fractions were combined and $Rb_2Zn(CN)_4$ obtained as a solid by rotary evaporation. Powder X-ray diffraction (PXRD) patterns of both $K_2Zn(CN)_4$ and $Rb_2Zn(CN)_4$ were measured using a Bruker D8 ADVANCE diffractometer operating in Bragg-Brentano geometry and employing mirror-monochromated Cu-Kα radiation ($\lambda = 1.5406$ Å). PXRD patterns were collected for 30 minutes across 2θ range 10–80°, and fitting was performed in Topas (Fig. 3.4).[173]

An initial Pawley fit was performed and confirmed the space group symmetry ($Fd\bar{3}m$) of both $K_2Zn(CN)_4$ and $Rb_2Zn(CN)_4$, with associated lattice parameters, a, of 12.4933(1) Å and 12.9092(2) Å, respectively. These lattice parameters are extremely similar to those found in the literature—12.53 Å for $K_2Zn(CN)_4$[146] and 12.87 Å for $Rb_2Zn(CN)_4$.[152] Rietveld fits were then undertaken using the lattice parameters extracted from the Pawley fits as starting points. The cyanides were constrained to be rigid-bodies (R_{wp} = 12.8% for $K_2Zn(CN)_4$ and 12.0% for $Rb_2Zn(CN)_4$). For $Rb_2Zn(CN)_4$, the occupancy of Rb was refined and found to be equal to 1. The full, tabulated lattice parameters and atomic positions from the Rietveld refinements can be found in the Appendix. For both $K_2Zn(CN)_4$ and $Rb_2Zn(CN)_4$, X-ray quality crystals were prepared by slow evaporation from a concentrated aqueous solution. The lattice parameters as determined by single crystal X-ray diffraction were comparable to those obtained from Pawley fitting (12.54 Å for $K_2Zn(CN)_4$ and 12.91 Å for $Rb_2Zn(CN)_4$ with reflections consistent with $Fd\bar{3}m$ symmetry).

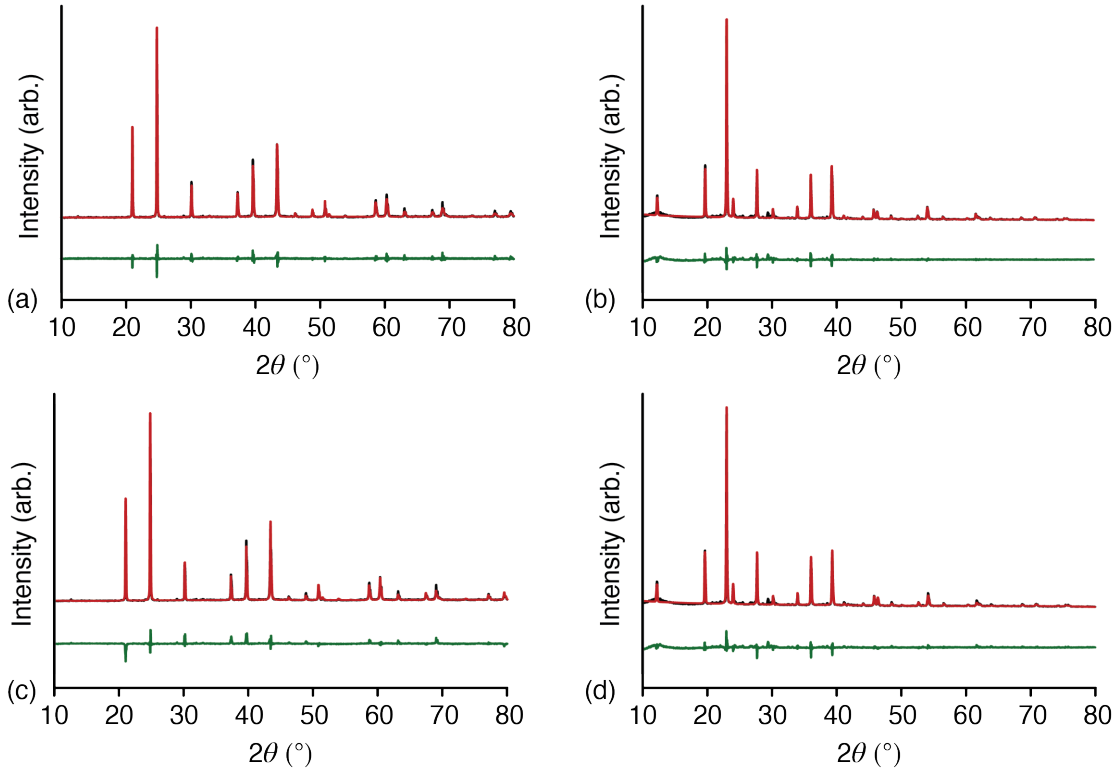

Figure 3.4: Pawley and Rietveld fits of the powder diffraction data. Pawley fits are given in (a) and (b) where the black and red lines refer to the experimental data and Pawley fit, respectively, with the difference in green. The Rietveld fits are given in (c) and (d) where the black and red lines refer to the experimental data and Rietveld fit, respectively, with the difference in green.

3.3.2 Phonon Calculations

Ab initio phonon calculations were also undertaken using DFT to directly compare to experiment. Two different methods were used since getting non-imaginary phonon frequencies for $K_2Zn(CN)_4$ proved difficult. The first method aimed to use DFPT as implemented in CASTEP (version 18.1).[115,116] The cells were geometry optimised using the BFGS method,[135] while keeping the symmetry fixed. The norm-conserving pseudopotentials of CASTEP were used with a Monkhorst Packing Grid[174] (MP Grid) of $8 \times 8 \times 8$ and plane-wave cut-off energy of 1300 eV together with the PBESOL functional.[133] Convergence of energies was set to 10^{-9} eV per atom and convergence of force to 10^{-7} eV Å^{-1}. DFPT was then run on a phonon MP grid of $4 \times 4 \times 4$ offset

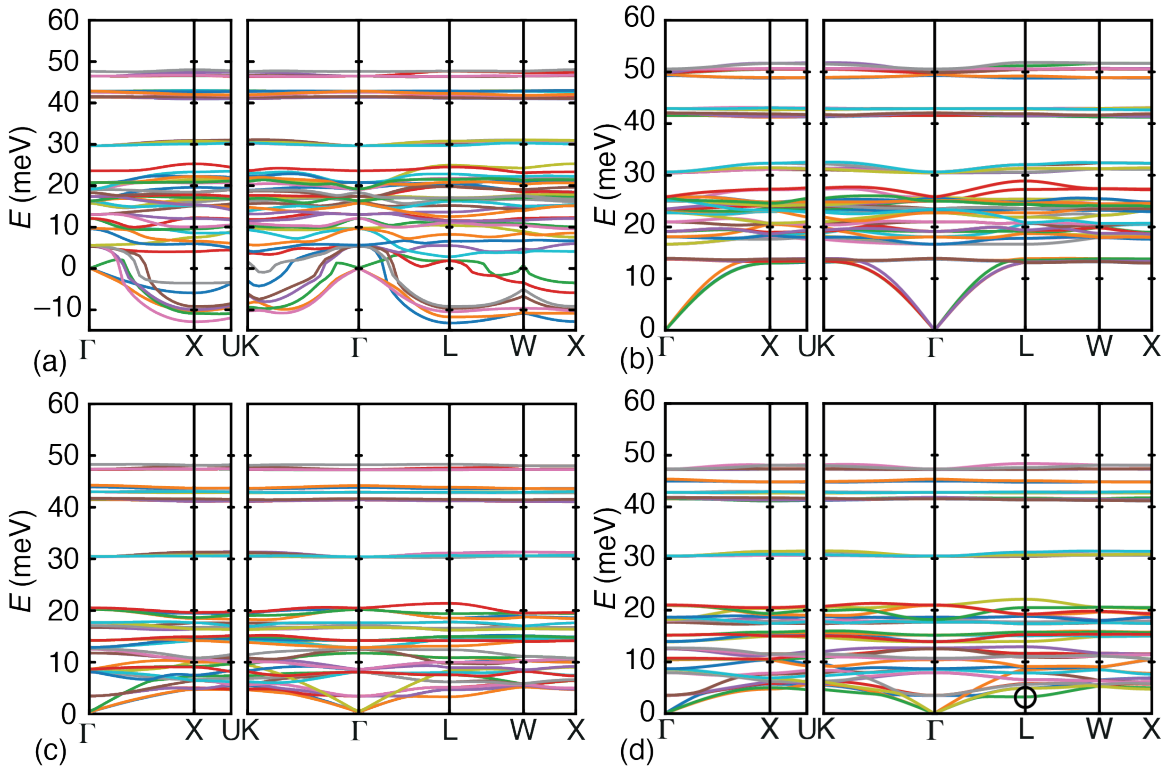

Figure 3.5: Phonon dispersion curves for $K_2Zn(CN)_4$ ((a) and (b)) and $Rb_2Zn(CN)_4$ ((c) and (d)). (a) and (c) were calculated using the DFPT method with norm-conserving pseudopotentials. (b) and (d) were calculated using a finite-displacement method with ultrasoft pseudopotentials. The lowest energy optic mode at the L-point is highlighted.

by 0.125 in all three directions. The phonon energy tolerance was set to 10^{-5} eV Å^{-2} and the e-field energy tolerance to 10^{-5} eV Å^{-3}. Whilst the phonons for $Rb_2Zn(CN)_4$ had positive and real frequencies, this is not the case for $K_2Zn(CN)_4$, where there are a series of dynamic instabilities (Fig. 3.5).

An alternative method was used to calculate the phonon dispersion curves shown in Fig. 3.5 (b) for $K_2Zn(CN)_4$ and (d) for $Rb_2Zn(CN)_4$. This method used CASTEP single point calculations in conjunction with *Phonopy*.[117,118] Geometry optimisations were undertaken using ultrasoft pseudopotentials and the rSCAN functional.[134] The plane wave cut-off energy was set at 1000 eV with an electronic energy tolerance of 10^{-13} eV per atom. The **q**-points MP spacing was set with a $2 \times 2 \times 2$ MP grid. The

finite-displacement method of *Phonopy* was used with a $2 \times 2 \times 2$ supercell. Single-point calculations were performed on multiple supercells with different displacements to then calculate a force-constant matrix. Phonon dispersion relations were then plotted using intervals of 0.1 reciprocal lattice units along high-symmetry directions of the Brillouin zone.

Both phonon dispersion curves have a similar form and energy range (the cyanide stretches at energies of $\sim$ 260 meV have been omitted). The low-energy phonon branches for $Rb_2Zn(CN)_4$ are noticeably lower since Rb^+ cations have a greater mass than the K^+ cations. In addition, there is a particularly low-energy optic mode at the L-point for $Rb_2Zn(CN)_4$.

Whilst there are no previous phonon calculations for these cyanospinels to compare to directly, multiple Raman and Infrared scattering measurements have been used to probe the Γ-point modes of $K_2Zn(CN)_4$.[166–169] The frequencies observed in Ref. 167 are given in Table 3.3. There is a relatively good agreement between these observed frequencies and the phonon calculations. The CN stretches are at similar frequencies, whilst the quasi-dispersionless bands around 40 meV are also seen experimentally and assigned to Zn–C stretching and Zn–C–N bending modes. The lower frequency modes that are measured are at a higher energy in the final DFT-calculated phonon dispersion curves for $K_2Zn(CN)_4$. The C–Zn–C bending and K^+ ion vibrations are at around $\sim$ 15 meV in the observed Raman and IR measurements compared to $\sim$ 20 meV in the *ab initio* calculation. Similarly, the lowest frequency optic mode observed is at 7.3 meV compared to 12 meV in the DFT phonon calculation. The energy scale of the low-energy modes is probably best captured in the $Rb_2Zn(CN)_4$ phonon dispersion curves.

Table 3.3: Observed Vibrational Frequencies of $K_2Zn(CN)_4$ from Ref.

Symmetry	Mode	Activity	Energy (meV)
CN stretching	A_{1g}	Raman	267.18
CN stretching	T_{2g}	Raman	267.06
Zn–C stretching	T_{1u}	I.R.	44.02
Zn–C stretching	A_{1g}	Raman	42.16
Zn–C–N bending	T_{1u}	I.R.	39.06
Zn–C–N bending	E_g	Raman	38.93
Zn–C–N bending	T_{2g}	Raman	38.93
Vibration of K^+ ion	F_{1u}	I.R.	19.10
C–Zn–C bending	T_{2g}	Raman	18.35
Vibration of K^+ ion	T_{1u}	I.R.	15.75
C–Zn–C bending	E_g	Raman	15.13
Rigid unit vibrations of $[Zn(CN)_4]^{2-}$	T_{2g}	Raman	7.32

3.3.3 Powder INS

The inelastic neutron scattering functions, $S(Q, E)$, were measured on the MARI[123] spectrometer at the ISIS Neutron and Muon Source for polycrystalline samples of $K_2Zn(CN)_4$ and $Rb_2Zn(CN)_4$ at 50 K and 300 K. At each temperature point, two measurements were performed at distinct incident energies (10 meV and 100 meV) each for 6 hours respectively. The plan was to capture the main features of the phonon dispersion relations with the 100 meV measurement, whilst the 10 meV would capture the key low-energy phonon modes at a greater resolution. Background measurements with empty aluminium cans were also carried out. Phonon dispersion curves and the associated neutron-weighted phonon density of states were directly compared to experiment (Fig. 3.5 and Fig. 3.6). Mantid workbench[124,125] was used to perform reconstruction, background subtraction, and normalisation.

The experimental neutron-weighted phonon density of states (DOS) for both $K_2Zn(CN)_4$ and $Rb_2Zn(CN)_4$ were obtained from the powder INS measurements using Mantid by integrating over the whole of reciprocal space. To compare to experiment,

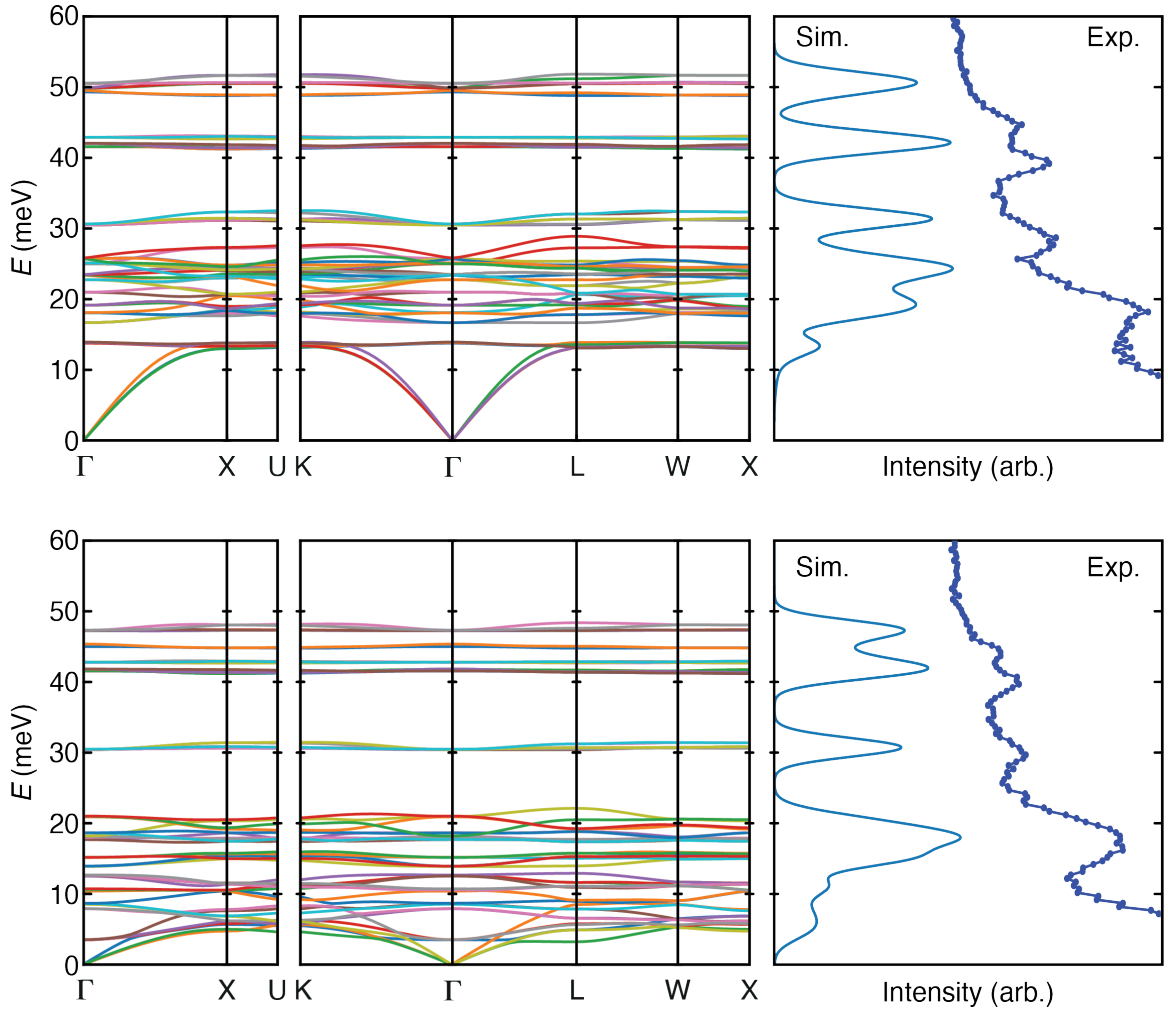

Figure 3.6: Phonon dispersion curves for (a) $K_2Zn(CN)_4$ and (b) $Rb_2Zn(CN)_4$, together with their neutron-weighted DOS compared to experiment.

the DOS were simulated using the *Euphonic* python package. The force constant matrix was extracted from the *Phonopy* calculations by *Euphonic*. Phonon modes were then calculated using a $9 \times 9 \times 9$ MP grid. The energy broadening used was 3 meV as given by the MARI instrument whilst in high-resolution mode (chopper at 400 Hz) and at an incident energy of 100 meV. Both the experimental and *ab initio* DOS are relatively similar for each cyanospinel, with $Rb_2Zn(CN)_4$ having the best match. Unfortunately, the resolution is too poor in the 2 meV region where the low-energy optic mode for $Rb_2Zn(CN)_4$ resides. DFT captures the general features, but the very soft dynamics

such as the L_1^- mode are too low in energy to be probed directly in these measurements.

The inelastic powder scattering maps were also simulated using *Euphonic*.[126,127] The command-line tools were used to simulate MARI-specific coherent neutron weighted powder inelastic scattering patterns. At 300 K, the scattering intensities were too high to observe any distinct bands experimentally. The data shown in Fig. 3.7 were obtained at 50 K. In line with the phonon dispersion curves, both experiment and simulation match well for both in the 10—50 meV range. There are distinct bands at energies of 20 meV, 40 meV, and 50 meV. The important region is that between 0–10 meV since this captures the low-energy dynamics. It is likely that the soft optic modes responsible for the ferroelastic phase transition lie within this region.

Unfortunately, due to the poor resolution of the data, distinct bands are difficult to resolve for both $K_2Zn(CN)_4$ and $Rb_2Zn(CN)_4$, since in this very low-energy regime the elastic line is a problem. The intensities may match better for $Rb_2Zn(CN)_4$ than $K_2Zn(CN)_4$; however, without additional experiments, little other information can be extracted from the data. No phase transitions were observed with the decrease in temperature.

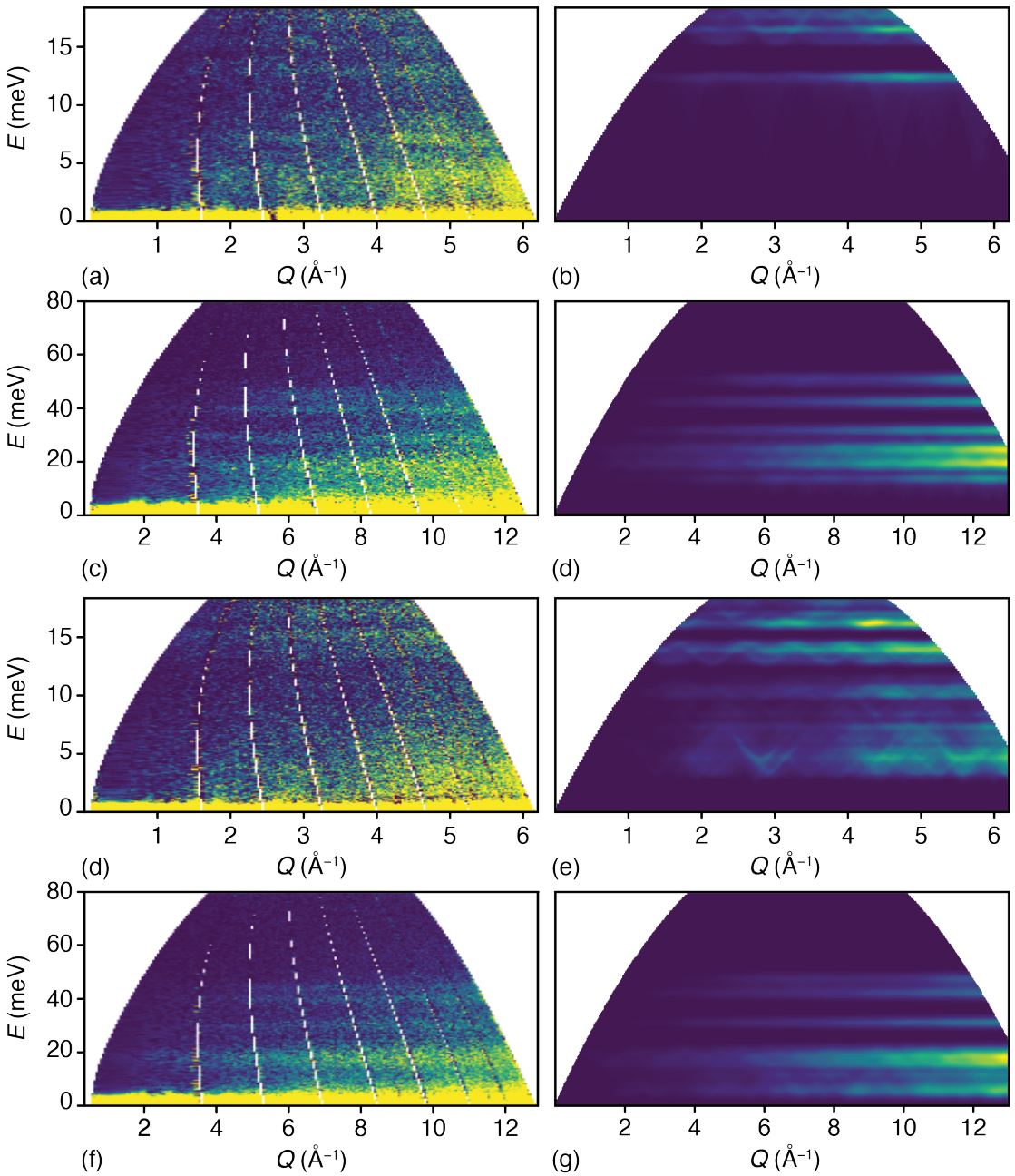

Figure 3.7: Powder INS measurements and the corresponding simulations for $K_2Zn(CN)_4$ ((a)–(d)) and $Rb_2Zn(CN)_4$ ((e)–(g)). The distinct bands are relatively well-matched for $Rb_2Zn(CN)_4$ in the high-energy region of 20–60 meV. Unfortunately, the poor resolution in the low-energy region of interest precludes further analysis of low-energy dynamics.

3.3.4 Single Crystal TDS

Whereas the very low-energy dynamics are obscured in INS by the elastic peak and energy resolution, these modes are the strongest features in TDS. So we turned to TDS to explore further the low-energy dynamics of $K_2Zn(CN)_4$ and $Rb_2Zn(CN)_4$. Single crystals for both cyanospinels were recrystallised from the same powder samples as used for the MARI experiment. Single crystal TDS experiments were then carried out on these single crytsals using a Rigaku XtaLAB Synergy-S Dualflex diffractometer fitted with a Dectris EIGER2 R 1M detector using Cu-K_α radiation ($\lambda = 1.54184\,\text{Å}$) over several hours. For both cases, the expected $Fd\bar{3}m$ reflection conditions were obeyed. The three-dimensional scattering function (Bragg + diffuse) for each crystal was reconstructed and symmetry-averaged. The experimental $hk0$ and hhl planes are shown and qualitatively compared to simulation (Fig. 3.8).

In experimental TDS, the intensity is highest at or near the Bragg points, since the energy of the acoustic modes tends to 0 as $\mathbf{q} \to 0$. In addition, the $hk0$ plane shows streaks of intensity along the $\langle 100 \rangle$ ($\Gamma \to$ X) and $\langle 110 \rangle$ ($\Gamma \to$ K) directions. These streaks of intensity correspond to the low-energies of the TA modes along these paths in reciprocal space (Fig. 3.6). The experimental hhl plane is perhaps even more interesting for these cyanospinels since it contains the $\Gamma \to$ L path. Once again, there are lines of diffuse intensity in the $\langle 110 \rangle$ directions due to the TA modes. In addition, there are TDS lines of intensity along the $\langle 111 \rangle$ directions that correspond to the path along $\Gamma \to$ L in reciprocal space (highlighted in Fig. 3.8). Yet, the TA modes are relatively low-energy in this region and it is difficult to ascertain whether there may be an additional low-energy optic mode such as the L_1^- phonon mode.

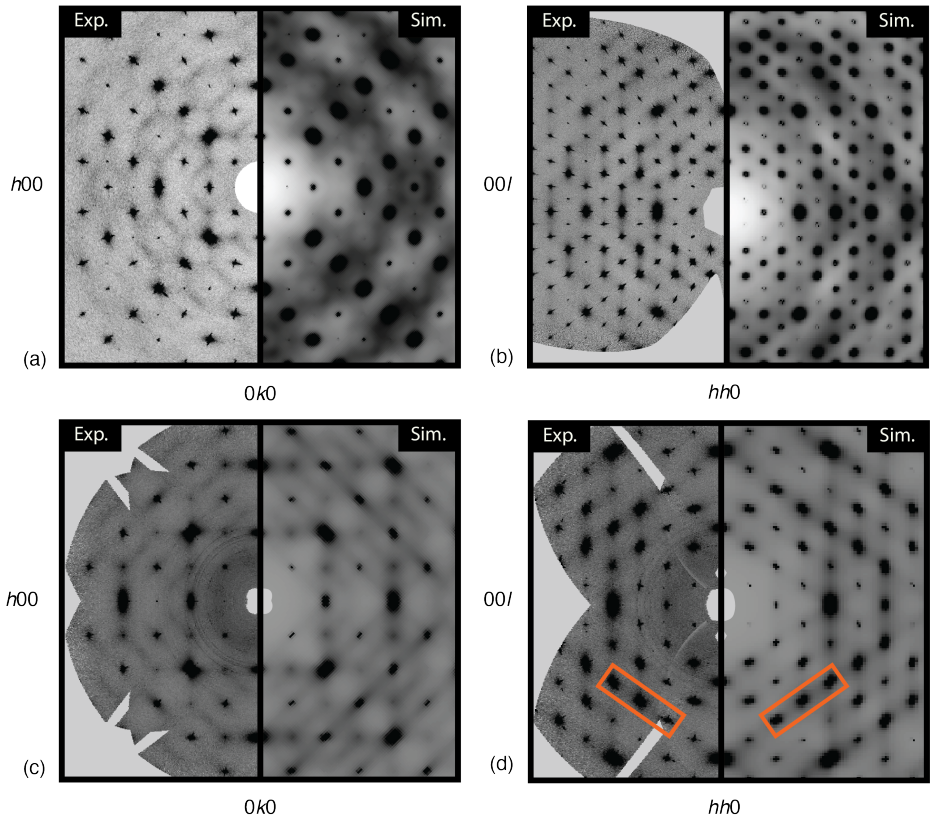

Figure 3.8: Single Crystal TDS Measurements for $K_2Zn(CN)_4$ ((a) and (b)) and $Rb_2Zn(CN)_4$ ((c) and (d)). (a) and (c) are the $hk0$ plane, whilst (b) and (d) are the hhl plane. The orange box highlights a section of TDS intensity along the $\langle 111 \rangle$ directions for both the experimental and simulated scattering patterns.

These experimental results were also qualitatively compared to simulation. These simulated phonon dispersion curves were calculated using the phonon dispersion curves of Fig.3.6 together with the *ab*2*tds* program. From the phonon dispersion curves, the *ab*2*tds* program derives the dynamical matrix. A temperature of 300 K was used for the Debye-Waller factors, and an effective $5 \times 5 \times 5$ **q**-point grid was used. The match between experimental and simulated for $Rb_2Zn(CN)_4$ is particularly good with the streaks of TDS intensity well replicated in both the $hk0$ and hhl planes. For $K_2Zn(CN)_4$ the picture is slightly more nuanced. Here, the streaks of diffuse intensity are less well captured, and perhaps indicate that the TA modes are perhaps too high in energy in the *ab initio* calculation. That the simulated TDS intensity for $K_2Zn(CN)_4$

matches less well with its experimental counterpart is perhaps not too surprising given the previous match for the powder INS measurements and the difficulty with obtaining these phonon dispersion curves for this cyanospinel.

3.3.5 L-point Low-Energy Mode Analysis

Although neither $K_2Zn(CN)_4$ nor $Rb_2Zn(CN)_4$ showed phase transitions when cooled down to 50 K, low-energy optic modes at the L-point hark back to the previous dynamic studies performed on this cyanospinel family.[165] Therefore, the low-energy L-point optic mode of $Rb_2Zn(CN)_4$, clearly present in its DFT-calculated phonon dispersion curves, is perhaps of greatest interest. The DFT-derived eigenvectors of this mode were used to displace the atoms of the high-symmetry $Fd\bar{3}m$ structure of $Rb_2Zn(CN)_4$. The creation of a new, lower-symmetry structure allowed for symmetry analysis using ISODISTORT. The crystal structure of $Rb_2Zn(CN)_4$ was shown to lower in symmetry from $Fd\bar{3}m$ to $R3c$ (rather than $R\bar{3}c$) when this low-energy L-point mode was activated. The atomic displacements of this mode led to slight alternating twists of the $[B(CN)_4]^{2-}$ tetrahedra along the [001] rhombohedral direction coupled with large displacements within the Rb^+ sublattice. These displacements preserve the Rb^+–Rb^+ distances in RUM-like rotations. In fact, the pyrochlore network of A-site cations, introduced at the start of this chapter, is distorting whilst preserving the shape of its constituent Rb_4 tetrahedra. These cooperative rotations occur in the planes of Rb_4 tetrahedra that are perpendicular to the trigonal axis. Interestingly, whilst this DFT-derived L-point mode contains both slight antiphase twists of the $[B(CN)_4]^{2-}$ tetrahedra, it is dominated by displacements of the Rb^+ sublattice.

Importantly, symmetry analysis from ISODISTORT shows how the descent in symmetry from $Fd\bar{3}m \rightarrow R3c$, can only be achieved *via* the activation of two distinct

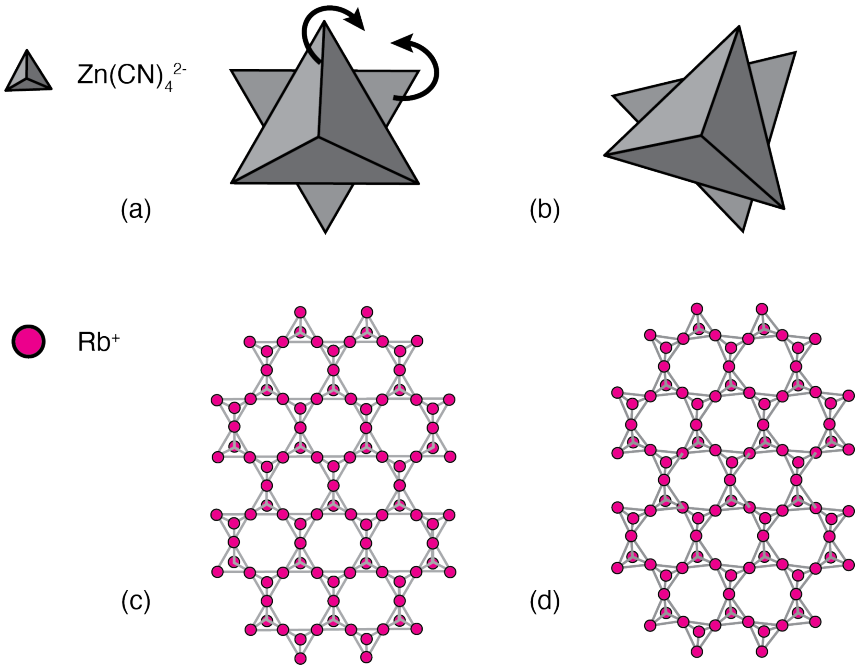

Figure 3.9: The displacements associated with the lowest energy L-point mode for $Rb_2Zn(CN)_4$ viewed down the trigonal axis. (a) and (b) show the correlated twists of the $Zn(CN)_4{}^{2-}$ tetrahedra. (c) and (d) show the quasi RUM-like distortion of the Rb-sublattice.

L-point modes, namely: L_1^- and L_2^+ modes. The L_1^- mode is predominantly associated with Rb^+ displacements, with a slight twisting of the $[M(CN)_4]^{2-}$ tetrahedra. The L_2^+ mode, however, only has slight displacements of the C and N atoms. A distortion driven by either the L_1^- or L_2^+ mode initially lowers the crystal symmetry to $R\bar{3}c$, subsequent activation of the *other* mode finally reduces the symmetry to $R3c$. The low-energy optic mode derived from DFT therefore arises from mixing between these L_1^- and L_2^+ modes. Non-symmetry allowed mode-mixing may occur in *Phonopy* since mode symmetries are not assigned beyond the Γ point. The large Rb^+ displacements within the DFT-derived mode suggest it has a greater L_1^- character. Fig. 3.9 displays the DFT-derived L-point mode and its associated displacements. This DFT-derived mode, with its great L_1^- character, is extremely similar to the one previously ascribed to the ferroelastic phase transition in $K_2Hg(CN)_4$ since both the antiphase tetrahedral

rotations and Rb^+ displacements are present. So, although the $[M(CN)_4]^{2-}$ tetrahedra do rotate, the A-site sublattice plays an important role in the low-energy dynamics of the cyanospinels. Both are important in the key low-energy optic mode that drives the ferroelastic transitions in this family. This opens up a new avenue in tuning these cyanospinels beyond the B-site composition.

3.4 Outlook

The importance of the A-site pyrochlore lattice, and the role it plays in the low-energy dynamics of the cyanospinels is particularly exciting. Mixed compositional series of the A-site cation are relatively easy to realise and have previously been used to vary T_c. Yet, the nature of how these A-site cations substitute into the pyrochlore lattice and how these interact with the low-energy phonon modes remains under-explored. The difference in A-site cation radii for mixed-cation $AA'Zn(CN)_4$ phases may potentially drive a '2-in-2-out' decoration of the pyrochlore lattice, conceptually related to the 'spin-ice' phases of frustrated magnets.[175,179] $CsNiCrF_6$ is an example of a compositional ice in the 'multiple Coulomb phase'.[176] In that system, the interplay of correlated compositional disorder and magnetism leads to a variety of unusual physics. In the case of non-magnetic $AA'Zn(CN)_4$, the correlated compositional disorder could influence the low-energy lattice dynamics in new and interesting ways. For example, one could hope to establish whether ice-like disorder frustrates low-energy optic mode instabilities and/or is effective in reducing phonon lifetimes for a new thermoelectric material design strategy. One could potentially realise cyanospinel 'compositional-ice' phases in which one has particularly strong control over the presence and nature of correlated compositional disorder and the corresponding dynamics.[177–179] This plays into the goal of establishing robust disorder-property relationships in functional

materials. With a good handle on the end-members of these series, it makes sense to explore the mixed compositional-ice candidates in the $K_xRb_{2-x}Zn(CN)_4$ series. By learning how particular types of disorder can influence lattice dynamics (amongst other collective properties) in non-trivial ways, one can direct materials design in a variety of fields including thermoelectrics and barocalorics.[109]

4

Dicalcium Barium Propionate: a Hybrid Cristobalite

4.1 Introduction and Acknowledgements

Quasi-RUM-like motion of the cation sublattice was shown to be key in the dynamics and phase transitions of the cyanospinels in the previous chapter. A similar story emerges for dicalcium barium propionate (DBP). DBP ($Ca_2Ba(C_2H_5OO)_6$) is a complex system that shows diffuse scattering which has been attributed to both the disorder in the propionate linkers and distortions of the cation network itself. I will come to show that its pyrochlore cation framework plays a crucial role in its diffuse scattering and ferroelastic phase transition.

This chapter shows the power of coarse-graining to understand the dynamics of systems where complexity prevents *ab initio* calculations. Parallels are drawn between the $BaCa_2$ cation framework of DBP and SiO_2 cristobalite. The high temperature phase of DBP is exactly analogous to β-cristobalite ($Fd\bar{3}m$), whilst the low temperature structure ($Pnma$) is related but distinct from α-cristobalite ($P4_12_12$). This analogy allows us to exploit efficient SiO_2 potentials as a proxy for modelling the thermal behaviour of the cation sublattice in DBP. Configurations from MD simulations are used to simulate TDS patterns that can then be compared to experiment. After symmetry analysis, quasi-RUM-like mode distortions of the cation sublattice are found to be key.

This study on the diffuse scattering of DBP is part of a broader project and collaboration with Professor Gregor Kieslich's group. All syntheses were carried out

at TU Munich. The thermal diffuse scattering measurements were performed in-house together with Ms Shinjoo Park, a then Master's student from the Kieslich group group who stayed in Oxford for a month.

4.2 Background

4.2.1 The Dicalcium Metal Propionate family

The dicalcium metal propionate family ($Ca_2M(C_3H_5OO)_6$ where M = metal) has been studied extensively, originally for its members' phase transitions and the presence of ferroelectric phases.[181,182] Both the metal (Ba, Sr, Pb) and the linker (propionate, acrylate, hexacrylate, butylate) can be substituted.[180] This family, therefore, has a rich variety of structures with their own corresponding phase transitions and ferroelectric phases[183] (Fig. 4.1).

Historically, compounds such as dicalcium strontium propionate (DSP) were of greatest interest in this family, since these were shown to have ferroelectric phases at atmospheric pressure. The room temperature structure of DSP adopts the chiral tetragonal space group of $P4_12_12$ symmetry and undergoes a ferroelectric transition below 281 K.[184] The focus of this chapter is on dicalcium barium propionate, (DBP), which adopts the $Fd\bar{3}m$ cubic aristotype for the dicalcium metal propionate family.[185] DBP undergoes two phase transitions at atmospheric pressure – one is an $Fd\bar{3}m \rightarrow Pnma$ first-order transition at 267 K,[186,187] while the second is a $Pnma \rightarrow P2_12_12_1$ second-order transition at 204 K.[188,189] DBP has also been shown to undergo a ferroelectric transition under high pressure.[190,191] More recently for DBP, its phase transitions and their associated large changes in entropy ($39.6\,J\,K^{-1}\,kg^{-1}$) under small hydrostatic pressures have made it a candidate of interest as a solid-state barocaloric.[192]

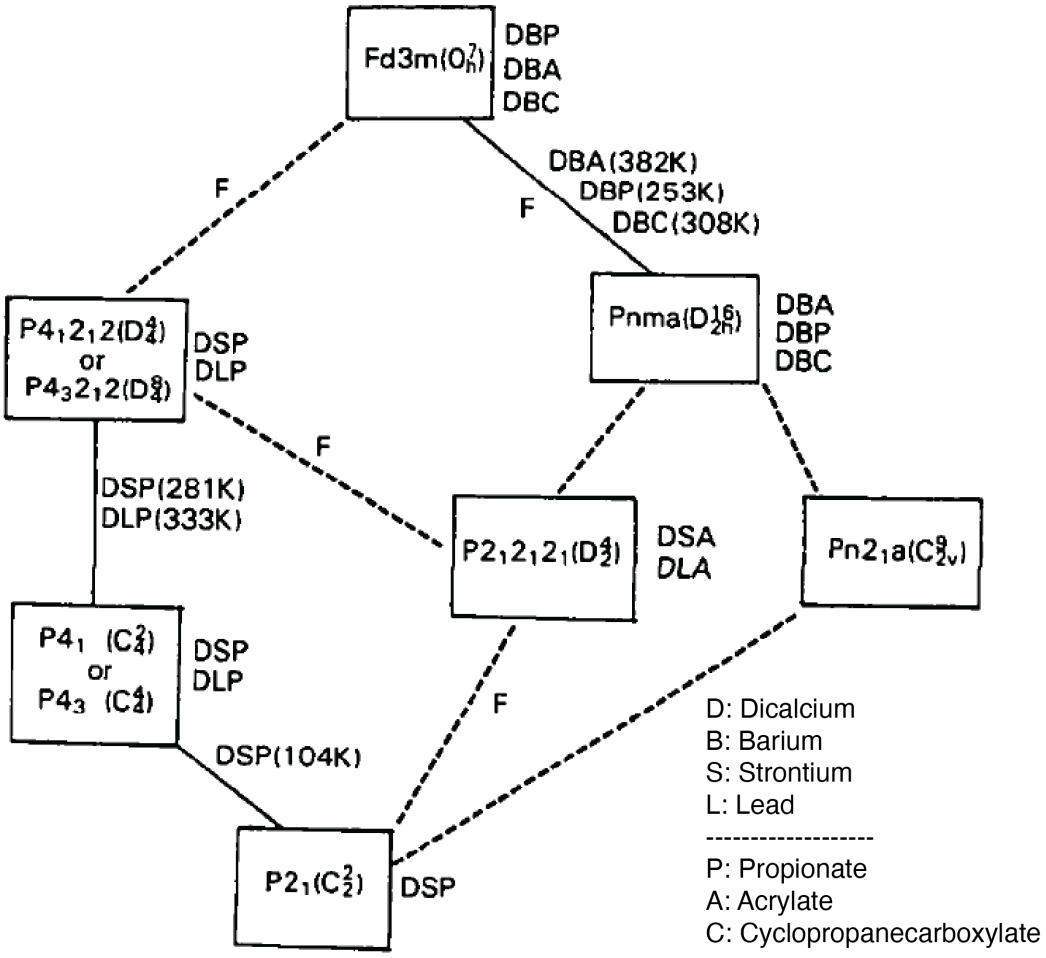

Figure 4.1: Schematic diagram of successive phases for the dicalcium metal propionates, acrylates, and carboxylates. The solid lines indicate known transitions and dashed lines potential continuous phase transitions, so far unreported. The letter F denotes a ferroelastic phase transition. Figure reproduced with permission from Ref. 180.

4.2.2 The Structure of DBP

DBP was first synthesised in the late 19$^{\text{th}}$ century,[193] and its $Fd\bar{3}m$ space group assigned in 1935.[194,195] The Ba^{2+} cations form a diamond-like framework occupying the 8*a* Wyckoff positions. Propionate linkers mediate the interactions between the Ba^{2+} and Ca^{2+} ions. These propionates exhibit significant disorder.[185] Indeed, the two-fold axes of the $Fd\bar{3}m$ space group imply a statistical two-site symmetry-imposed disorder of the

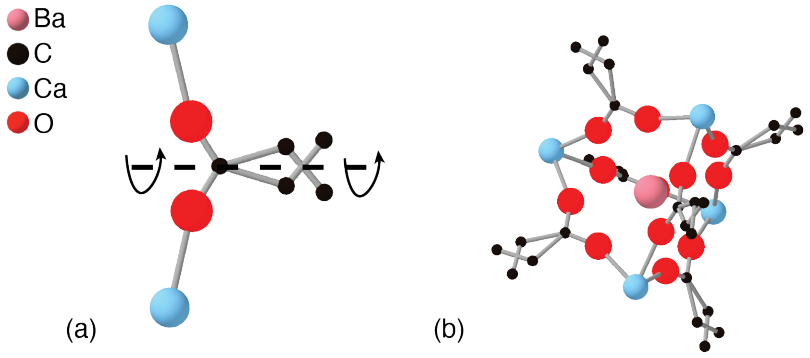

Figure 4.2: (a) Propionate linker and its pseudo-two-fold axis when disordered over two orientations. (b) The tetrahedron building unit found in DBP, composed of four Ca^{2+} cations, propionate linkers and a Ba^{2+} cation that resides inside it.

propionate group about its long axis (Fig. 4.2 (a)). Each Ba^{2+} cation can be considered to reside within a tetrahedron defined by its four nearest Ca^{2+} cations together with its nearest propionate linkers (Fig. 4.2 (b)). These tetrahedra are edge-sharing and form a pyrochlore lattice. The inherent disorder of the propionate linkers can make representations of the average unit cell difficult to interpret. For clarity, Fig. 4.3((a)—(f)) illustrates the structure of DBP both with and without the propionate linkers.

4.2.3 X-ray Diffuse Scattering

DBP displays significant diffuse scattering, and its underlying microscopic origin remains of significant debate. Single crystal X-ray diffuse scattering studies of DBP showed streaks of intensity elongated along the $[\bar{1}10]$ directions that passed through the reflections in the $(hk0)$ plane given by $h + k = 8n$[196] (Fig. **??**).

The diffuse scattering intensity was originally rationalised as a signature of large amplitude librational modes about the pseudo-two-fold axes of the propionate linkers. This motion was described as coupled between adjacent propionate groups. These modes, together with short-range ordering of the propionate linkers in the $\langle 110 \rangle$

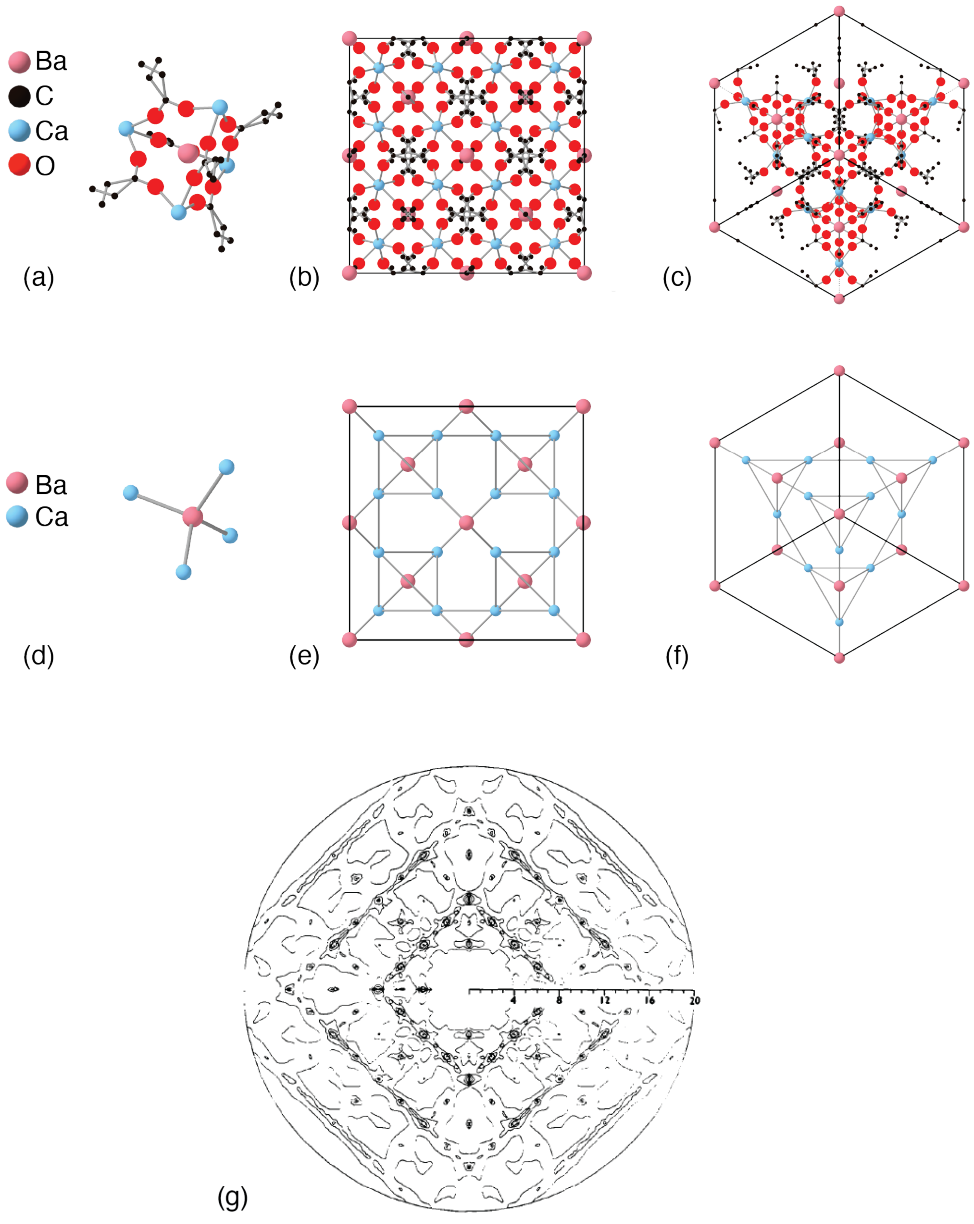

Figure 4.3: Structure of DBP with ((a)—(c)) and without ((d)—(f)) its propionate linkers. The tetrahedra ((a) and (d)), and views along the [100] ((b) and (e)) and [111] directions ((c) and (f)) are shown for both. The X-ray diffuse scattering for DBP in the $hk0$ plane of DBP is shown as (g)—reproduced with permission from Ref. 196.

directions were assigned as key for the diffuse scattering. ^{1}H NMR studies have shown that the propionate motions differ significantly after the phase transition.[197] As a result, it has been proposed that the C_2H_5 motion drives the phase transition behaviour of DBP. A recent thesis asserted that the phase transition in DBP 'originates from thermal changes in the carbon chains' and that 'the cage made of Ca^{2+} and Ba^{2+} ions changes shape only due to the changes in the carbon chain molecules'.[192]

4.2.4 The Cation Framework is Key

Yet, already 40 years ago, an optical transform study demonstrated that it was the displacement of the cations, and not the orientations of the propionate groups, that contributed most strongly to the diffuse scattering.[198] Intuitively, the atomic scattering factors of Ba^{2+} and Ca^{2+} ions should provide a much larger contribution to the overall scattering intensity than the propionate groups. In this thorough study, different short-range orderings of propionate groups were used and shown not to result in the diffuse scattering patterns measured experimentally. Indeed, local growth models incorporating Ba-Ca sublattice distortions best replicated the diffuse streaks. These growth models used displacements allowed by the lower symmetry, chiral framework of the Sr analogue (DSP). These locally orthorhombic configurations led to a good match for the diffuse scattering (Fig. 4.4).

Since then, models have described the thermal parameters of Ca^{2+} and Ba^{2+} ions in DBP as a superposition of the chiral states produced by $P4_12_12$ and $P4_32_12$ whilst maintaining the three-fold rotations about the cubic [111] axes.[180,183] In this picture, the high symmetry structure of DBP is simply the average over all the chiral microdomains from which it is formed.

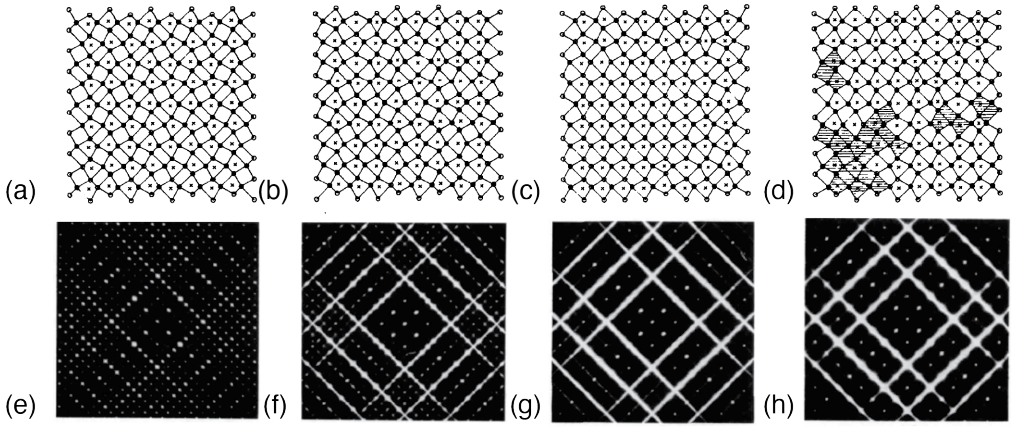

Figure 4.4: Different growth models using distortions allowed by the chiral framework of DSP ((a)–(d)) and their corresponding diffuse scattering viewed along the ($hk0$) plane ((e)–(h)). Figure adapted and reproduced with permission from Ref. 198.

4.2.5 Similarity to β-Cristobalite

This conclusion is reminiscent of the historical debate on the disorder present in β-cristobalite. β-cristobalite also adopts $Fd\bar{3}m$ symmetry, with its low-temperature α-phase adopting the chiral $P4_12_12$ space group. The average structure of $Fd\bar{3}m$ symmetry contains unphysical Si–O–Si linkages at angles of 180° rather than the expected angle of 104.5°. Instead, it was proposed that the high symmetry structure of β-cristobalite was composed of many small domains of the low-temperature phase or other lower symmetry space groups.[66,199] The problem with these interpretations is the high energy penalty of distorting SiO_4 tetrahedra required for these domains to form. The alternative RUM model elegantly showed how a superposition of low-energy RUMs over all wave-vectors could lead to the same disorder and associated diffuse scattering with minimal distortion of the tetrahedra.[32,200] For β-cristobalite, there is one RUM for each wave-vector of the form (ξ, ξ, ζ) which lie in the $\langle 1\bar{1}0 \rangle$ zones of reciprocal space.[28,200,201] RUMs that lie in these zones can replicate the distortions of previous domain models. For α-cristobalite for example, the distortion required is a doubly-degenerate RUM at wave-vector (1,0,0). All previous domain models can exist

as superposed RUM-type fluctuations of β-cristobalite. Perhaps more importantly, all other distortions associated with other RUMs in the $\langle 1, \bar{1}, 0 \rangle$ zones of reciprocal space can be activated, leading to a dynamically disordered structure. Following this RUM model through, the phase transition from $\beta \rightarrow \alpha$ for cristobalite may be due to the softening of different RUMs.[27,201]

The concept of RUM-driven disorder may also be applicable to DBP. Although both the high-temperature phases of DBP and cristobalite share the same symmetry, parallels can also be drawn between the tetrahedra of $BaCa_4$ and SiO_4, although the interactions between Ba–Ca are mediated by propionate linkers rather than direct bonds (Fig. 4.5). The RUMs in β-cristobalite can lead to a variety of different symmetry lowerings. The α-cristobalite structure is one possibility; the *Pnma* structure of DBP is another. So whilst the low temperature phase of DBP has *Pnma* symmetry, the RUM model can still be applied effectively. In this RUM model picture, the first-order phase transition for DBP may also result from the softening of RUM-like modes similar to those in β-cristobalite. Previous NMR and EPR studies attributed DBP's phase transition to its propionate linkers rather than cation framework distortions, citing the large entropy change and increased amplitude of propionate motion across the

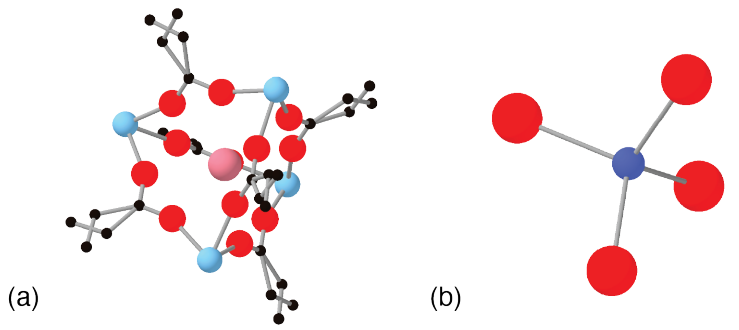

Figure 4.5: (a) $BaCa_4$ tetrahedron (with the disordered propionate linkers) in DBP compared to (b) the SiO_4 tetrahedron found in SiO_2 systems.

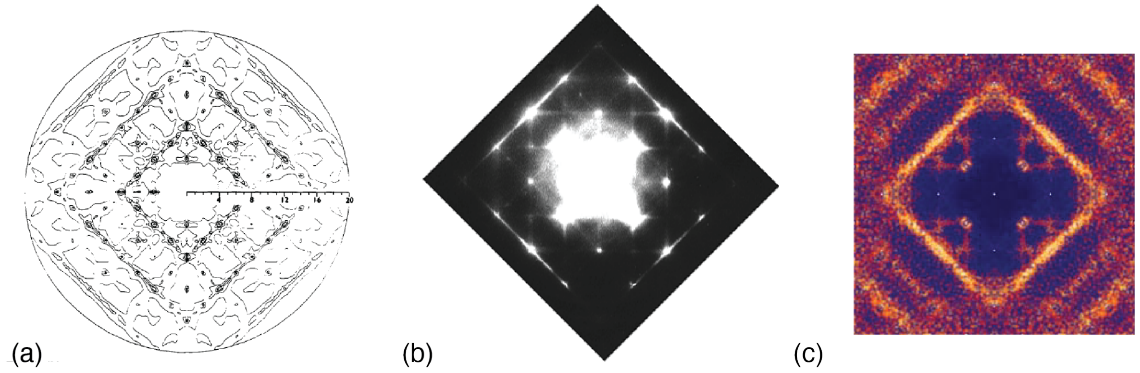

Figure 4.6: (a) X-ray diffuse scattering of DBP, (b) Electron diffuse scattering of β-cristobalite measured using a TEM, and (c) simulated diffuse scattering of β-cristobalite from MD. Figures reproduced with permission from Ref. 196, Ref. 204, and Ref. 201 respectively.

transition.[202,203] Yet, the RUM model could also provide an alternative and consistent explanation. The distortion of the cation framework and change in symmetry from $Pnma \rightarrow Fd\bar{3}m$ would allow the propionate groups to librate more fully and hence also result in a large entropy change.

A next step to take would be to calculate the possible quasi-RUM-like modes for the BaCa4 framework and output its associated TDS. Yet, bar the difference in atomic scattering factors, one can simply compare its experimental TDS to that of β-cristobalite. Indeed, the shape of the diffuse scattering is very similar between them (Fig. 4.6).

Alternatively, the complete phonon dispersion curves for DBP and associated TDS could be simulated *via* DFT calculations. The large DBP supercells required, however make this prohibitively computationally expensive. Moreover, the lack of accurate interatomic potentials for DBP precludes direct MD simulations.

Instead, we explore here the extent to which DBP can be thought of as a hybrid cristobalite. This would help to solve the disorder conundrum of DBP and elucidate the

driving force for the first-order phase transitions (whether these are soft-phonon mode driven or order-disorder transitions). This coarse-graining allows us to remove the associated linker complexity and find the key framework distortions. More importantly, this abstraction allows us to leverage the extensive research on cristobalite and apply it to DBP and its family. The importance of establishing 'hybrid' analogies should not be understated. The rational materials design of hyrbid perovskites, for example, has been greatly accelerated by building on previous work on the original, inorganic ABX_3 systems. Well-established frameworks such as the Goldschmidt tolerance factor together with the description of octahedral tilts (and associated Glazer notation) originally developed for inorganic perovskites have been widely and successfully adopted for research on their hybrid analogues.

4.3 Results

If DBP is truly analogous to the cristobalite system, at least in its dynamics, one should be able to use SiO_2 potentials to replicate its behaviour. We wanted to collect modern X-ray TDS measurements and explore recent advances in the development of high quality machine-learned interatomic SiO_2 potentials to test this analogy between DBP and SiO_2. In addition, the configurations from the MD simulations can be used to simulate the TDS of DBP and qualitatively compared to experiment. The diffuse scattering measurements of this chapter were collected at 300 K with Mo-K_α radiation ($\lambda = 0.7107$ Å) and using DBP crystals synthesised by collaborators from the Kieslich group at TU Munich.

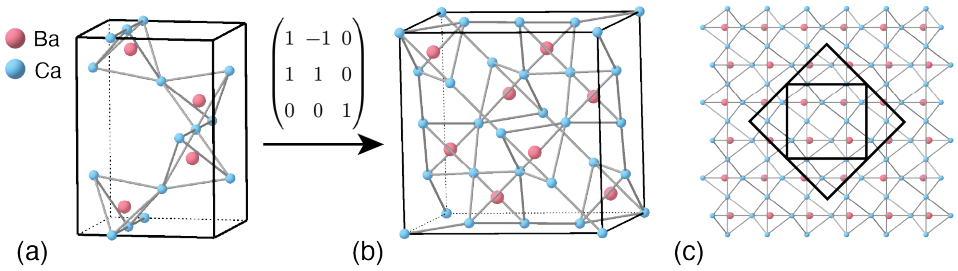

Figure 4.7: The matrix transformation from the orthorhombic *Pnma* unit cell (a) to the cubic unit cell (b) that retains the space group symmetry. The relation between the two unit cells is shown with a view along the [001] direction in (c). The matrix transformation scales the a and b lattice parameters by a factor of $\sqrt{2}$ and rotates them by 45° about the c-axis.

4.3.1 MD Simulation of SiO_2 from $Pnma \rightarrow Fd\bar{3}m$

Using a general, recent, and robust machine-learned potential of SiO_2, MD simulations of SiO_2 with *Pnma* symmetry (low-temperature DBP) were run with a heating rate of 2.5 K/ps from 100 K to 1450 K using LAMMPS.[144,205] For the MD simulation, the initial starting configuration was a supercell containing 1536 atoms. To construct this supercell, an orthorhombic *Pnma* unit cell of SiO_2 was transformed to a larger cubic unit cell that retained *Pnma* symmetry. This was achieved with the matrix transformation shown in Fig. 4.7. The a and b lattice parameters of the original orthorhombic cell were scaled by a factor of $\sqrt{2}$, and rotated by 45° about the c-axis. The c lattice parameter remained unchanged. This new cubic unit cell contained eight SiO_2 units instead of four in the original orthorhombic unit cell. As a result, the initial configuration was simply a $4 \times 4 \times 4$ supercell of this cubic unit cell with *Pnma* symmetry.

This starting configuration was kept at 100 K for 5 ps for equilibration before being heated at a constant rate of 2.5 K/ps. A Parrinello–Rahman barostat[206] was used for the *NPT* simulation with a time step of 1 fs, a temperature damping constant of 100 fs, and a pressure damping constant of 100 fs. Fig. 4.8 shows the evolution of

the dimensions of the supercell with temperature. For an orthorhombic *Pnma* unit cell, the cell angles are fixed ($\alpha = \beta = \gamma = 90°$) while the cell lattice parameters are allowed to vary ($a \neq b \neq c$). Since the SiO_2 supercell is composed of cubes of *Pnma* symmetry, it has three degrees of freedom in its cell dimensions. These are distributed differently from those of the orthorhombic *Pnma* unit cell as a result of the 45° rotation of the *a*- and *b*-axes when forming the cubic unit cell. This leads to the supercell having the following degrees of freedom: $a = b \neq c$ and $\alpha = \beta \neq \gamma = 90°$, noting that there are still three degrees of freedom overall. This allows us to track phase transitions to higher-symmetry structures. For example, cubic $Fd\bar{3}m$ symmetry would force the supercell dimensions to have $a = b = c$ and $\alpha = \beta = \gamma = 90°$.

Looking at Fig. 4.8, the supercell retains *Pnma* symmetry until around 453 K when it undergoes a phase transition to cubic symmetry. The temperature of the phase transition is below the temperature range of the α–β cristobalite transition (540 K for synthetic)[207] since the *Pnma* structure is of higher energy than that of α-cristobalite for the SiO_2 system. In addition, a precise transition temperature (T_c) for α–β cristobalite is difficult to ascertain since this can vary between samples and with the sample history. Indeed, in experimental synthetic samples, there is a temperature interval of $\sim$20–40 K for the phase transition depending on crystallite size, structure, and composition.[208–210] Furthermore, the α and β phases have been shown to coexist over a temperature interval.[211–213] Since the transition from $Pnma \rightarrow Fd\bar{3}m$ may involve similar tetrahedral distortions to that of the α–β transition, it is not surprising that the T_c for both are relatively close.[214,215]

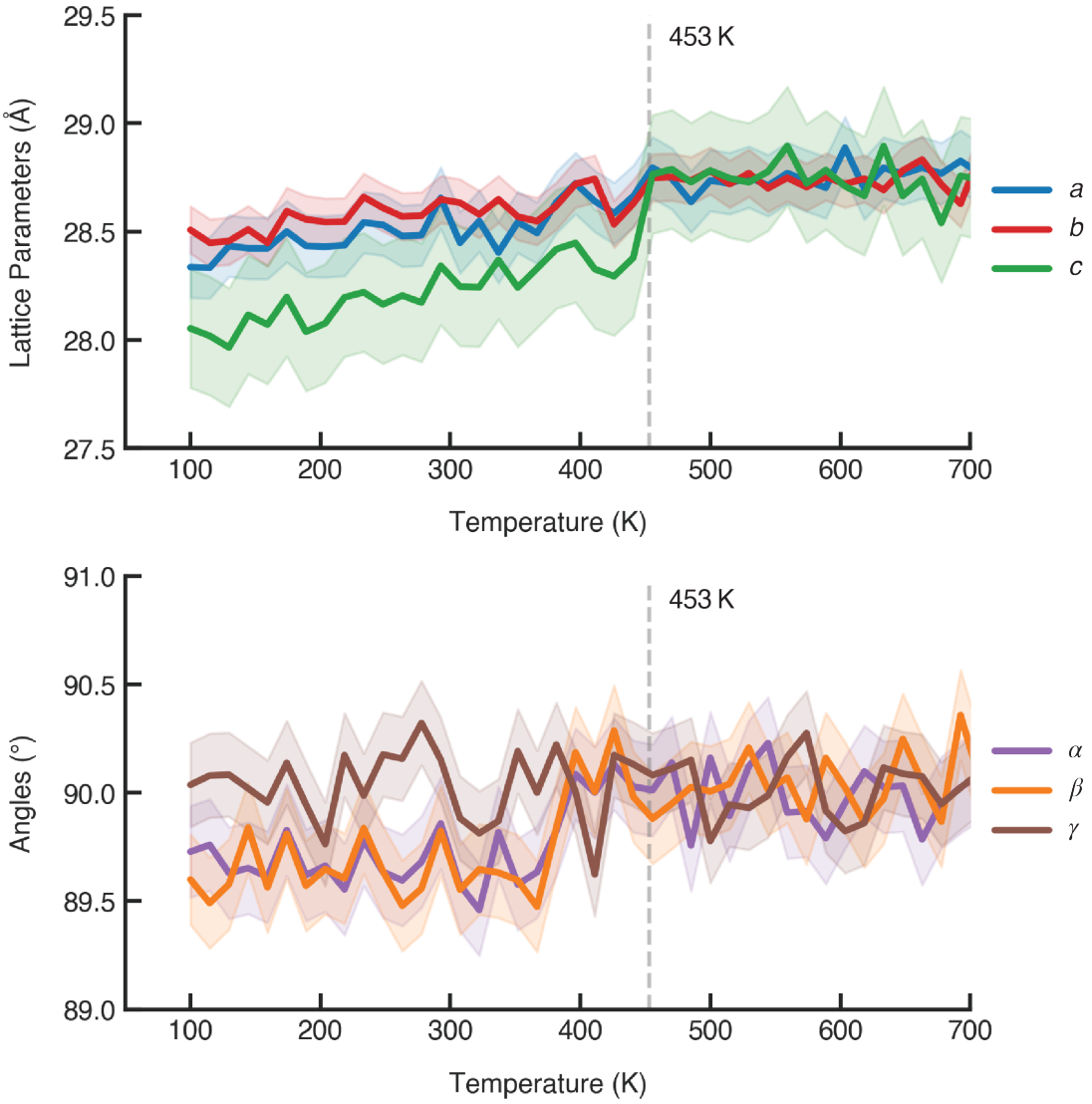

Figure 4.8: (a) Evolution of the lattice parameters and (b) of the angles of the supercell with temperature across the MD run. There is a phase transition from orthorhombic to cubic at approximately 453 K.

4.3.2 A Closer Look at the Phase Transition

To visualise exactly what is occurring at an atomic level during the phase transition, snapshots of the supercells were taken within the 350 K to 500 K temperature range at 50 K intervals (Fig. 4.9). For the four temperatures sampled, there is a view down the [100] ((a)–(d)), the [110] ((e)–(h)), and their respective radial distribution functions ((i)–(l)). Below the phase transition at 350 K, the *Pnma* symmetry and domains are

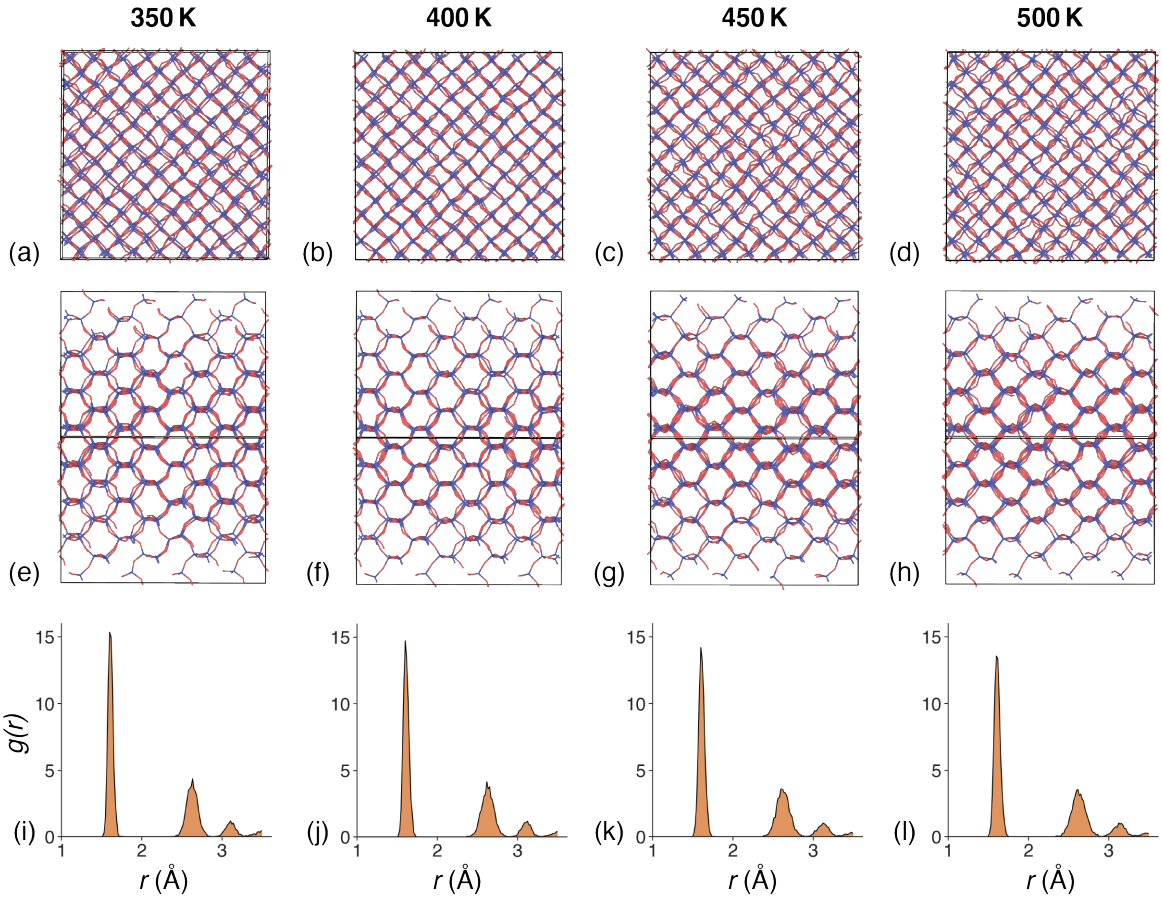

Figure 4.9: Four supercells at temperatures around T_c. For each supercell, there is a view down the [100] ((a)–(d)), the [110] ((e)–(h)) and their respective radial distribution functions ((i)–(l)). This gives an atomic representation of how the $Pnma \rightarrow Fd\bar{3}m$ transition occurs.

clear to see in both the [100] and [110] views. Perhaps of greatest interest are the supercells at 400 K and 450 K looking along the [110] direction. When traversing the phase transition, the *Pnma* domains are lost to correlated tetrahedral motions. The supercell becomes progressively more symmetric as the temperature increases. At 500 K the supercell now has an overall $Fd\bar{3}m$ space group symmetry. The radial distribution functions below show how the Si–O, O–O and Si–Si distances are maintained during the phase transition. The local environments and tetrahedra are distorting minimally, lending credence to the RUM model for this $Pnma \rightarrow Fd\bar{3}m$ phase transition.

4.3.3 Experimental Diffuse Scattering

Single crystal TDS measurements were measured at 300 K ($\sim$ 33 K above the reported T_c for DBP) on the in-house lab diffractometer. The experimental $hk0$ and hhl planes are shown in the bottom right quadrant of Fig. 4.10. The most intense Bragg reflections are consistent with a high-temperature cubic $Fd\bar{3}m$ structure for DBP. There are, however, additional small superstructure peaks of intensity. These peaks may indicate that the phase transition may not be complete at 300 K for these measured DBP single crystals and that domains of $Pnma$ symmetry may still persist at 300 K. The diffuse scattering in the $hk0$ plane is qualitatively similar to previous measurements: it contains streaks of diffuse intensity along the $\langle 110 \rangle$ directions (Fig. **??**). For the hhl plane, lines of TDS intensity appear prominently along the $\langle 111 \rangle$ directions, with some small streaks of TDS also along the $\langle 001 \rangle$ directions.

Diffuse scattering from the MD runs was simulated to compare directly with the experimental, in-house single crystal diffuse scattering measurements of DBP. Snapshots along the MD run were taken, the unit cell was scaled (lattice parameters were multiplied by 2.5), and the Si and O atoms were replaced by Ba and Ca, respectively. For each temperature, 16 different configurations at intervals of 200 fs (8 K interval range) were used. Their Fourier transforms were averaged using *Scatty* and compared to the experimentally obtained diffuse scattering (Fig. 4.10).[121] *Scatty* allows for fast Fourier transforms and averaging of diffuse scattering patterns. For better comparison of the TDS intensity, there are no Bragg reflections in the simulated diffuse scattering planes.

Three temperature points were used: $0.5\,T_c$ (corresponding to the low-symmetry $Pnma$ structure), T_c (during the phase transition interval), and $1.1\,T_c$ (the $Fd\bar{3}m$

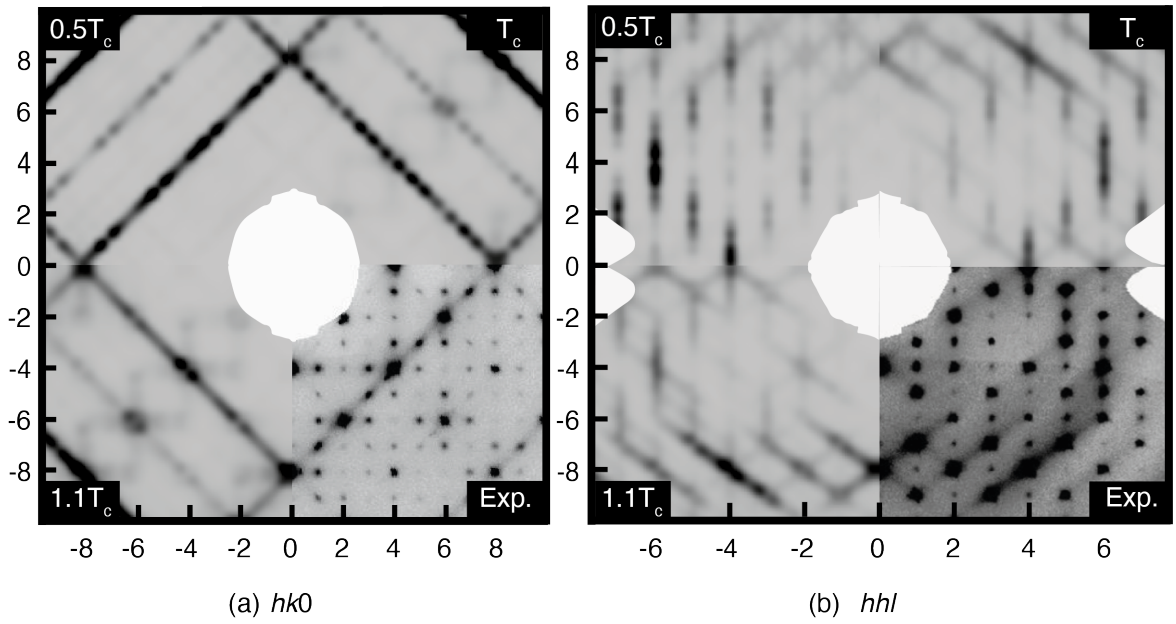

Figure 4.10: $hk0$ plane and hhl planes of thermal diffuse scattering for DBP. Simulated planes are at temperatures of $0.5\,T_c$, T_c, $1.1\,T_c$ whilst the experimental TDS planes (inset) were measured at at 300 K.

regime). For the $hk0$ plane, all temperature points have streaks of TDS intensity along the $\langle 110 \rangle$ directions and a consistent with the experimental and previous measured data. Yet, the hhl plane provides better and clearer comparison. Whilst the simulated scattering of the low-temperature ($0.5\,T_c$) *Pnma* structure does not have lines of TDS intensity along the $\langle 111 \rangle$ directions, both the T_c and $1.1\,T_c$ structures do and provide a better match to the experimental measurements. The T_c configurations provide a better match for the vertical lines of TDS in the hhl plane compared to the $1.1\,T_c$ counterparts, but it is difficult to be conclusive on such a qualitative comparison of TDS. Importantly, this study demonstrates that the diffuse scattering of DBP can all be accounted for by the vibrations and distortions of the cation framework. Whilst the propionate linker motions may affect the cation framework (and vice versa), these are not required. Whilst the importance of the cation framework is in agreement with the previous optical transform study, this model shows how the diffuse can be

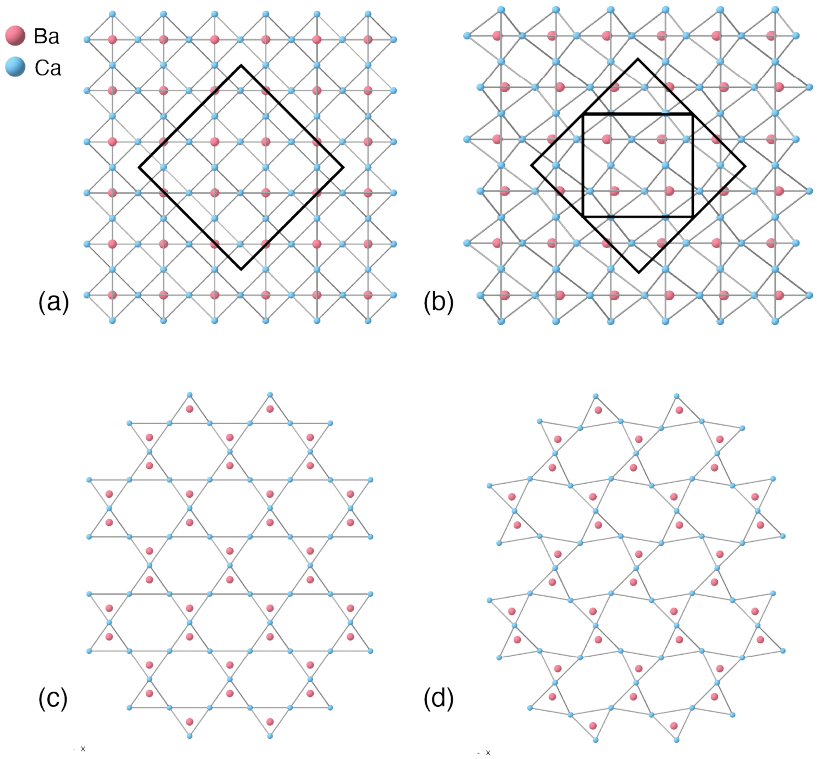

Figure 4.11: Cation framework of DBP in both $Fd\bar{3}m$ ((a) and (c)) and $Pnma$ symmetry ((b) and (d)) looking down the [001] ((a) and (b)) and [010] ((c) and (d)) directions of the orthorhombic cell. Only a quasi-RUM–like distortion is required for the phase transition. Both the orthorhombic and cubic unit cells are displayed as solid black lines in (a) and (b). The distortion is similar to that for cristobalite shown in Fig. 1.4

achieved through atomic vibrations rather than static local growth models. In addition, this dynamic behaviour of the cation framework of Ba^{2+} and Ca^{2+} ions can now be considered as analogous to that of cristobalite.

4.3.4 Symmetry Analysis of the Cation Framework Distortions

Symmetry analysis from $Fd\bar{3}m$ to $Pnma$ using ISODISTORT provides further detail. The modes required for the distortion are similar to those required for the α–β phase transition for cristobalite. After reducing the symmetry from $Fd\bar{3}m$ to $Pnma$ there are several Γ-point modes (Γ_1^+, Γ_3^+, Γ_5^+), yet there is one symmetry-allowed mode that is the primary order parameter, and that drives the distortion: the X_4 mode.

This mode is active at the X-point ((1,0,0) wave-vector).

Interestingly, the Ba–Ca and Ca–Ca distances are preserved when this mode is activated, such that the $BaCa_4$ "tetrahedra" are minimally distorted. This distortion could therefore be considered RUM-like (Fig. 4.11). Conserving the distances between the Ba^{2+} and Ca^{2+} cations probably keeps the energy of this phonon mode low, and underscores the key role of the cation framework in the dynamics of DBP and its family. For β-cristobalite, its calculated phonon dispersion curves support two low-energy RUMs along the $\langle 100 \rangle$ directions and three RUMs along the $\langle 111 \rangle$. Assuming the cation framework of DBP contributes similar phonon modes, it is perhaps the softening of one of these RUM-like motions at the X-point that is driving the phase transition. For DSP, the Sr analogue of DBP that adopts a *Pnma* low-temperature structure, the softening of two RUMs at the X-point are required as for the $\beta \rightarrow \alpha$ transition in cristobalite.

4.4 Outlook

This chapter has readdressed the microscopic origin of the diffuse scattering of DBP. The diffuse scattering is predominantly dynamic and arises from the cation framework. Our results support the identification of DBP as a hybrid cristobalite with respect to its dynamics and phase transition behaviour. One can build on the extensive studies on cristobalite and use these on DBP and its related systems. In addition, the organic linkers that couple to the cation framework are likely key for the large entropic changes that occur during the phase transitions. Substitution of these organic linkers and the metal centres should lead to a family of highly tuneable compounds with a wide-range of applications, particularly in the field of solid-state barocalorics.

5

Negative Thermal Expansion in Transition Metal Dicyanides: the Hidden Role of the Underlying Diamondoid Framework

5.1 Introduction and Acknowledgements

This chapter highlights the potential insight gained by coarse-graining the complex lattice dynamics of framework materials in terms of so-called 'framework modes'—the correlated distortions of the underlying network structure itself. Indeed, even for 'simple' structures (compared to DBP and the cyanospinels), abstraction can be key in truly understanding their lattice dynamics and temperature-dependent behaviour.

This chapter focuses on the transition metal dicyanides $M(CN)_2$ (M = Zn, Cd) and their large isotropic NTE behaviour. The conventional picture of the NTE mechanism in this family is one of correlated rotations and translations of $M(C/N)_4$ polyhedra acting to draw the diamondoid network of M–CN–M linkages in on itself. An implication of this mechanism is increased transverse vibrational motion of C and N atoms relative to the isotropic displacements of M atoms, which act as anchors. In this chapter, a combination of neutron total scattering measurements and *ab initio* calculations is used to reassess the vibrational behaviour of the $M(CN)_2$ family. It is found that M, C, and N atoms all exhibit similar degrees of local thermal motion, such that the cyanide linkages behave as pseudo-springs connecting M$\cdots$M pairs. This interpretation uncovers a 'hidden' dispersion in the $M(CN)_2$ phonon dispersions that is closely related to that of diamond and silicon themselves. By virtue of this

mapping, a simple geometric model based on the competing energy scales of network stretching and flexing—long applied to interpret NTE modes in C and Si—can capture the key NTE physics of $M(CN)_2$, especially at low temperatures.

Experimental neutron scattering data for isotopically-enriched $^{114}Cd(CN)_2$ were measured at 300 K using the POLARIS instrument at ISIS by Dr Chloe S. Coates with instrument scientists Dr Ronald I. Smith, Dr Helen Y. Playford and Dr David A. Keen. The experimental neutron total scattering data fits were carried out by Mr Henry Patteson. The work in this chapter formed the following publication:

Q. Guéroult, J. M. Bulled, H. Patteson, C. S. Coates, R. I. Smith, H. Y. Playford, D. A. Keen, A. L. Goodwin, "Negative thermal expansion in transition metal dicyanides: the hidden role of the underlying diamondoid framework," arXiv:2406.11381 [cond-mat.mtrl-sci], 2024.

5.2 Background

5.2.1 Structure of $Zn(CN)_2$ and $Cd(CN)_2$

Both $Zn(CN)_2$ and $Cd(CN)_2$ have relatively simple structures at ambient temperature and atmospheric pressure. The metal centres are tetrahedrally coordinated to the cyanide ions to form a pair of interpenetrating diamondoid networks (Fig. 5.1 (a)–(b)).[216,217] In this anti-cuprite structure, the cyanide anions exhibit head-to-tail orientational disorder such that the space group symmetry of the average structure is cubic $Pn\bar{3}m$. Whilst $Zn(CN)_2$ does not exhibit any temperature-dependent phase transitions under atmospheric pressure, $Cd(CN)_2$ undergoes a displacive phase transition at 130 K and a possible orientational-glass transition at 80 K.[218] This phase transition from cubic $Pn\bar{3}m$ to tetragonal $I4_1/amd$ is a result of long-range cyanide ion orientational ordering.

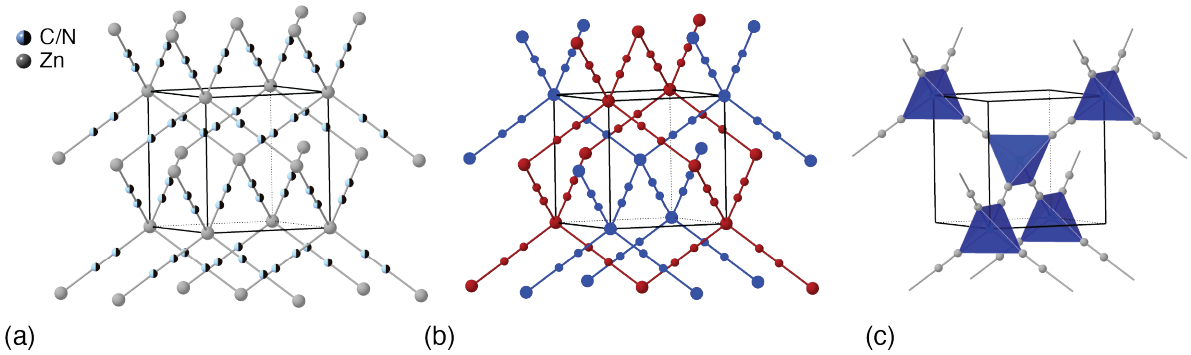

Figure 5.1: Different ways of viewing the structure of $Zn(CN)_2$. (a) The Zn centres are tetrahedrally coordinated to orientationally disordered cyanide ions. (b) $Zn(CN)_2$ is formed by two interpenetrating diamondoid networks (coloured in either red or blue). (c) One of the two networks displayed as a pyrochlore lattice. In $Cd(CN)_2$, there is a preference for the Cd to bind to two C atoms and two N atoms in an an ice-like 'two-in-two-out' manner.

This behaviour has been rationalised *via* a pseudo-spin mapping of the orientation of the cyanide ions onto a spin-ice model.[218] A spin-ice model is applicable since each Cd centre has a preference to bind to two C and two N atoms, respectively (2-in/2-out). This leads to a constant sum rule for each $Cd(C/N)_4$ tetrahedron in the respective pyrochlore lattices (Fig. 5.1 (c)). A quantitative fit to a spin-ice Hamiltonian *via* both DFT and NMR studies allowed Coates and co-workers to reproduce the experimentally observed cyanide ordering and associated temperature of the phase transition.[218] Moreover, the 'spin-ice physics' of $Cd(CN)_2$ is on a similar energy scale to the lattice vibrations (1–2 THz) such that there is significant interplay when approaching the transition temperature. This is not the case for $Zn(CN)_2$ where the energy required for cyanide ion flips is much greater such that cyanide ion ordering is thermally inaccessible.

5.2.2 Negative Thermal Expansion in $Zn(CN)_2$ and $Cd(CN)_2$

Both $Zn(CN)_2$ and $Cd(CN)_2$ exhibit strong isotropic NTE over a large temperature range.[219–222] Their negative volumetric expansion coefficients are more than double that of other well-known NTE materials such as ZrW_2O_8 ($-50\,MK^{-1}$ for $Zn(CN)_2$;

$-60\,\mathrm{MK}^{-1}$ for $Cd(CN)_2$; and $-27\,\mathrm{MK}^{-1}$ for ZrW_2O_8).[223] Whilst the NTE of $Zn(CN)_2$ remains isotropic between 30–300 K, the behaviour of $Cd(CN)_2$ is more complicated; the NTE becomes strongly anisotropic below T_c (130 K). Clearly, there is an interplay between the orientational ordering of the cyanides and the lattice dynamics such that the thermal expansion behaviour of $Cd(CN)_2$ is complex. Additionally, it has been postulated that the formation of anti-polar nanodomains with locally strong anisotropic behaviour may be enhancing isotropic NTE behaviour of $Cd(CN)_2$ when approaching the phase transition.[224] The strong anharmonicity of the phonon modes and their complex interactions with the local CN^- order makes low temperature NTE behaviour of $Cd(CN)_2$ particularly difficult to model. This chapter focuses on $Zn(CN)_2$ and the high temperature $Cd(CN)_2$ structures and seeks to understand why these exhibit particularly large NTE within the quasi-harmonic approximation. Isotropic NTE is of particular fundamental interest because it can signal a variety of anomalous mechanical responses including auxeticity[225] and pressure-induced softening.[45,226] In addition, NTE materials can be employed in the design of composites with tuneable coefficients of thermal expansion.[227–232]

5.2.3 The RUM Picture

The original and local description of NTE in the $M(CN)_2$ family has focussed largely on cooperative rotations of the $M(C/N)_4$ tetrahedra. These rotations have the C and N atoms of each M–CN–M linkage displace away from the local M···M axis, giving rise to a 'skipping-rope' type motion that draws the structure in on itself (Fig. 5.2).[221,233]

Whilst earlier work may have focussed on whether a 'see-saw' vs 'skipping-rope' motion is driving the NTE, a more complete approach assesses the phonon modes responsible over the whole Brillouin zone. Indeed, *ab initio* phonon calculations have

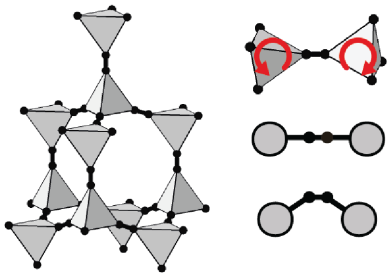

Figure 5.2: RUM rotations of neighbouring coordination polyhedra—as proposed to occur in M(CN)2 frameworks—give rise to local transverse displacements away from the M···M axis and so shorten the M···M distance if bond lengths are preserved.

been carried out for $Zn(CN)_2$ and $Cd(CN)_2$.[222,234–236] As described in the introduction, the extent to which individual modes influence thermal expansion is quantified by the corresponding mode Grüneisen parameters (γ)[15,234–236] which capture the sensitivity of the angular frequency of a mode at each wave-vector to changes in crystal volume. Modes with $\gamma < 0$ soften at lower volumes and favour NTE, whilst modes with $\gamma > 0$ drive PTE behaviour. These are consistent across calculations for $Zn(CN)_2$, that are all very similar, and identify three main NTE branches.

The lowest energy branch at $\omega < 1\,\text{THz}$, for which γ is most negative, is doubly degenerate and has translational character; the higher energy branches at $\omega \sim 2.5\,\text{meV}$ and $\omega \sim 10\,\text{meV}$ are each triply degenerate and correspond to correlated $M(C/N)_4$ rotations.[29,234]

Fig. 5.3 adapted from Ref. 234, shows calculated phonon dispersion curves for $Zn(CN)_2$ (a), and these phonon dispersion curves weighted by their Grüneisen parameter (b) and RUM character (c), respectively. These phonon dispersion curves were calculated using an empirical force field generated by fitting to DFT calculations. The many ways polyhedral rotations can be combined leads to relatively dispersionless NTE bands. The RUMs corresponding to anti-phase nearest-neighbour tetrahedral rotations

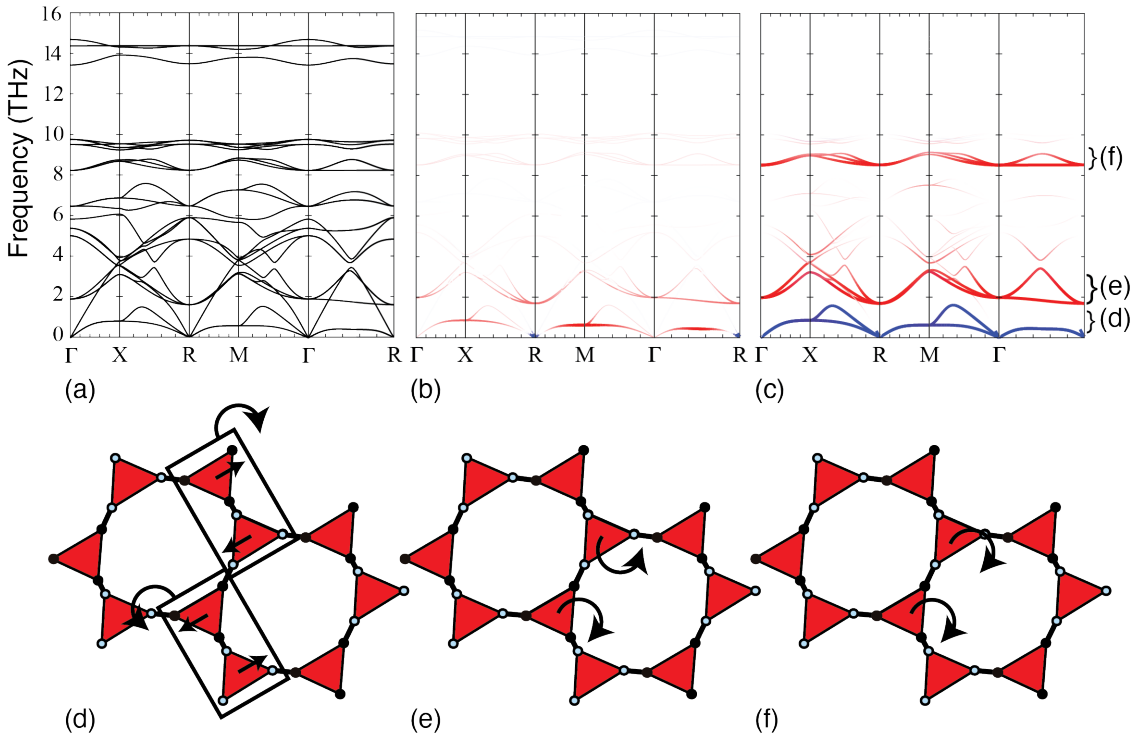

Figure 5.3: Calculated phonon dispersion curves for $Zn(CN)_2$. (a) Phonon dispersion curves for $Zn(CN)_2$ (b) Dispersion curves coloured according to the corresponding value of the mode Grüneisen parameter $\gamma(\nu, \mathbf{k})$. Red is a negative value of $\gamma(\nu, \mathbf{k})$ (down to a minimum of -18); blue is a positive value of $\gamma(\nu, \mathbf{k})$ (up to a maximum of 0); white is a $\gamma(\nu, \mathbf{k})$ value of zero. (c) Dispersion curves coloured according to projection of the eigenvectors onto RUMs. Colour strength corresponds to the degree to which a mode is a RUM; white corresponds to zero RUM-character in a given mode. The colour itself corresponds to the nature of the RUM: red is purely rotational RUM motion; blue is purely translational RUM motion. The corresponding eigenvectors of (d) the translational RUMs (around 0.5 THz), (e) the first rotational RUMs (around 2.0 THz), and (f) the second rotational RUMs (around 9.0 THz), viewed down the $[1\bar{1}0]$ direction with the undistorted structure in grey shown behind. The translational RUMs correspond to lateral translations of the tetrahedra leading to rotations of pairs of tetrahedra. The rotational RUMs correspond to neighboring tetrahedra rotating in the same or opposite direction. Figure adapted and reproduced with permission from Ref. 234.

have relatively large Grüneisen parameters at 2 THz and are important mostly at the R-point. The key NTE modes are clearly the translations, with large Grüneisen parameters over larger regions of reciprocal space. Yet, the RUM model may not adequately explain the complete microscopic origin of these translational modes.[234]

5.2.4 NTE in Diamond Structures

At low temperatures, the ostensibly very different material Si also exhibits NTE.[237] The Si–Si bond network of silicon traces the same diamondoid structure of the $M(CN)_2$ family, but there is of course no possibility of polyhedral rotations. The NTE behaviour of silicon is understood as a geometric effect. The undistorted Si structure is maximally expanded such that any change in its internal angles results in a volumetric contraction. The transverse acoustic branches that capture shear-like distortions of the network must then have a negative Grüneisen parameter and lead to NTE.[238] The NTE behaviour of Si can thus be understood in terms of angular deformation of the Si–Si bond network[239] (Fig. 5.4). This geometric effect can be tuned by varying the relative strengths of the bond-bending and bond-stretching terms.[239] Indeed, for the zinc-blende structure-type, the coefficient of thermal expansion can be directly related to the difference in ionic character between the constituent ions and their relative bond-bending force constants.[240,241]

At certain points in reciprocal space, the Grüneisen parameter can be derived for the transverse acoustic modes for a diamond framework. The formalism of Ref. 239 for diamondoid systems gives a geometric estimate of the Grüneisen parameter at

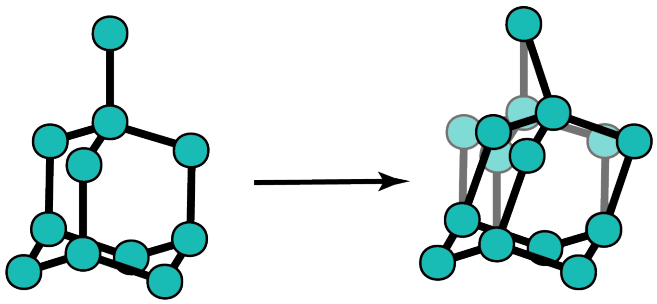

Figure 5.4: Acoustic (shear) modes in C and Si distort network angles but not bond-lengths and accordingly couple to volume reduction accordingly.

the Brillouin zone boundary (X-point):

$$\gamma_{\text{geom}} = \frac{2}{3} - \frac{8}{\sqrt{3}} \frac{B_0 d_0}{m\omega_0^2}. \tag{5.1}$$

Here, B_0 is the bulk modulus, d_0 the inter-node separation, m the node mass, and ω_0 the zone-boundary TA angular frequency (X-point). The last term of Eq. (5.1) can be interpreted as the ratio of restoring forces for compressive (numerator) and angular (denominator) deformations. The value of γ is most large and negative when the latter is very much smaller than the former. Ref. 239 found that their geometric results fitted experimental values well for both C and Si.

This chapter establishes an unexpected mapping between these two seemingly contrasting NTE mechanisms. *Ab initio* DFT calculations re-confirm the low energy translational modes in effecting NTE. Neutron total scattering measurements of $Cd(CN)_2$ then allow the experiment-driven models of local atomic displacements in this material to be derived and so to test the validity of the 'skipping-rope' mechanism illustrated in Fig. 5.2. Instead, it is found that the magnitudes of the M atom displacements are essentially as large as those of the C and N atoms. Hence, there is a natural mapping of each M–CN–M linkage onto a single M$\cdots$M connection with the cyanide ion acting as a pseudo-spring. Projecting the $M(CN)_2$ phonon dispersion onto M atom displacements reveals a hidden spectrum closely related to the phonon dispersion of Si. The translational NTE branches of $M(CN)_2$ have the same character as the NTE shear modes in Si and it is demonstrated that the simple geometric rules used to rationalise the extent of NTE in the latter also apply to $M(CN)_2$. This chapter highlights the conceptual power of abstracting the lattice dynamics of network structures in terms of their underlying 'framework modes'—an approach of potential importance across a wide range of different materials which

I will come to explore further in the next chapter.

5.3 Results

5.3.1 Identifying the NTE Phonon Modes

Ab initio DFT calculations were used to determine the phonon dispersion relations for $Zn(CN)_2$ and $Cd(CN)_2$ using the CASTEP code (Fig. 5.5).[115] The GGA-PBEsol functional and norm-conserving potentials generated from the code ONCVPSP were used.[244] In all cases, electronic energies and forces were converged to within 1×10^{-12} eV and 1×10^{-6} eV Å^{-1}, respectively. A plane-wave[245] cut-off of 1200 eV with the Monkhorst-Pack[174] grids of $7 \times 7 \times 7$ for integration of the electronic states across the Brillouin zone were used. Geometry optimisation was carried out using the BFGS (Broyden-Fletcher-Goldfarb-Shanno) algorithm[135] at 0 GPa. The space group symmetry, cubic $P\bar{4}3m$, corresponding to ordered CN^- orientations was used rather than the orientationally disordered cubic space group $Pn\bar{3}m$. Previous comparison between these models have found no significant difference for both the phonon modes and the NTE.[222,234]

Phonon frequencies were then calculated using DFPT[246] with MP grids of $4 \times 4 \times 4$. These were offset to capture the Γ-point. Fourier interpolation was used to calculate the phonons along the required paths using a spacing of 0.01 Å^{-1}. The Grüneisen (γ) parameters of modes were obtained by calculating phonon frequencies at two strained cell volumes of ±1 % and ion positions were re-optimised before computing phonon frequencies. *Euphonic* was used to read-in and re-order phonon frequencies and eigenvectors from the CASTEP output files.[126,127]

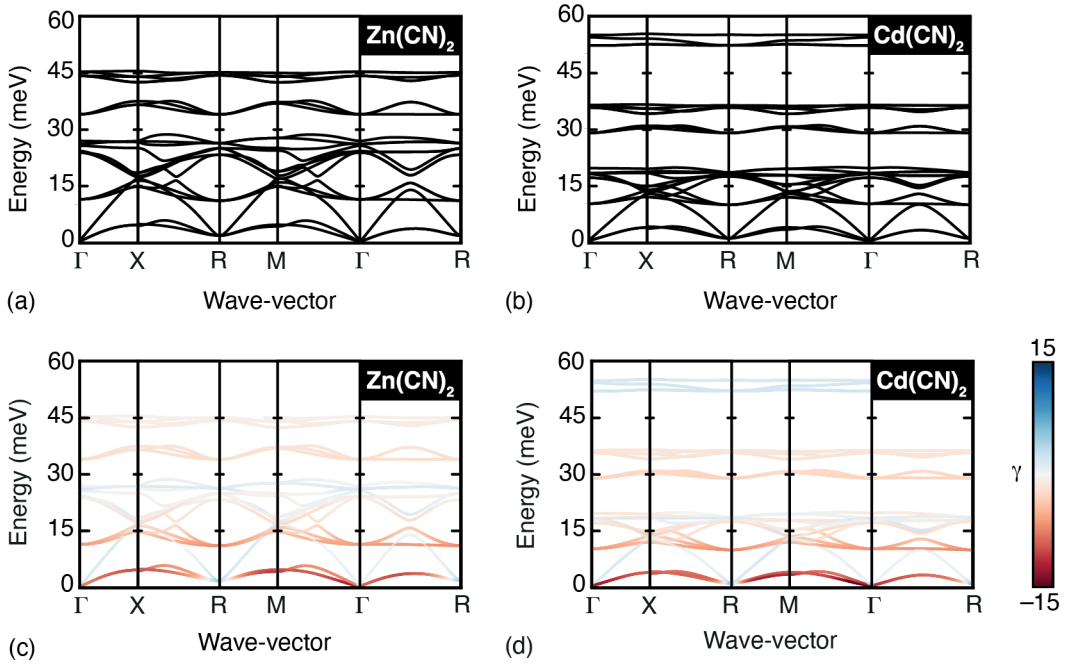

Figure 5.5: Four sets of $M(CN)_2$ dispersion curves calculated using DFT. For (a) and (b), these are the dispersion curves for $Zn(CN)_2$ and $Cd(CN)_2$ in the conventional representation; note that the cyanide stretching bands occur at very high energies and are omitted here. For (c) and (d), the same dispersion curves are coloured according to the corresponding value of the mode Grüneisen parameter. The colour map used ranges from red ($\gamma = -15$) to blue ($\gamma = +15$), with white indicating a value of zero. The transverse acoustic modes are the branches with the most negative γ (i.e., deepest red colour), and hence dominate the low temperature NTE behaviour for both $Zn(CN)_2$ and $Cd(CN)_2$.

Our results are in close agreement with previous DFT calculations performed on these systems (Fig. 5.5).[15,222,234–236] The energy scale ranges from 0–60 meV such that the cyanide stretches that occur around 260 meV are not shown. $Cd(CN)_2$ has a lower energy manifold due to the larger mass of Cd relative to Zn.[222] As seen in previous studies, the low energies and large negative Grüneisen parameters of the translational branches indicate that these modes dominate the NTE behaviour, especially at low temperatures for $Zn(CN)_2$. The acoustic modes at the R-point correspond to anti-phase translations of the interpenetrating frameworks and are closely related to the inter-framework dispersion interactions.

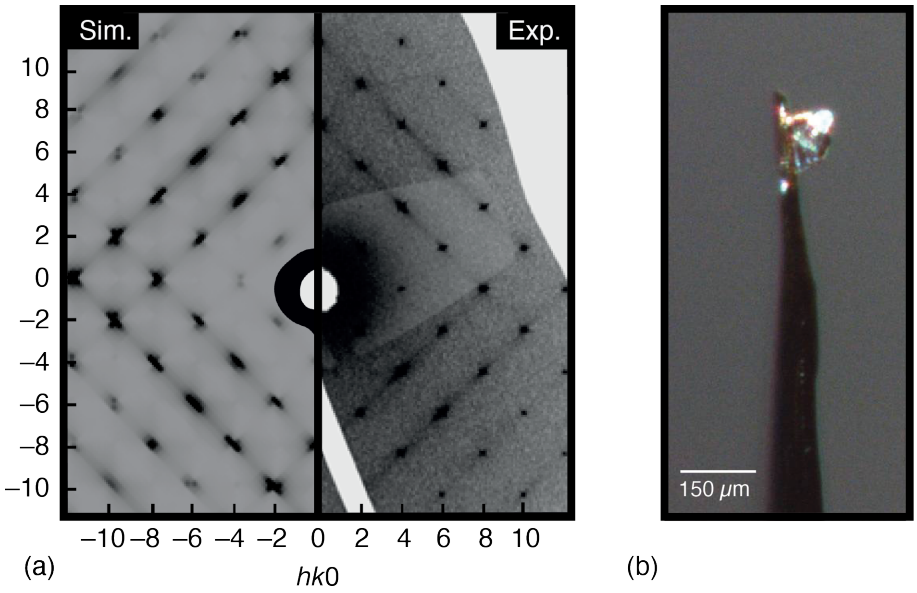

Figure 5.6: (a) Single crystal TDS measurements of the $hk0$ plane for $Zn(CN)_2$. (b) The data crystal used to acquire TDS for $Zn(CN)_2$.

As previously seen for the cyanospinels and DBP, TDS is a good probe for the low energy dynamics of the systems of interest. Single crystals of $Zn(CN)_2$ were prepared and measured at 300 K using mirror-monochroamted Mo-K_α radiation ($\lambda = 0.7107$ Å) with the in-house Rigaku XtaLAB Synergy-S Dualflex diffractometer. The synthesis was as follows: $K_2Zn(CN)_4$ (56 mg, 0.217 mmol) and $Zn(NO_3)_2.6H_2O$ (50 mg, 0.264 mmol) were dissolved in a minimal amount of distilled water. These were then placed at opposing ends of an H-tube which was then filled with distilled water. After two weeks, colourless octahedral crystals of $Zn(CN)_2$ of approximate size of 150 μm were formed. The TDS was then qualitatively compared to that calculated from the phonon dispersion curves using the *ab2tds* program (Fig. 5.6).

The main feature of the experimental measurements is the presence of streaks of TDS intensity along the $\langle 110 \rangle$ directions. These correspond to the low-energy TA acoustic modes along the $\Gamma \rightarrow$ M path in reciprocal space. The good match achieved by the simulation shows how the phonon dispersion calculations capture well lowest

energy phonon modes for $Zn(CN)_2$ at 300 K.

5.3.2 Local distortions from Experiment

To test the validity of the NTE mechanism, a real-space interpretation of vibrational motion in the $M(CN)_2$ materials is needed. A combination of neutron total scattering measurements from Ref. 218 and a reverse Monte Carlo (RMC) refinement over a range of $0.5 < Q < 50$ Å^{-1} is undertaken. The structures of $Zn(CN)_2$ and $Cd(CN)_2$ (pair of interpenetrated diamondoid frameworks with $Pn\bar{3}m$ symmetry) enforce identical distances between M$\cdots$M or C/N$\cdots$C/N pairs both within and between the networks. It is therefore particularly difficult to directly interpret local structure measures such as the PDF since contributions from thermal motion within a single framework are superposed with displacements of the frameworks themselves relative to each other. RMC is well placed to disentangle these two contributions as it fits the PDF using an atomistic representation that is interpretable as a structural snapshot of the system undergoing thermal motion.

Experimental neutron scattering data for isotopically-enriched $^{114}Cd(CN)_2$,[218,247] acquired at 300 K using the POLARIS instrument at ISIS,[248] are shown in both real and reciprocal space representations in Fig. 5.7 (a)–(c). The Bragg intensities place a constraint on the average extent of vibrational motion through the Debye–Waller factors (single-particle correlation functions), and the PDF adds information regarding correlated displacements *via* its sensitivity to two-body correlations.[249–251] RMC refinements against these data made use of the RMCProfile code,[252] and were carried out using $8\times8\times8$ supercells of the $Pn\bar{3}m$ $Cd(CN)_2$ structure, with cyanide ion orientations determined according to the structural spin-ice model presented in Ref. 218.

RMC refinements were then carried out with equal weights assigned to three data sets: the total PDF, the total-scattering structure factor, and the Bragg structure factor (Fig. 5.7 (a)–(b)). To obtain satisfactory fits to the data, the neutron scattering length of ^{114}Cd had to be adjusted by an empirical factor of 0.7. This is attributed to incomplete ^{114}Cd isotopic substitution. Indeed, ^{113}Cd has a negative coherent scattering length and a very high absorbance compared to ^{114}Cd, so even a small contaminating quantity has a relatively large impact on the average Cd neutron scattering length.

Informed by the C–N and Cd–C/N peaks in the total PDF, the C–N nearest-neighbour distances were constrained to be between $0.99 \leq d(\mathrm{C-N}) \leq 1.4\,\text{Å}$, whilst the Cd–C/N nearest-neighbour distances were constrained to be $1.95 \leq d(\mathrm{Cd-C/N}) \leq 2.4\,\text{Å}$. Sample configurations were taken every 10^6 accepted moves to ensure that the system had equilibrated and was uncorrelated.

With access to an atomistic representation of the vibrational motion in $Cd(CN)_2$, one can extract the degree of local vibrational motion across individual Cd–C–N–Cd linkages from the RMC configurations. For each such linkage, the local Cd$\cdots$Cd axis was identified as expected from the high symmetry average structure. A suitable geometric transformation was then applied to bring each such axis into coincidence, such that the displacements of all Cd–C–N–Cd linkages can be projected onto a single collective distribution. The distribution so obtained is represented in Fig. 5.7 (d). If local vibrational motion were dominated by the skipping-rope mechfanisms as described in Refs. 220,221,234, there should be a greater distinction between the transverse displacements of the C/N atoms and the isotropic displacements of the anchoring Cd atoms than is evident in the RMC refinements. Instead, the magnitude of Cd, C, and N displacements in this local reference frame is roughly isotropic and surprisingly

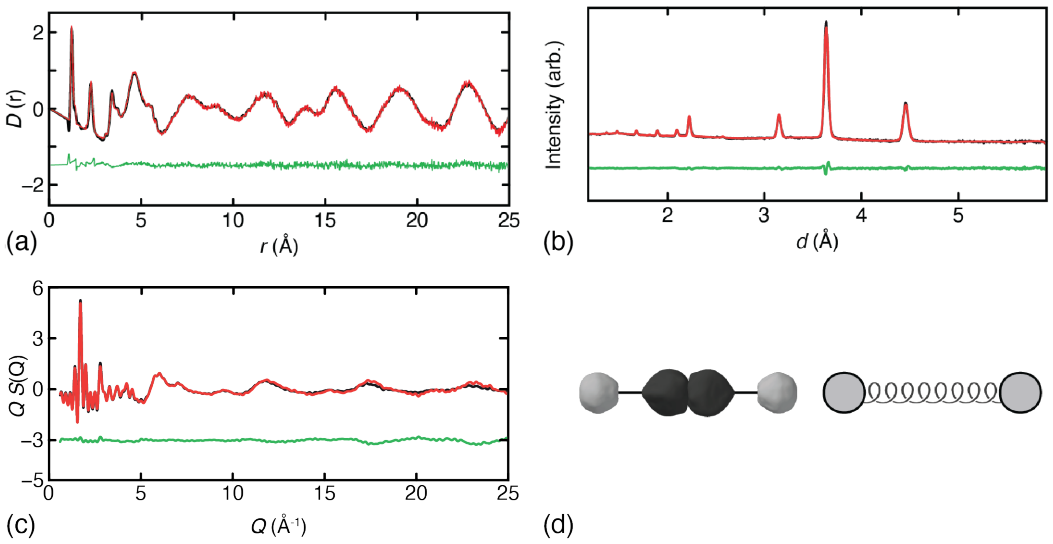

Figure 5.7: Experimental neutron total scattering data for $Cd(CN)_2$ at 300 K and corresponding RMC fit. (a) The neutron PDF, with data shown in black, RMC fit in red, and difference function (fit − data) shown in green. (b) Reciprocal space scattering function shown here as a conventional Bragg diffraction pattern, with line colours as in (a). (c) $Q\,S(Q)$ of $Cd(CN)_2$ at 300 K (black line) and the corresponding RMC fit (red line) and difference function (green line, offset by −2 units). $Q\,S(Q)$ was not used for the RMC refinement. (d) Projection of the atomic positions within Cd–C/N–C/N–Cd linkages onto a single common coordinate system. The symmetrised distributions of projected atoms (left) are shown as 90% isosurfaces and reflect the degree of local thermal displacements of Cd (grey), and C and N atoms (black), deconvolved of contributions from inter-framework slipping.[218] That all atom types show similar thermal distributions suggests that the CN linkages behave as pseudo-springs connecting neighbouring Cd atoms (right).

similar from one atom type to another. Hence the picture developed in Fig. 5.2 (and elsewhere)—as appealing as it is—does not accurately capture the key microscopic behaviour of $M(CN)_2$. The distribution of Fig. 5.7 (d) suggests that the dominant vibrational motion might be better understood in terms of collective displacements of the entire M–CN–M linkages. The interpretation is not that this linkage is rigid (e.g., as in the 'rigid-rod' model for NTE in Cu_2O),[253] but rather that the degrees of freedom of the C and N atoms can be integrated out such that the cyanide ion behaves as if it were a pseudo-spring acting between connected M atom nodes.

5.3.3 Framework Modes

To test this interpretation, the calculated $M(CN)_2$ phonon dispersion curves were projected onto the contribution from the M atom displacements alone, using a normalised weighting $0 \leq \rho(j, \mathbf{q}) \leq 1$ that quantifies the magnitude of M atom displacements for each phonon mode with label j and wave-vector $\mathbf{q}$. The relevant weighting $\rho(j, \mathbf{q})$ was defined as follows:

$$\rho(j, \mathbf{q}) = \sum_i |\mathbf{e}(i, j, \mathbf{q})|^2. \tag{5.2}$$

Here, the summation is over i, the atomic indices for the nodes. In practice, for $Zn(CN)_2$ and $Cd(CN)_2$, this involves summing over the two Zn or Cd 'nodes'. Since the eigenvector $e(j, \mathbf{q})$ is normalised, then $\rho(j, \mathbf{q})$ is always bound between 0 and 1. A value of 0 indicates a mode with no M atomic displacements, whilst a value of 1 would indicate that the mode is described purely by M displacements.

The displacement-weighted phonon dispersion curves for $Zn(CN)_2$ and $Cd(CN)_2$ are shown in Fig. 5.8; the coarse-grained vibrational modes these characterise are referred to here as the 'framework modes' of the system. Importantly, the key low energy NTE branch of both $Zn(CN)_2$ and $Cd(CN)_2$ is preserved in this mapping. Hence, the dominant NTE mechanism should be understandable in terms of the behaviour of the diamondoid framework itself, independent of the cyanide-ion displacements (i.e., neglecting correlated polyhedral tilts or 'skipping-rope' motion altogether).

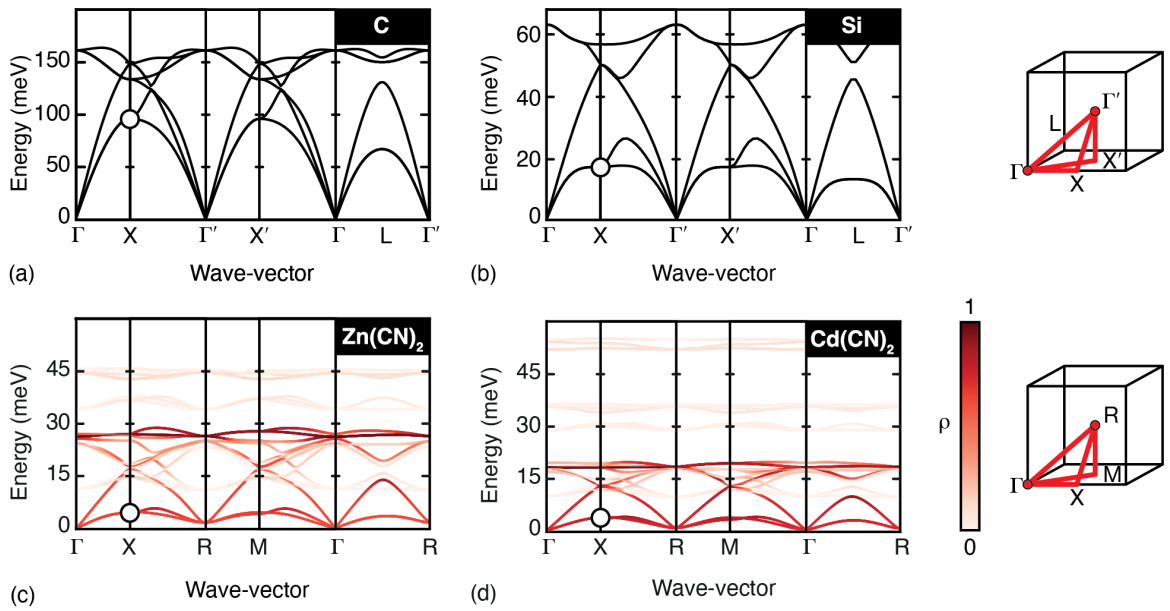

Figure 5.8: Phonon dispersions of diamond and silicon compared to the framework-weighted phonon dispersion curves of $Zn(CN)_2$ and $Cd(CN)_2$. The diamond (a) and silicon (b) phonon dispersion curves are plotted along a similar path of reciprocal space to that of the $M(CN)_2$ systems. For $Zn(CN)_2$ (c) and $Cd(CN)_2$ (d), each mode is coloured according to the relative displacements of the M atoms, capturing the framework modes of $M(CN)_2$. Note the similar form amongst the four sets of dispersion curves. The zone-boundary TA modes discussed in the text are highlighted using open circles. These modes involve angular deformations of the diamondoid lattice as shown in Fig. 5.4.

5.3.4 The Diamond Structure is Key

The framework mode dispersion relations of $M(CN)_2$ are closely related to those of diamond and silicon (Fig. 5.8 (a)–(b)), albeit that the presence of the two interpenetrating frameworks in $M(CN)_2$ changes the symmetry of reciprocal space between the two families. The overall energy scale of the dispersion is understandably much lower in the case of the cyanide frameworks: it is quite intuitive that M···M linkages would be much softer than C–C or Si–Si bonds. But the form of the dispersion also varies in the *relative* energy of the TA branches with respect to the optic branches. It is the TA branches that correspond to the NTE shear modes of the diamond structure (Fig. 5.4), and their zone-boundary energies provide a measure of the angular rigidity of the network.

Indeed, the previously described formalism of Ref. 239 for diamondoid systems on $Zn(CN)_2$ and $Cd(CN)_2$ can be used here (see Eq. (5.1)). Table 5.1 lists the various terms in Eq. (5.1) for each of C, Si, $Zn(CN)_2$, and $Cd(CN)_2$, together with the calculated values of γ_{geom}. Excellent agreement is found with the DFT Grüneisen parameters. Hence, the contribution of the transverse acoustic branches to NTE can be understood essentially entirely in terms of the geometric effect illustrated in Fig. 5.4. In particular, there is no need to invoke mechanisms of polyhedral rotations or transverse vibrational motion of the C and N atoms other than through their role in allowing the M–CN–M linkage to behave as if a pseudo-spring.

As observed in previous studies, the DFT-obtained values for the bulk moduli and zone-boundary TA frequencies of $M(CN)_2$ frameworks are overestimated with respect to experiment.[222,255] Hence, one should not attach too great an importance to the numerical values of γ_{geom}, except to note that they are internally consistent and are much larger in magnitude for $M(CN)_2$ than for C or Si as a result of the

Table 5.1: Parameters used in the geometric estimation of NTE mode Grüneisen parameters (Eq. (5.1)) and comparison with DFT results.

	C	Si	$Zn(CN)_2$	$Cd(CN)_2$
B_0 / GPa	442	98.7	36.9	33.2
d_0 / Å	1.54	2.35	5.12	5.46
m / $g\,mol^{-1}$	12.0	28.1	117	164
ω_0 / THz	146	25.6	6.79	5.47
$\gamma_{geom}(X)$	−0.08	−2.8	−9.0	−9.6
$\gamma_{DFT}(X)$	0.20	−1.9	−9.9	−9.2

relative stretching and angular deformation energies noted above. In fact, working within the formalism of Eq. (5.1), the experimental values of B_0 (33.4 GPa[45] and 13.6 GPa[256]) and ω_0 (3.7 THz[254] and 1.9 THz) for $Zn(CN)_2$ and $Cd(CN)_2$, respectively, predict an even more extreme $\gamma_{geom} \simeq -30$. These large and negative Grüneisen parameters for zone-boundary TA modes are consistent with the observation of dynamic instabilities under relatively modest pressures; while the high pressure structure of $Cd(CN)_2$ is not known,[256] that of $Zn(CN)_2$ involves framework shear of the kind shown schematically in Fig. 5.4.[257]

Whilst the underlying diamond frameworks of $M(CN)_2$ are key in driving their NTE mechanism, many solids with diamondoid frameworks such as Si exhibit NTE-PTE transitions. When temperature is increased, higher energy modes with positive Grüneisen parameters, become thermally accessible and affect the thermal expansion coefficient, eventually leading to PTE. For Si, this transition occurs around 120 K, since the 'framework modes' are of relatively high energy with small negative Grüneisen parameters (of comparable magnitude to the other modes). In contrast, for $M(CN)_2$, the large magnitude in the negative Grüneisen parameter and the low energies of their TA modes ensures that the NTE is large and persists over a large temperature range. In addition, the higher energy rotational modes with negative Grüneisen parameters

(albeit of a smaller magnitude), help counteract the population of positive Grüneisen modes. It should also be noted that the formalism of Ref. 239 is only applicable to diamondoid systems. Below 130 K, the phase transition of $Cd(CN)_2$ that is due to CN^- ordering[218] removes the symmetry constraints within the diamond framework and thus the geometric necessity for negative Grüneisen transverse modes.

5.4 Outlook

The key result of this study is to clarify the most appropriate conceptual framework within which to understand the dominant lattice dynamics of $M(CN)_2$ NTE materials. In conventional framework materials—e.g., silicates, zeolites, and perovskites—the RUM model usually plays this role.[26–28,258] But, while cyanides and other molecular frameworks certainly support RUMs[29]—and indeed the TA branches can be couched in terms of translational RUMs[234]—the more relevant coarse-graining appears to be simply in terms of the underlying framework connectivity. The term 'framework modes' is used to denote the coarse-grained lattice dynamics of the framework itself—i.e., nodes connected *via* pseudo-springs to give an appropriate degree of compressive and angular rigidity. In the diamondoid $M(CN)_2$ structures, these modes include the low energy branches that dominate NTE. But equivalent modes may be relevant to the low energy dynamics of other extended network structures, such as MOFs, for which the conventional RUM picture appears to break down.[48] Common to both approaches is the motivation to simplify the lattice dynamics of otherwise complex materials and to identify the key structural features responsible for phenomena of physical interest. In this spirit, the 'framework mode' approach also serves to identify the possible design principles one might use to optimise NTE in diamondoid networks: the key microscopic feature being to combine compressive rigidity with angular flexibility.[276]

6

Phonon Modes for Framework Materials: a Generalised Approach

6.1 Introduction and Acknowledgements

This chapter extends the 'framework-modes' picture developed previously for $M(CN)_2$ and applies it generally to framework materials. This coarse-grained approach is seen as a complementary model to the RUM model and is applicable to structures with strong directionality in their bonding where the structural polyhedra present may no longer be edge- or corner-sharing. For framework materials, the low-energy modes tend to be associated with parallel motions of atoms, both in the nodes and linkers. This new coarse-graining approach aims to capture these low-energy 'framework modes' and relate them to thermal and mechanical properties of the system of interest. This method, that only requires a structure as an input, also allows for a straightforward approach in approximating TDS and for its interpretation in terms of whole-framework breathing and flexing modes. Its effectiveness is then discussed for several case studies, namely: MOF-5 and its TDS, the mechanical flexibility of $NH_4Zn(HCOO)_3$, and the thermal expansion behaviour of $Zn(CN)_2$.

Dr Thomas C. Nicholas helped throughout this project: both for the coarse-graining method that uses his CHIC python module and the automation of the method. Dr Johnathan M. Bulled contributed to the development of the conceptual framework. The MOF-5 experimental diffuse scattering was measured by Dr Emily G. Meekel on her crystals.

6.2 Background

6.2.1 The RUM Model Applied to Framework Materials

The successes of the RUM model have been described extensively in this thesis. The RUM model has helped further our understanding of the microscopic origin of temperature-dependent phenomena such as phase transitions, network flexibility and NTE.[26,37] A key tenet of the RUM model is that energy cost of distorting the structural polyhedra remain is much greater than flexing at the polyhedral connections. Therefore, this approach works well for materials that can be described as edge-sharing or corner-sharing polyhedra (perovskites, silicates, and even cyanides where the cyanide ion is treated as a rigid rod). Yet, this picture can break down for framework materials where there is an increase in the distance between the polyhedra and where the bonding may have directionality.[258] Here, with extended linkers and increased connectivity, the 'shared' vertices between the polyhedra become less well-defined. This added complexity makes RUM analysis much more difficult. Indeed, for framework materials such as zeolitic imidazolate frameworks (ZIFs), there is no clear preferred way of defining the rigidity and degrees of freedom of the imidazolate linker (Fig. 6.1). Previous RUM analysis for MOF-5 had to examine several different rigid units to coarse-grain both the nodes and linkers since the choice was not immediately obvious. Furthermore, some of the low-energy phonons associated with NTE seemed to involve polyhedral distortions that were inconsistent with the RUM model.[48] Ideally, a well-adapted coarse-graining method would require minimal user input.

Of course, the RUM model was originally developed with soft-mode phase transitions of silicate materials in mind. It is classically ill-adapted to handle structures containing extended and organic linkers such as MOFs, with all their chemical modularity and

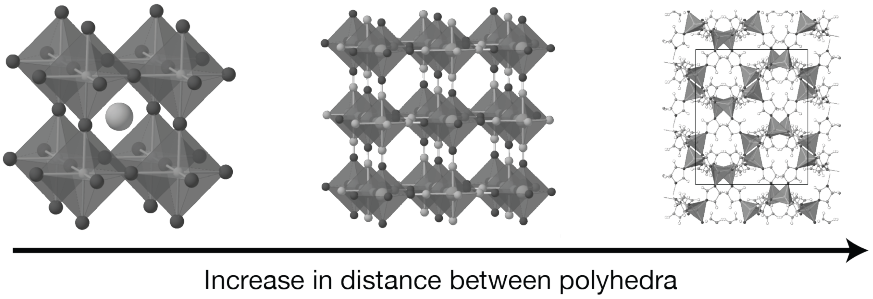

Figure 6.1: The RUM model was originally conceived for edge and corner-sharing polyhedra. When the distance between polyhedra is small, as for perovskites, the RUM model works well. For cyanometallates, such as Prussian blues, the cyanide linker can be treated as a rigid rod and RUM analysis remains general. As the distance between polyhedra is increased, as for ZIF-4, the RUM picture becomes more arbitrary in the choice and flexibility of the rigid units.

tuneability that emerged a few years after the first RUM models.

Whilst there have been many studies focussing on the synthesis of new MOFs, and exploring their responsiveness towards chemical substitution or behaviour under different stimuli, there have been comparatively fewer studies performed to understand their lattice dynamics. The inherently larger number of atoms in these systems has traditionally made phonon calculations particularly expensive computationally and difficult to interpret. Yet, at 300 K, the dynamics are of particular importance, especially for a class of materials where local breathing and flexing modes are often considered key factors in determining their ability to sequester small molecules. Understanding these effects is therefore important in realising the value of MOFs to be used in gas storage and separations applications.

MOF-5, $[OZn_4][1,4\text{-bdc}]_3$ (1,4-bdc = 1,4-benzenedicarboxylate) is considered to be the canonical MOF and also exhibits NTE, with an associated large volumetric coefficient of $\alpha_v = -48\,\mathrm{MK}^{-1}$.[259,260] As a result, its dynamics have been extensively studied and its *ab initio* phonon dispersion curves have been calculated previously.[48,259,261]

The driving force for the NTE of MOF-5 had originally been assigned to a trampoline mode where the benzene ring of the BDC linker translates out of the plane.[259,261] RUM analysis was carried out to further rationalise the isotropic contraction of MOF-5 with temperature. As described in Ref. 48, several choices of possible rigid units were used and compared with the full Grüneisen-weighted phonon dispersion curves. There were two possible rigid units for the Zn_4O_{13} node: either a single rigid cluster or four ZnO_4 tetrahedra connected *via* one O atom with full rotational flexibility. For the BDC linker, three possible rigid units were used (BDC as a single rectangle, two edge-sharing rectangles, and a bow-tie arrangement). The sweet spot in terms of fewest degrees of freedom and maximum insight was a combination of single rigid clusters (Zn_4O_{13}) together with the edge-sharing rectangles for the BDC linkers. The modes with the largest contribution to NTE were low-energy acoustic modes in the $\Gamma-X-W$ direction and a low-energy optic mode which corresponded to the trampoline mode described in previous studies. The use of rigid edge-sharing rectangles to coarse-grain the linkers was key in capturing the trampoline-mode as a RUM. Yet, whilst the acoustic modes in the $\Gamma-X$ had RUM-like character, this was not the case in the $X-W$ region. In this region, the phonon mode eigenvectors lead to rigid unit distortions for both the linkers and Zn_4O_{13} nodes. Another coarse-grained approach is required to describe these modes that are not captured by the RUM model. The approach described in this chapter is similar to the 'framework modes' picture developed for the low-energy acoustic modes of $Zn(CN)_2$ in the previous chapter.

6.2.2 Low-Energy Modes in Framework Materials

For framework materials, the low-energy modes have often been associated with parallel motions of the atoms with no distinction as to whether they are part of a linker

or a node. These low-energy modes are present in MOFs,[48] molecular systems,[262] and inorganic solids.[45,263] For MOFs, recent work has shown how topology often dictates the atomic motions for these low-energy modes.[264] For certain isoreticular MOFs, the energies of the low-frequency modes may differ substantially, yet the corresponding mode eigenvectors remain highly similar. This phenomenon highlights the dominant role of network topology in determining the low-energy dynamics of framework systems, a principle previously illustrated in Chapter 5 by the analogy between the phonon dispersion curves of $Zn(CN)_2$ and Si. Capturing the equivalent 'framework modes' for framework materials in a general and automated method is therefore important and would complement well the RUM model.

6.3 Results

6.3.1 Capturing the 'Framework Modes'

Our approach to capture the 'framework modes' is conceptually simple. For a given framework structure, the linkers are replaced with harmonic springs of fixed stiffness (k_{stretch}) whilst the nodes are replaced by a single atom at their centre. There is a small energy penalty assigned to framework hingeing that is fixed by k_{bend} (Fig. 6.2). Our 'framework modes' therefore capture the stretching and shearing modes of the overall framework. This approach is general and only requires the structure of a material, k_{stretch} and k_{bend} parameters as inputs.

In the previous chapter, 'framework modes' were calculated for $Zn(CN)_2$. The Zn atom (or framework node) displacements were projected onto the DFT-calculated phonon dispersion curves to give Zn-displacement-weighted phonon dispersion curves. These coarse-grained dispersion curves had similar shapes to those of Si and C albeit

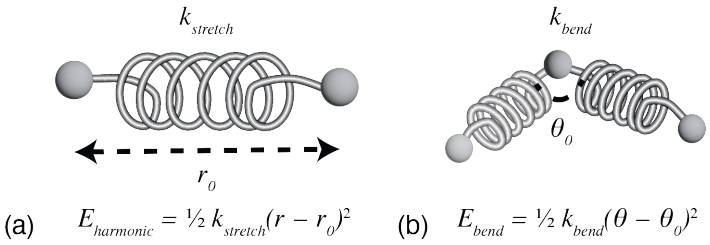

Figure 6.2: The two harmonic potential terms used for the coarse-grained framework potential. (a) The harmonic stretching term. E_{harmonic} is governed by the k_{stretch} force constant. r_0 is the equilibrium bond length given by the initial structure. (b) The angle bending term. This is harmonic in angle with k_{bend} as the force constant. θ_0 is the equilibrium bond angle given by the initial structure.

at a different energy scale. Here, for this 'framework modes' approach, one cannot use *ab initio* phonon calculations since these are intractable for most framework materials with their large number of atoms. This 'framework modes' approach provides an attractive and fast alternative in calculating the key phonon modes for these systems.

Given a framework structure, the first task is to coarse-grain it and create a simple toy-model that preserves the original topology. An interatomic potential that follows the network connectivity is then defined using the k_{stretch} and k_{bend} parameters. From this interatomic potential, phonon dispersion curves can be calculated such that the 'framework modes' are captured.

This coarse-graining is achieved using the CHIC Python module.[265,266] The chemical elements that compose the nodes and linkers can be defined by the user. The automatic procedure generally assumes that heavier elements are node constituents and the lighter ones form the linkers. From this, one has a framework interatomic potential entirely defined by a harmonic spring network. From this potential, one can derive a dynamical matrix, phonon dispersion curves, and the associated thermal properties for the system of interest. TDS can also be calculated from these coarse-grained phonon modes and

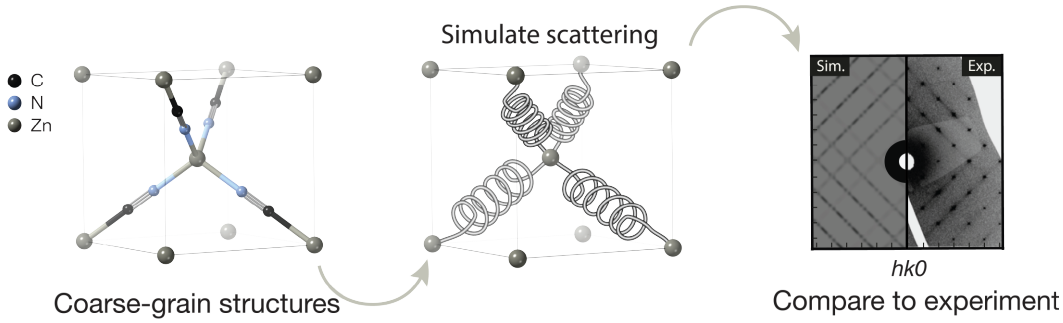

Figure 6.3: An overview of the general methodology for 'framework mode' analysis using $Zn(CN)_2$ as an example. First, the initial structure is coarse-grained, with the nodes replaced by central atoms and the linkers replaced by springs. These are harmonic in distance and harmonic in angle with respect to their flexing. From this simplified potential, the TDS can be simulated as a check of the low-energy dynamics of the framework material.

compared to experiment. This methodology is shown in Fig. 6.3 for $Zn(CN)_2$.

The CN^- ligands are replaced with springs while the Zn nodes remain unchanged. Usually, both the k_{stretch} and k_{bend} parameters are optimised to match previously calculated DFT-derived elastic constants such as the bulk modulus. For $Zn(CN)_2$, the bulk modulus is independent of the k_{bend} term. Only the k_{stretch} parameter was optimised to match the DFT-derived bulk modulus (Table. 6.1—B_0^{cg} is the bulk modulus given by the coarse-grained spring model, and B_0^{DFT} is the DFT bulk modulus) whilst the k_{bend} parameter was optimised to best fit phonon frequencies. Once a spring model is well-fitted, the TDS can be simulated and compared to experiment. A relatively good match indicates that the low-energy dynamics of $Zn(CN)_2$ are well-captured by the 'framework mode' analysis.

Table 6.1: Coarse-grained parameters for $ZnCN_2$

k_{harm} (eV Å^{-2})	k_{bend} (eVrad^{-2})	B_0^{cg} (GPa)	B_0^{DFT} (GPa)
1.75	2.72	36.8	36.9

A direct comparison with the phonon dispersion curves for $Zn(CN)_2$ is perhaps most instructive to truly see what is happening. In Fig. 6.4, the full *ab initio* DFT

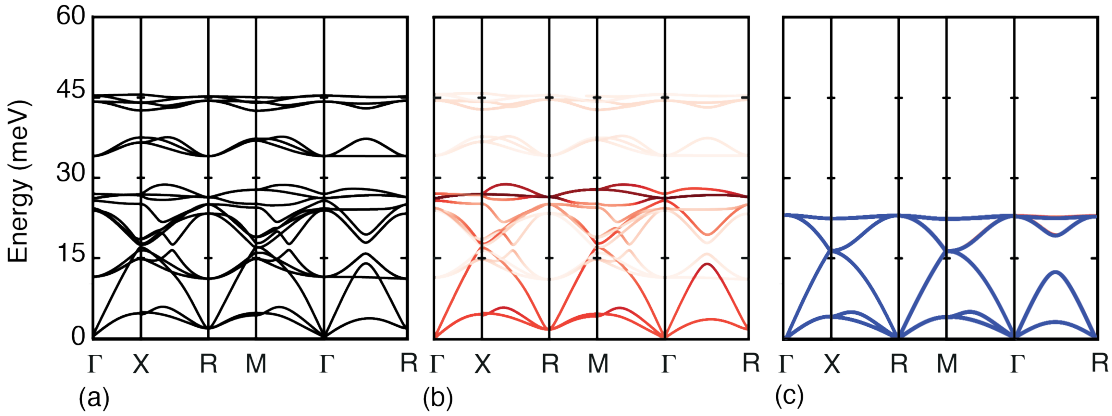

Figure 6.4: The full (a) and Zn-displacement-weighted (b) phonon dispersion curves for $Zn(CN)_2$ compared to the coarse-grained equivalent (c). Note how the coarse-grained potential now only has six modes, compared to the 30 modes in the original. Moreover, the form is similar between the Zn-displacement-weighted and the coarse-grained potential. The difference in energy at the R-point is due to the lack of an intra-framework dispersion interaction in the coarse-grained potential.

phonon dispersion curves are compared with the DFT-derived 'framework modes', and the coarse-grained dispersion curves.

The coarse-grained and DFT-derived 'framework modes' are remarkably similar. The shape is defined by the diamond topology, whilst the match in energy scale indicates that the k_{stretch} and k_{bend} parameters have been well optimised. This conclusion is supported by the direct relationship between long-wavelength acoustic phonons and the crystal elastic constants. Consequently, successful matching of the bulk modulus provides strong evidence that the model accurately captures the stiffness of the framework and, by extension, the energy scale of the 'framework mode' phonons. In fact, the previous formalism and discussion of the last chapter has been condensed to its simplest form: the low-energy phonon properties of complex materials are often governed by k_{stretch} and k_{bend} that are directly related to the stretching and bending of the framework topology.

A benefit of this method is that it can be automated and generalised. Once coarse-graining has occurred (recognising the nodes and linkers based on chemical identification or user input), a small custom code creates a GULP[13] input file, replacing the centroid of the node with a single atom and the linkers with harmonic springs. Phonon dispersion curves and Grüneisen parameters can be quickly calculated *via* GULP. A LAMMPS input file is also outputted with the same interatomic potential. *NPT* MD simulations can then be run with supercells of the coarse-grained system. These MD simulations can be set at a specified temperature (default is 5 K) and allowed to equilibrate (default is to run for 10 ps with a timestep of 1 fs, a T_{damp} of 10 fs, and a P_{damp} of 100 fs). Several configurations can then be taken from the MD run and the TDS calculated using *Scatty*[121] by averaging the diffuse scattering over the different configurations. All experimental diffuse scattering in this chapter was acquired using Rigaku XtaLAB Synergy-S Dualflex diffractometer outputting confocal mirror-monochromated Mo-K_α radiation ($\lambda = 0.7107$ Å).

This chapter explores this coarse-graining methodology with three case studies: TDS using MOF-5, mechanical flexibility with $NH_4Zn(HCOO)_3$, and NTE behaviour with $Zn(CN)_2$.

6.3.2 TDS with MOF-5

The complexity of performing phonon calculations for MOF-5 arises due to the large number of atoms in its unit cell. Its cubic topology, lack of vacancies, and straight-chain linker make it a good case study.[267] Its diffuse scattering should be described entirely by its low-energy phonon modes since there is no correlated short-range disorder. MOF-5 is therefore an excellent test case for the 'framework mode' coarse-grained model. The proposed coarse-graining is straightforward: the Zn_4O nodes are replaced by placeholder

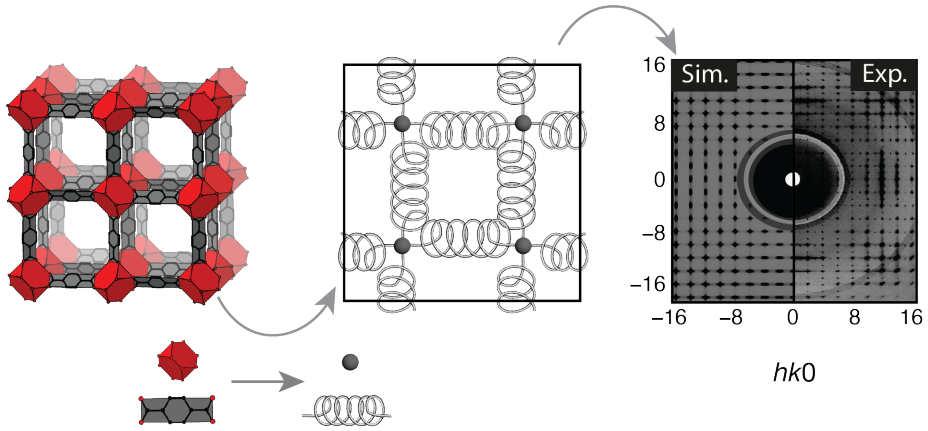

Figure 6.5: The 'framework modes' methodology applied to MOF-5. The Zn_4O nodes are replaced by a placeholder atom, and the 1,4-BDC linkers by the harmonic springs. The new coarse-grained unit cell and potential retains the original cubic topology.[267,268] TDS is then simulated and compared to experiment for the $hk0$ plane. The shape matches relatively well, but the modulation in intensity is not captured.

atoms at their centre, whilst the 1,4-BDC linkers are replaced by springs (Fig. 6.5).

The k_{harm} and k_{bend} used were from Ref. 269 that had optimised them to fit the elastic constants of MOF-5 (Table. 6.2).

Table 6.2: Coarse-grained parameters for MOF-5

k_{harm} (eVÅ^{-2})	k_{bend} (eVrad^{-2})	B_0^{cg} (GPa)	B_0^{exp} (GPa)
1.75	2.72	7.23	15–35

Although a good match to elastic constants is preferable, the strict values of k_{harm} and k_{bend} themselves are relatively unimportant in matching the shape of the diffuse scattering as long as it remains easier to bend around the harmonic spring than to stretch. The relative magnitudes of the k_{harm} and k_{bend} would only affect the intensity since the atomic displacements (and therefore shape of the TDS) are defined by the topology of the structure. For the experimental diffuse scattering, the TDS intensity is dominated by streaks along the $\langle 100 \rangle$ directions, indicative of low-energy TA modes along the $\Gamma \rightarrow \text{X}$ path in reciprocal space. The simulated diffuse scattering matches

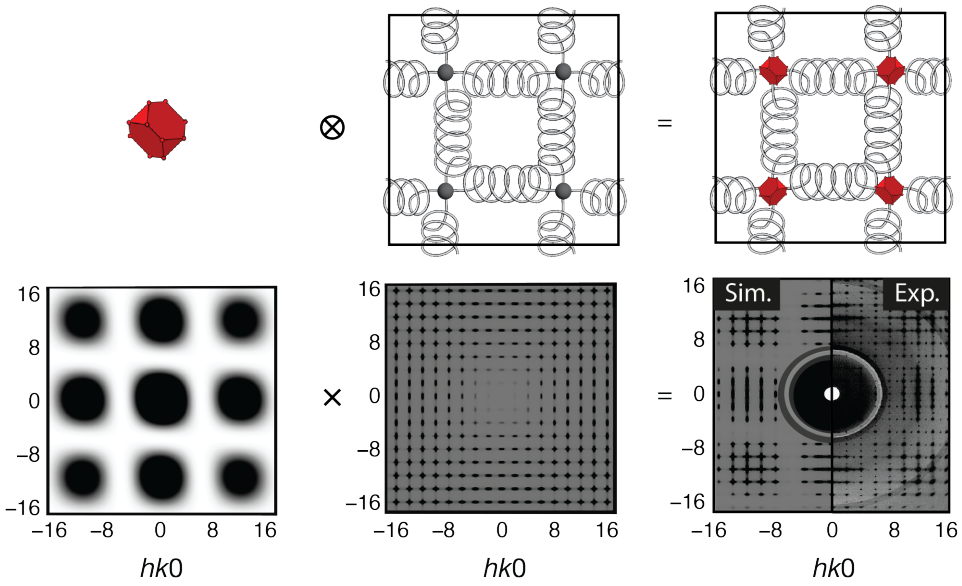

Figure 6.6: Adding back in the node form factor will improve the TDS match for MOF-5. For MOF-5, the tetrahedral Zn_4O node has two possible orientations and a corresponding form factor. The top line shows the process of convolving the Zn_4O node with the coarse-grained spring potential, effectively leading to a spring potential of Zn_4O nodes. The bottom line shows the Fourier transform equivalent. The multiplication of the two Fourier transforms leads to a much better match between the simulated and the experimental diffuse $hk0$ planes.

reasonably well with the shape of the experimental diffuse scattering, yet the clear modulation of the intensity is missing. Of course, by coarse-graining the structure down, the shape of the nodes and linkers have been lost. The Zn_4O node has a distinct shape and form factor that contributes to the diffuse scattering intensity (Fig. 6.6).

In fact, for the atomic displacements associated with the 'framework modes', the nodes can be assumed to be relatively undistorted, hence the contribution to the diffuse is just the convolution between the nodes themselves and their displacements. This is analogous to convolving a motif (the nodes) with the lattice (the displacements). This can then be calculated *via* the product of the Fourier transforms of the node and the phonon motions (Fig. 6.6). Here, one can see the quality of the match, with the modulation arising from the node form factor.

6.3.3 Mechanical flexibility with $NH_4Zn(HCOO)_3$

Ammonium zinc formate, NH4Zn(HCOO)$_3$, adopts the achiral Sohncke hexagonal space group $P6_322$, and is isostructural to other members of the $NH_4M(HCOO)_3$ family (M = Mn^{2+}, Co^{2+}, Ni^{2+} at room temperature).[270] Its topology is $4^9 \cdot 6^6$ (**acs**) such that each ZnO_6 metal node is involved in nine four-membered and six six-membered rings.[271,272] The hexagonal channels are occupied by the NH_4^+ cations that exhibit orientational disorder at room temperature. Upon cooling, there is a paraelectric to ferroelectric transition ($P6_322 \rightarrow P6_3$) at 255 K.[273,274] This phase transition has been associated with ordering of NH_4^+ cations in the channels, from a single site to three crystallographically distinct ammonium environments. The **acs** topology of the framework leads to wine-rack-like motifs within the structure similar to those found in $Ag_3Co(CN)_6$.[275] $NH_4Zn(HCOO)_3$, therefore, also exhibits negative linear compressibility (NLC) along its *c*-axis. This NLC behaviour was previously shown in a high-pressure single-crystal X-ray diffraction experiment using a diamond anvil cell and paraffin oil as a hydrostatic pressure-transmitting medium.[272] The volume change of $NH_4Zn(HCOO)_3$ was approximately 3 % per GPa, whilst analysis of the change in lattice parameters revealed that the *a*- and *b*-axes were highly compressible (linear compressibility along *a* and *b* of 15.8 TPa^{-1}) whilst the *c*-axis exhibited NLC of $-1.8\,TPa^{-1}$ along its axis.

The mechanical flexibility of $NH_4Zn(HCOO)_3$ is therefore an interesting case study for the 'framework mode' model. Again, the structure was coarse-grained and its k_{harm} and k_{bend} parameters optimised to fit the experimental bulk modulus (Table. 6.3). The TDS intensity of $NH_4Zn(HCOO)_3$ was measured on the in-house diffractometer at 300 K. This is above the phase transition of $NH_4Zn(HCOO)_3$, such all the diffuse

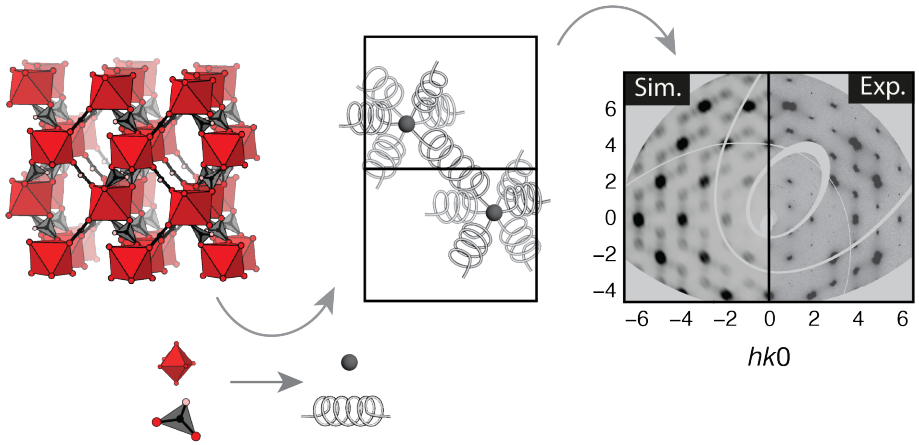

Figure 6.7: 'Framework mode' methodology for $NH_4Zn(HCOO)_3$. The ammonium ions are ignored, the Zn atoms are replaced by placeholder atoms, and the formate linkers are replaced by harmonic springs. Again, the TDS can be simulated and compared to experiment.

scattering originates from TDS. Below 255 K, sharp 1D streaks of diffuse scattering associated with the correlated disorder of ammonium channels can be seen when viewing planes perpendicular to the channels.[224] The match between the experimental and simulated patterns is quite good. A molecular form factor that includes half of the linkers could also be included to better match the modulated intensity.

Table 6.3: Coarse-grained parameters for $NH_4Zn(HCOO)_3$

k_{harm} (eVÅ^{-2})	k_{bend} (eVrad^{-2})	B_0^{cg} (GPa)	B_0^{exp} (GPa)
5	4	43.4	39.2

The advantage of a coarse-grained potential for a topology is that its mechanical responsiveness can be calculated rapidly. The changes in cell volumes and lattice parameters as a function of pressure are plotted and compared to the previous DFT studies on this work (Fig. 6.8). First, the match with the experimental data from Ref. 272 is excellent. Both the change in volume and the quasi-linear responses in lattice parameters are well-replicated, with the NLC of the *c*-axis also captured.

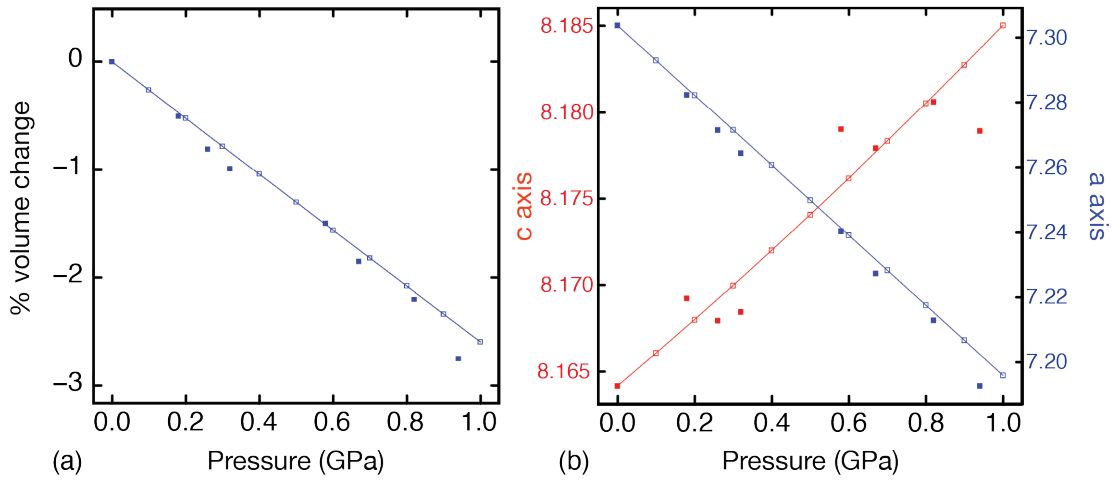

Figure 6.8: The volume change of $NH_4Zn(HCOO)_3$ under pressure (a) and the corresponding changes in cell axes (b). Since $NH_4Zn(HCOO)_3$ adopts $P6_322$ symmetry, the a- and b-axes are equivalent. Filled squares are the experimental values from Ref. 272 and the unfilled squares are the coarse-grained spring potential. Both trends are well-replicated. Note for (b) that the c-axis follows the left hand y axis and the a- and b-axes follow the right hand y axis.

This case study further confirms that the mechanical flexibility of framework materials is determined by the network topology and the relative strengths of the associated bending and stretching interactions. Furthermore, the ability of a computationally inexpensive coarse-grained model to accurately capture these properties demonstrates the predictive power of this approach.

6.3.4 NTE with $Zn(CN)_2$

Our initial two cases demonstrate the model's intuitive strengths. The accurate prediction of TDS is expected, as it is dominated by low-frequency framework phonons that the model is designed to capture. Similarly, the model's ability to reproduce the mechanical properties of $NH_4Zn(HCOO)_3$ is a direct outcome of fitting the coarse-grained parameters to the elastic properties of the framework, resulting in a close match with experimental measurements.

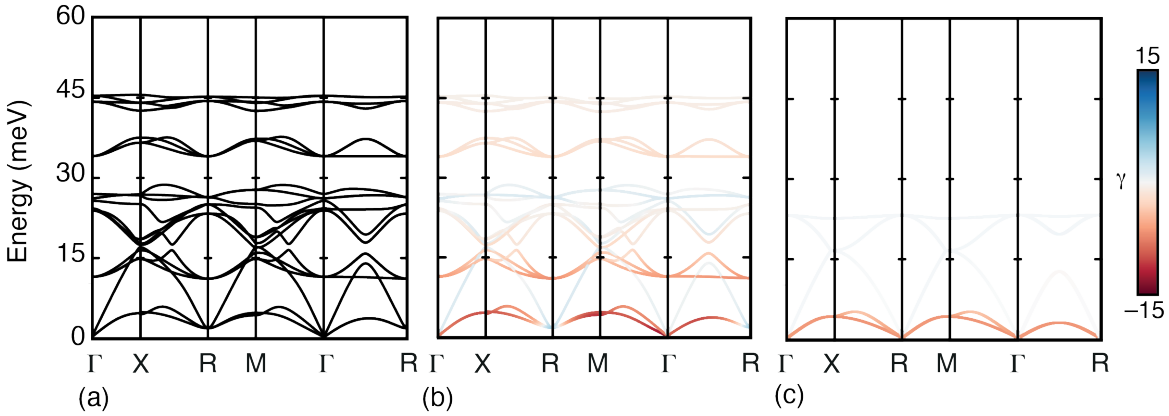

Figure 6.9: The full (a) and Grüneisen-weighted (b) phonon dispersion curves for $Zn(CN)_2$ compared to the Grüneisen-weighted coarse-grained equivalent (c). Note how the coarse-grained potential also has its TA modes with negative Grüneisen parameters. The largest magnitude is -9 compared to approximately -15 for the DFT-calculated phonon dispersion curves.

Finally, the model is tested against the NTE behaviour of $Zn(CN)_2$. The ability of a seemingly 'harmonic' model to capture any thermal expansion may appear counter-intuitive. The key insight, however, lies in the E_{three} bending term. While the potential is harmonic in the angular coordinate, the non-linear transformation to Cartesian coordinates introduces an effective anharmonicity in the interatomic distances. It is this implicit anharmonicity in the bending term that gives rise to an asymmetric restoring potential and enables the simulation of thermal expansion.

The previous chapter showed how the acoustic modes, or 'framework modes', were crucial especially in the low-temperature regime. The coarse-grained model should be able to capture this behaviour and qualitatively measure its contribution to the NTE. The Grüneisen parameters of the phonon modes were calculated and are shown to be similar to those previously calculated *via* DFT for the same modes (Fig. 6.9).

An MD simulation was also run with an interatomic potential that used the parameters in Table. 6.1. A $6 \times 6 \times 6$ supercell of the coarse-grained cell containing

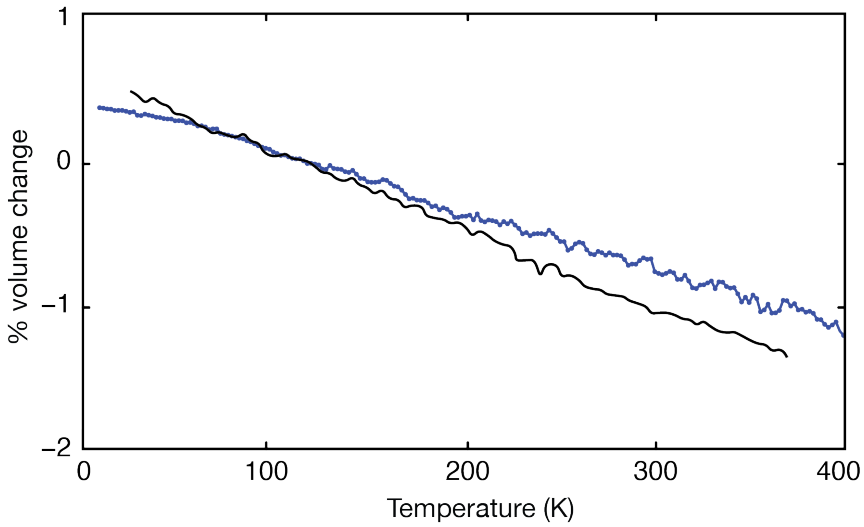

Figure 6.10: The change in volume for $Zn(CN)_2$ over the 5–400 K temperature range for experiment (black) and the coarse-grained supercell (blue). The experimental data (black) is from Ref. 251. The percentage change is with respect to the 100 K structure for both. The coarse-grained model also exhibits NTE although the magnitude is less than that observed experimentally probably due to the lack of RUMs in the 'framework mode' picture.

432 Zn atoms was used. A Parrinello–Rahman barostat[206] was used for the *NPT* simulation with a time step of 1 fs, a temperature damping constant of 10 fs, and a pressure damping constant of 100 fs. Whilst all atoms had randomly initialised velocities at 5 K, the Zn atoms constituting both frameworks had to be grouped together, and the overall initial velocities of both frameworks were set to zero. This was to prevent each framework drifting through the other. After equilibration for 1 ns at 5 K, the temperature was then ramped up from 5 K to 405 K over 10 ns. The relative volume change was then compared to previously measured experiments (Fig. 6.10).[251]

There are two key observations. First, the $Zn(CN)_2$ cell shows NTE over the temperature range. This confirms that the 'framework modes' are capable of rationalising much of the NTE behaviour. Moreover, the ease of bending of the $Zn(CN)_2$ framework ensures that the magnitude of the Grüneisen parameter is such that the PTE character of the higher-energy modes are unable to counteract the NTE even

at higher temperatures. So, there is no NTE → PTE transition over the 5–400 K temperature range. The second key point is that the magnitude of the NTE over this temperature range is less than that measured experimentally even if the phonon mode energies and Grüneisen parameters are similar. The larger magnitude in the experimental NTE points to the contribution of RUMs in $Zn(CN)_2$.

6.4 Outlook

A simple coarse-graining model has been developed that adequately captures the low-energy modes of complex framework materials. Its advantage is two fold. Its speed allows one to calculate quickly the low-energy 'framework modes' of the system and to compare qualitatively the coarse-grained simulations to experimental measurements. For modulated diffuse scattering of complex framework materials, this method can be used as a quick test to model the scattering and ascertain the TDS contribution from the framework topology. The gold standard of expensive *ab initio* calculations and beamtime can be more effectively used for systems that cannot be described by this simple model. Diffuse scattering that is not captured by the 'framework modes' is often indicative of short-range order or low-energy optic modes. The tilts in perovskites, for example, will appear in TDS measurements, and not be captured by the model.

Additionally, this coarse-grained method can be used to efficiently perform computational screening of framework structures. Large structural databases may be coarse-grained and their elastic constants calculated using this 'framework modes' methodology. Structures that display anomalous mechanical properties, such as a negative Poisson ratio, may be more readily identified.

Perhaps more importantly, the coarse-graining enables the analysis of certain key phonon modes in complex systems. Even with full DFT-calculated phonon dispersion curves, it is often difficult to isolate the important phonons or ascertain the microscopic origin of the phonon mode (as for $Zn(CN)_2$). This coarse-grained model has the advantage of paring down these often complex phonon dispersion curves. This approach aims to facilitate the evaluation of the role that low-energy 'framework modes' play in a given property of interest. Conversely, the absence of such a correlation indicates that different mechanisms are responsible.

7

The Anisotropic Heisenberg Quaternion Chain and its Realisation in $Ni(CN)_2$

7.1 Introduction

In previous chapters, it is clear how coarse-graining can simplify complex dynamics. We have used the RUM model and 'framework modes' to understand the key phonon modes of our systems. Effectively, by treating groups of atoms as rigid polyhedra, the RUM model decreases the total number of degrees of freedom. Yet, alternative dimensional abstractions, that often further reduce the total number in degrees of freedom can be achieved. In fact, the A, B, and C notation used by crystallographers to describe 3-D (111) close-packed planes of atoms is an example of this. Hexagonal close-packed systems can be simply described as (...ABABABAB...) whilst cubic close-packed systems are (...ABCABCABC...). This 'coarse-graining' allows us to quickly describe the stacking behaviour of systems in a shorthand form whilst also helping with the conceptual understanding of the problem at hand. It is much more efficient (and easier) to discuss the stacking behaviour of close-packed (111) atomic planes *via* their assigned letters rather than their particular atomic shifts. This chapter aims to solve complex structural problems with a similar coarse-grained approach. Rather than the (111) planes of atoms, the abstractions described in this chapter treat systems with columnar shifts (AgCN/AuCN) and layer shifts ($Ni(CN)_2$). For linear chains of atoms the columns are treated as collective objects, whilst for the layered materials, it is the layers themselves that are abstracted (Fig. 7.1). We note that for both these cases, the collective objects (chains and layers) only have three

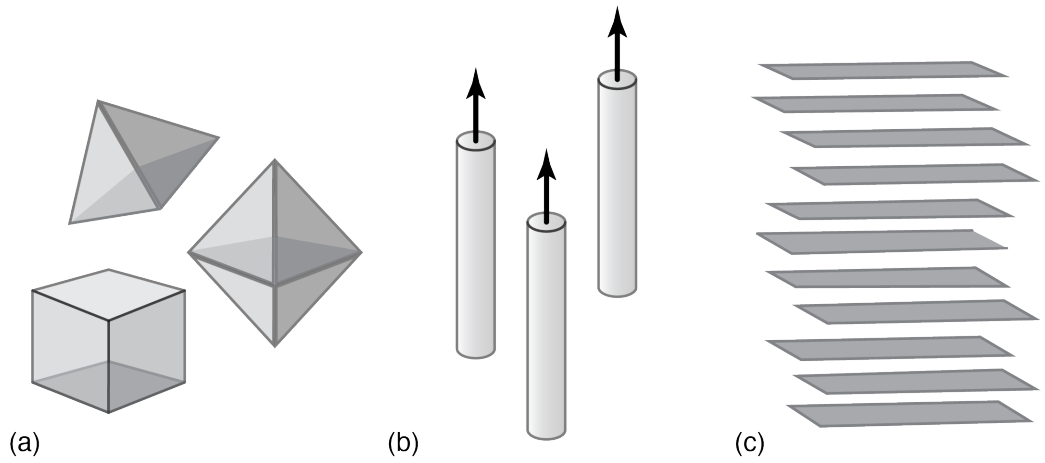

Figure 7.1: (a) RUM model abstraction: groups of atoms are treated as rigid polyhedra. (b) Linear chains of atoms treated as collective objects with their displacement along the z-direction being key. (c) Here, layers of a material are treated as collective objects and can be displaced in both the x- and the y-directions.

translational degrees of freedom each. For the linear chains, the key degree of freedom corresponds to displacements along the z-direction. For the layers, however, it is the displacements along the x- and y-directions that are the most important.

This treatment is particularly useful for structures with significant structural disorder. The PES of a material can be approximated by an interlayer potential governed by effective interactions between its constituent collective objects. As a result, the origin of the structural disorder and the key effective interactions can become much more apparent. Additionally, parallels can be drawn between these coarse-grained potentials and those of pseudo-spin models. Re-casting complex structures as pseudo-spin models can allow for the comparison between complex chemical phases and their magnetic analogues. In this chapter, an inter-layer potential of $Ni(CN)_2$ is shown to encode interactions that drive its complex, disordered stacking behaviour. In addition, we map the layer shifts of $Ni(CN)_2$ onto 4-D pseudo-spins (quarternions) to create a pseudo-spin model for its disordered layered structure. We begin by introducing the usage of pseudo-spin models in structural chemistry: both for modelling discrete stacking

sequences in layered close-packed structures and with the one-dimensional chain coinage metal cyanides. The X-ray powder scattering and disordered structure of $Ni(CN)_2$ are then described, followed by a discussion of how this pseudo-spin model effectively captures the layer interactions that drive its overarching disordered layer structure.

7.2 Background

The representation of collective structural degrees of freedom in terms of effective variables is a standard approach for abstraction of material behaviour. These mappings allow for the interpretation of phase behaviour in terms of statistical mechanical models based on effective interactions between these variables.[277,278] This methodology has formed the basis for a large variety of key results across condensed matter physics, where complex phase behaviour is the result of the subtle balance between competing interactions.

7.2.1 Ising Description of Layered Structures

Traditionally, pseudo-spin models have been useful in understanding different structural phases. These pseudo-spin models can vary both in the dimensionality of the pseudo-spin and/or the lattice on which the pseudo-spins reside. The Ising model is one of the most famous.[279] Here, the pseudo-spin has a magnitude of 1 ($|\mathbf{S}| = 1$) and is confined to a single axis (z, say), such that it can only be in one of two states—up or down ($\mathbf{S}_z = \pm 1$). Originally used in magnetism to describe ferromagnetic (... ↑↑↑↑↑↑ ...) and antiferromagnetic (... ↑↓↑↓↑↓ ...) behaviour, the Hamiltonian for

the exchange interaction between Ising pseudo-spins is given as follows:

$$\mathcal{H} = -\sum_{i,j} J_{ij} s_i s_j, \tag{7.1}$$

where s_i is the Ising pseudo-spin variable that can take values of $+1$ (up) or -1 (down), J_{ij} is the interaction parameter between the pseudo-spins, and the sum is over all sites. Since J_{ij} drops off dramatically with distance, it is often sufficient to use J_1 (nearest-neighbour interactions) to a first approximation. Stacking behaviour is a well-characterised pseudo-1-D model where each (111) plane can be characterised by a line of pseudo-spins. For stacking faults, layer planes are assigned an s_i of $+1$ if they follow the general packing sequence (i.e., ...ABCAB**C**... for a cubic system) and an s_i of -1 if they lead to a stacking fault (i.e., ...ABCAB**A**...).[280] Clearly, only taking nearest-neighbour interactions into account is insufficient; there would be no driving force for an AB sequence to end up as ABC rather than ABA (for cubic close-packed). This degeneracy between stacking fault and 'correct' stacking sequence can be lifted by introducing next-nearest neighbour interactions. These have been crucial in understanding the stacking faults present in Ni, Al, Cu, and Mg.[281–283]

7.2.2 The ANNNI Model

Indeed, next-nearest neighbour interactions are often important in properly modelling structural analogues. The anisotropic next-nearest neighbour Ising model (ANNNI) includes these interactions and has the following pseudo-spin Hamiltonian:[284,285]

$$\mathcal{H} = -J_1 \sum_{\langle i,j \rangle} s_i s_j - J_2 \sum_{\langle\langle i,j \rangle\rangle} s_i s_j, \tag{7.2}$$

where J_2 is the effective interaction parameter between next-nearest neighbours.

This simple interplay between nearest and next-nearest interactions leads to a rich phase behaviour (Fig. 7.2 (a)). For $T = 0$, when $J_2 > 0$ (ferromagnetic next-nearest

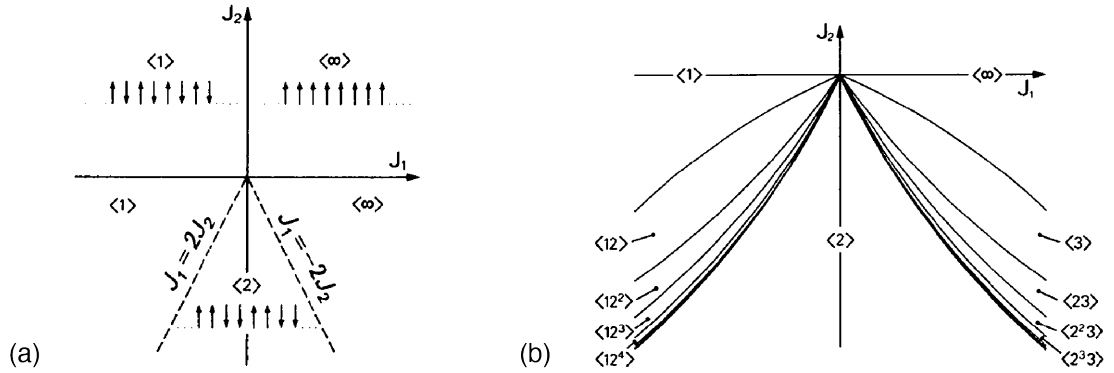

Figure 7.2: (a) Phase diagram of ANNNI model at 0 K. When $J_2 < 0$ phase lines emerge at $|J_1| = 2|J_2|$. (b) Phase diagram of ANNNI at temperature. The phase lines split and broaden with increasing temperature such that a range of stable sequences are possible. Figure adapted and reproduced from Ref. 292.

neighbour interactions), all possible states are ordered and depend solely on J_1. For $J_1 > 0$, the ground state is ferromagnetic (... ↑↑↑↑↑↑ ...), and for $J_1 < 0$, the ground state is antiferromagnetic (... ↑↓↑↓↑↓ ...).

When $J_2 < 0$, the phase behaviour becomes more interesting as the J_1 and J_2 terms drive different orderings. The notation used to describe these states is analogous to Zhdanov notation.[286,287] Generally, $\langle n_1 n_2 ... n_m \rangle$ refers to a state where the repeating sequence is made of m bands of length $n_1, n_2, ...n_m$. For example, the sequence (... ↑↑↓↓↑↑↑↓↓↓↑↑↑↓↓↓↑↑ ...) would be $\langle 223333 \rangle$ or $\langle 2^2 3^4 \rangle$. The ferromagnetic and antiferromagnetic ground states are denoted as $\langle \infty \rangle$ and $\langle 1 \rangle$, respectively.

If J_1 is small, one arrives at <2> (↑↑↓↓) for the ground state since J_2 dominates. When $|J_1| = 2|J_2|$, many phases become degenerate. No $\langle 1 \rangle$-bonds (↑↓) lie on the line between $\langle \infty \rangle - \langle 2 \rangle$ whilst all phases with $\langle 1 \rangle$ (↑↓) or $\langle 2 \rangle$ (↑↑↓↓) bonds have the same energy on the $\langle 1 \rangle - \langle 2 \rangle$ line. In addition, at higher temperatures, where $0 < k_B T << J_1$, in the vicinity of the multiphase lines, multiple sequences of $\langle 2^{n-1} 3 \rangle$ and $\langle 12^n \rangle$ become stable (here, $n \in \mathbb{N}$).[285,288] This is illustrated in Fig. 7.2 (b) where the widths of the

phases are proportional to $\exp(-J_1/k_{\mathrm{B}}T)$ and the associated phase transitions are all first-order. Increasing the temperature further leads to significantly disordered arrangements.[289,290] The ANNNI model beautifully shows how simple competing interactions can lead to complex and rich phase behaviour.

7.2.3 The ANNNI Model in structural chemistry

Whilst originally formulated for magnetic systems (a 3-D ANNNI model was developed in 1961 by Elliott for the sinusoidally ordered state of Er[278,284]), mappings of ANNNI models to structural chemistry have proved crucial for a number of systems that exhibit polytypism. These structures, that are assembled by structurally compatible units, can have a range of stacking sequences with long periodicities.[291] The spinelloids (AB_2O_4), pyroxene ($MgSiO_3$), wollastonite ($CaSiO_3$), and SiC have all been explored in the context of the ANNNI model.[292] For spinelloids, there are two structural units that are packed normal to the [100] direction.[293,294] It is by mapping these structural units to up or down pseudo-spins that one can then use the ANNNI model (Fig. 7.3 (a)).

Six stacking sequences corresponding to $\langle 1\rangle$, $\langle 2\rangle$, $\langle 3\rangle$, $\langle 12\rangle$, $\langle 13\rangle$, and $\langle 12^2\rangle$ are found in the $Ni_2SiO_4{-}NiAl_2O_4$ spinelloids.[295,296] These states have been shown to be highly dependent on composition. Different compositions affect the J_1 and J_2 interactions

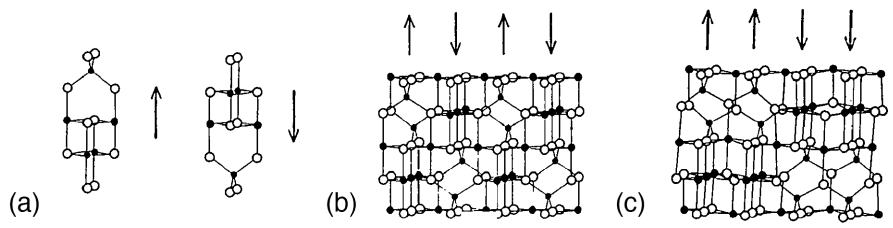

Figure 7.3: (a) Shows the two orientations of the spinelloid secondary building unit and the corresponding pseudo-spin. (b) The spinel phase corresponding to $\langle 1\rangle$. (c) The β-phase corresponding to $\langle 2\rangle$. Figure adapted and reproduced with permission from Ref. 292

.

and result in different stable phases.[292] The phase behaviour of the spinelloids and pyroxene under increasing pressure can also be shown to correspond to trajectories on an ANNNI phase diagram using key J_1/J_2 terms.[296,297]

The ANNNI model does have its limitations. For the spinelloids for example, the $\langle 13 \rangle$ polytypic structure, observed experimentally, does not occur in the ANNNI phase diagram.[292] In addition, at temperature, the ANNNI model captures significant thermal disorder that may not be applicable to real, close-packed compounds.

7.2.4 Continuous Spin Models

Spin models may also be continuous to capture extra degrees of freedom. There are, in fact, continuous analogues to the ANNNI model that include next-nearest neighbour interactions. Historically, these models were used to rationalise Lifshitz points (triple points for paramagnetic, ferromagnetic, and helimagnetic phases) in magnetic systems.[278,298] The phase diagram is similar to that of ANNNI in that the effective J_2 interaction is crucial in stabilising complex phases. For a one-dimensional chain of n-component spin-vectors, at $T = 0$, one can have a ferromagnetic state ($J_1 > 0, J_2 > -J_1/4$), an antiferromagnetic state ($J_1 < 0, J_2 > J_1/4$), and a helical state ($J_2 < -|J_1|/4$) (Fig. 7.4).[299,300] These systems can exhibit spatially modulated spin patterns in their ground state. $FeMgBO_4$ exhibits 1-D spin correlations within the zig-zag chains of its Fe^{3+} ions.[301] As it is cooled, it displays a helical state of its magnetic spins. Moreover, excitations of such 1-D spin chain systems are of particular interest. $Sr_2V_3O_9$ can be considered as a host of weakly coupled $S = \frac{1}{2}$ chains (V^{4+}, $[Ar]3d^1$, is magnetic).[302] Its magnetic excitations are gapless and a spinon continuum can be seen.

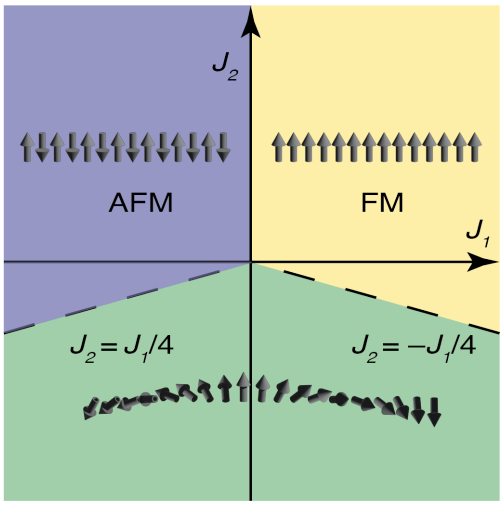

Figure 7.4: Schematic phase diagram for continuous spin model at 0 K where different interaction parameters lead to ferromagnetic (yellow – FM), antiferromagnetic (blue – AFM), and helical spin states (green).

7.2.5 AuCN and AgCN: Classical XY Pseudo-spins on a Triangular Lattice

Structural analogues to spin-systems with continuous degrees of freedom do exist and this is how the structure of $Ni(CN)_2$ can be best understood. Previous work from the group drew parallels between the one-dimensional chain coinage metal cyanides, AuCN and AgCN, and the classical spin XY model on a triangular lattice.[303] We will come to use a similar methodology for $Ni(CN)_2$, but give first a thorough description of the AuCN and AgCN cases here.

Both AuCN and AgCN form assemblies of one-dimensional chains where each metal is linearly coordinated to two cyanide ligands. For both, these rod-like chains of -(CN)-M-(CN)- are arranged on a triangular lattice.[304–306] Distinct structure-types emerge, characterised by the relative displacement of the chains in relation to each other along the crystallographic c-axis (here the z-direction) as shown in Fig. 7.5 (a).[307] Since these chains are periodic, the system is invariant with respect to lattice translations $z \to z+n$ where $n \in \mathbb{Z}$ such that the effective phase $\theta = 2\pi z$ is a suitable representation of this

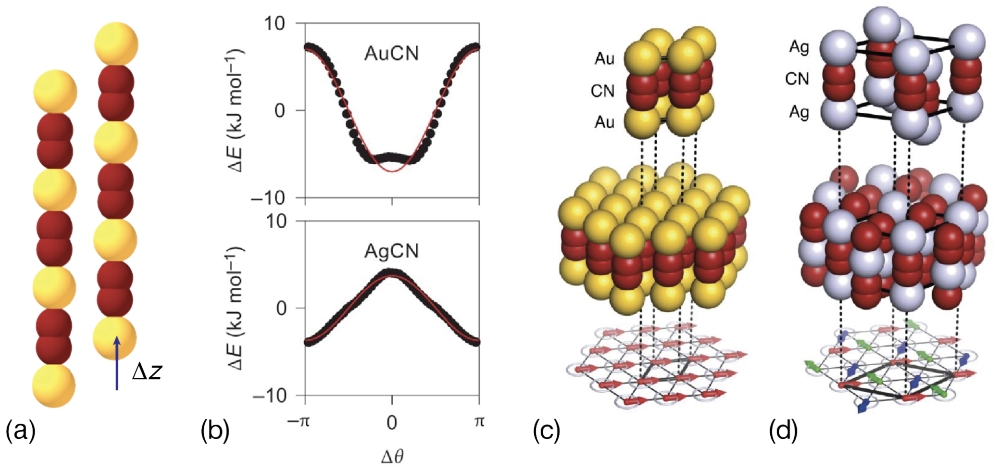

Figure 7.5: (a) The relative displacement Δz between chains differs for both AuCN and AgCN. (b) The PES for both AuCN (top) and AgCN (bottom) with respect to the phase angle where $\Delta\theta = 2\pi\Delta z$. (c) Shows the relationship between the chain displacement of $(\Delta z = 0)$ and a ferromagnetic arrangement of the XY spins on the hexagonal lattice for AuCN. (d) Shows the relationship between the chain displacement $(\Delta z = \pm\frac{1}{3})$ and an antiferromagnetic arrangement of pseudo-spins on a triangular lattice for AgCN. Figure adapted and reproduced with permission from Ref. 303.

same degree of freedom. As the chains can shift relative to each other in the z-direction, the inter-chain potential energy, E, can be written in terms of Δz and, hence, $\Delta\theta$.

The inter-chain PES was calculated for both AuCN and AgCN using *ab initio* quantum mechanical calculations (Fig. 7.5 (b)). Interestingly, whilst metallophilic interactions dominate for AuCN such that the chains prefer to have a Δz and $\Delta\theta$ of 0, for AgCN, the energy minimum occurs at a $\Delta z = \frac{1}{2}$ $(\Delta\theta = \pi)$ as the electrostatic interactions are dominant. For both AgCN and AuCN the energy dependence on relative phase shift can be well-approximated by their first-order Fourier component:

$$E = J\cos(\Delta\theta), \tag{7.3}$$

where $J = -7.0\,\mathrm{kJ\,mol^{-1}}$ and $+3.7\,\mathrm{kJ\,mol^{-1}}$ for AuCN and AgCN, respectively.

The similarity to the spin Hamiltonian for the XY triangular antiferromagnet is clear. Ascribing XY pseudo-spins to each chain where $S = (\cos(\theta), \sin(\theta))$, an effective

Hamiltonian can be shown to adopt the general form:

$$\mathcal{H} = J \sum_{\langle i,j \rangle} \cos(\theta_i - \theta_j) = J_{\mathrm{XY}} \sum_{\langle i,j \rangle} \mathbf{S}_i \cdot \mathbf{S}_j, \tag{7.4}$$

where the sum is over neighbouring chains i, j.

The XY pseudo-spin model allows us to interpret the different structures that AuCN and AgCN adopt. For AuCN, the metallophilic interactions dominate such that $J_{\mathrm{XY}} < 0$. AuCN adopts a ferromagnetic arrangement of the XY pseudo-spins on the hexagonal lattice, with the chains not being shifted with respect to each other ($\Delta z = 0$) as shown in Figure 7.5 (c).

AgCN is perhaps more interesting. As discussed previously, the electrostatic interactions outweigh the argentophilic interactions, leading to an antiferromagnetic interaction between neighbouring pseudo-spins and $J_{\mathrm{XY}} > 0$. An Ising anti-ferromagnet is frustrated on a triangular lattice. Whilst two Ising spins can be aligned anti-parallel with respect to one another, the third spin must always be parallel to at least one of the first two spins. The continuous XY spin model lifts this frustration giving a ground state in which triplets of neighbouring pseudo-spins are rotated 120° away from each other. The structural analogy is that the AgCN chains are all shifted by a $\pm\frac{1}{3}$ displacement in the z-direction away from each other, and this is found experimentally (Figure 7.5 (d)). Indeed, for AgCN, its low energy structure could not have been mapped onto a discrete pseudo-spin Ising model. This explains the different space groups of $P6/mmm$ for AuCN and $R\bar{3}m$ for AgCN.

Additional terms can be used in the spin Hamiltonian to describe more complex cases. The mixed-cation system $Ag_{0.5}Au_{0.5}CN$, for example, has a more elaborate

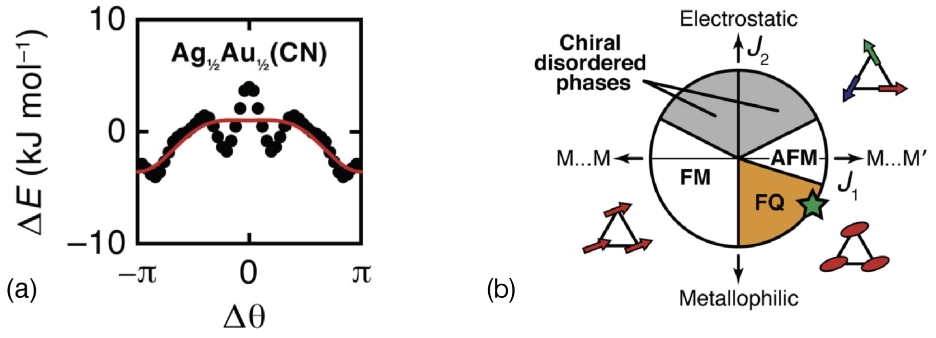

Figure 7.6: (a) The BLBQ energy profile. The added complexity in shape requires extra terms in the pseudo-spin Hamiltonian. (b) The BLBQ phase diagram. There are ferromagnetic (FM), antiferromagnetic (AFM), ferroquadrupolar (FQ), and chiral disordered phases. The pseudo-spin model for $Ag_{0.5}Au_{0.5}CN$ falls in the FQ ordered region as shown by the green star. Figure adapted and reproduced with permission from Ref. 303.

energy profile due to its different metallophilic interactions: Ag· · ·Ag, Ag· · ·Au, and Au· · ·Au (Fig. 7.6 (a)).

The more complex energy profile now requires at least two Fourier components to be well fitted. The corresponding Hamiltonian is now well approximated by the bilinear biquadratic (BLBQ) XY model where the second Fourier component for 1-D systems (the cosine squared term) is used:[308]

$$\mathcal{H} = J_1 \sum_{\langle ij \rangle} \mathbf{S}_i \cdot \mathbf{S}_j + J_2 \sum_{\langle ij \rangle} |\mathbf{S}_i \cdot \mathbf{S}_j|^2 = J_1 \sum_{\langle ij \rangle} \cos(\Delta\theta_{ij}) + J_2 \sum_{\langle ij \rangle} \cos^2(\Delta\theta_{ij}). \qquad (7.5)$$

An intuition of the physical interactions that these Fourier components are capturing is particularly useful. Here, the first Fourier component captures the difference between homometallic (Ag· · ·Ag or Au· · ·Au) and heterometallic (Ag· · ·Au) contacts. This first Fourier component has a periodicity of 2π. The second Fourier component is the one reminiscent of the earlier pseudo-spin-Hamiltonian for AuCN and AgCN since it describes the average between the electrostatic and metallophilic interactions. This second Fourier component now has a periodicity of π since the Ag and Au metals are not differentiated with this term. The parametrisation to the *ab initio* energy

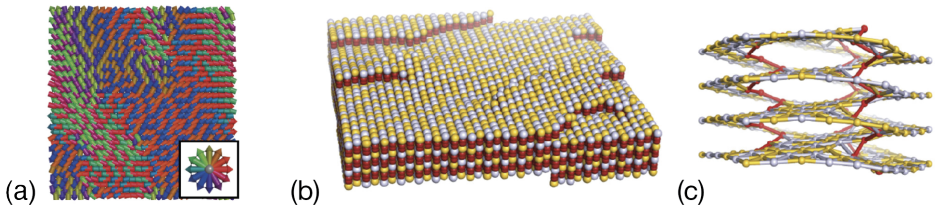

Figure 7.7: (a) Spin vortices predicted by the BLBQ spin model in the FQ region of the phase diagram. (b) Structural model of $Ag_{0.5}Au_{0.5}CN$ generated by previous work shows lack of Ag/Au order. (c) Screw dislocations in previous configuration are highlighted as the structural analogue of the spin vortices. Figure adapted and reproduced with permission from Ref. 303.

profile led to values of $J_1 = +2.31\,\mathrm{kJ\,mol^{-1}}$ and $J_2 = -1.28\,\mathrm{kJ\,mol^{-1}}$. Hence, there is a strong preference for heterometallic contacts whilst metallophilic interactions slightly outweigh the electrostatic interactions.

Using these interaction parameter values, one can map the $Ag_{0.5}Au_{0.5}CN$ room temperature phase to the ferroquadrupolar (FQ) phase of the BLBQ phase diagram. In this phase, dipolar disorder couples with hidden FQ order. The magnetic phase had been predicted to be unstable to vortices at temperature (Fig. 7.7 (a)). These topological defects were shown to be analogous to screw dislocations found in $Ag_{0.5}Au_{0.5}CN$ and corresponded to experimentally observed selective peak broadening in the PXRD (Fig. 7.7 (b)–(c)).[309]

Such pseudo-spin mappings allows for the creation of physical, chemical analogues to complex magnetic phases and their emergent, exotic behaviour. The next logical step is to increase the dimensionality: from 1-D chains and XY pseudo–spins to 2-D layered systems and quaternion pseudo-spins.

7.2.6 $Ni(CN)_2$: a 2-D Analogue to AuCN/AgCN

$Ni(CN)_2$ is a layered inorganic compound composed of sheets of Ni^{2+} coordinated to four CN^- ions in a square-planar arrangement (Fig. 7.8 (a)).[310] The cyanides exhibit head-to-tail disorder.[310] The strong intra-layer interactions lead to ordering in the layer directions, whilst the comparatively weak electrostatic inter-layer interactions no periodic ordering in the perpendicular direction except for the layer spacing. The layers are disorederd in the x- and y-directions. The experimental PXRD pattern of $Ni(CN)_2$ reflects this stacking behaviour: it contains a set of sharp reflections with a series of broad diffuse features with asymmetric Warren peak shapes (Fig. 7.8 (c)).[311] The sharp ($hk0$) and ($00l$) peaks correspond to the individual layer structure and layer spacing being well-defined, whilst the broad (hkl) peaks point to less distinct inter-layer correlations.

The crystal structure of $Ni(CN)_2$ has previously been interpreted in terms of a stacking fault model based on Ising-like degrees of freedom.[311] It was assumed that the driving force for inter-layer interactions was electrostatic such that the Ni^{2+} ions of subsequent layers would lie directly above CN^- ions. Since there are twice as

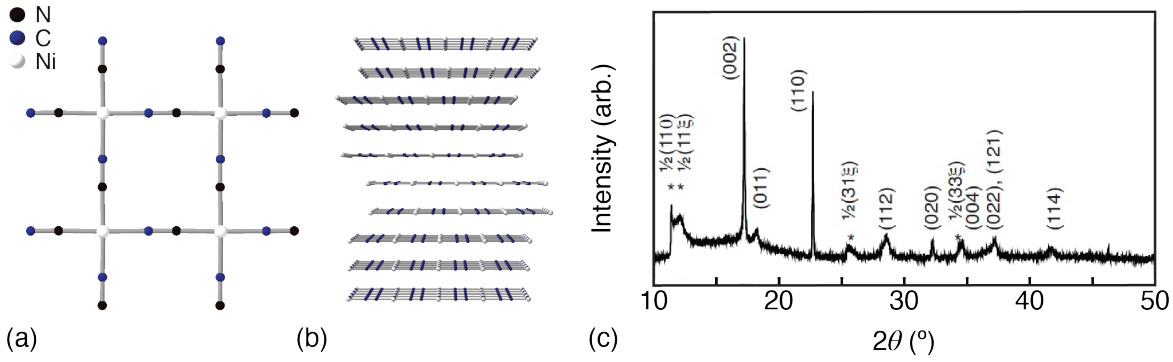

Figure 7.8: (a) Square planar $Ni(CN)_4$ units in $Ni(CN)_2$. (b) Disordered layered structure of $Ni(CN)_2$. (c) PXRD pattern of $Ni(CN)_2$ reproduced and adapted with permission from Ref. 311.

many cyanides as Ni^{2+} ions, the stacking faults were understood as the result of the choice between two energetically similar orientations for each layer (A, A′ and B, B′ with As and Bs in alternating layers). Weighting the layer probabilities appropriately (taking the next-nearest layers into account) and adding a Gaussian shear displacement perpendicular to the [001] direction led to a good match with the experimental PXRD pattern. Yet, this discrete model did not explain why the shear was needed.

Previous work described in the DPhil thesis of Dr Emma H. Wolpert (Ref. 312) sought to describe the stacking behaviour of $Ni(CN)_2$ *via* a continuous pseudo-spin model. A toy model of the PES of the layers found in $Ni(CN)_2$ was constructed using a simple electrostatic model. The Ni^{2+} and CN^- ions were treated as point charges. Four layers were used to construct this pseudo-PES (Fig. 7.9 (a)). Here, the first and third layers of $Ni(CN)_2$ were fixed at shifts of (0,0,0) and (0.5,0.5,0.5) with respect to each other. These layer shifts corresponded to the energetically equivalent layer shifts used in the previous Ising model. The second and fourth layers were then translated along the x and y directions. This gave a PES (Fig. 7.9 (b)) that was parametrised well by the following Hamiltonian:

$$\mathcal{H} = J \sum_{\langle ij \rangle} \{\cos\{2\pi(x_i - x_j)\} + \cos\{2\pi(y_i - y_j)\}\}. \tag{7.6}$$

This Hamiltonian only requires the first-order Fourier component in 2-dimensions and is effectively the first term in the 2-D Fourier expansion of the energy with respect to displacements ($\Delta\mathbf{r}$):

$$E(\Delta\mathbf{r}) = \sum_{\mathbf{G}} \cos(2\pi\mathbf{G} \cdot \mathbf{r}), \tag{7.7}$$

where $\mathbf{G}$ is the reciprocal lattice vector. Here, Eq.(7.7) considers $\mathbf{G} \in \langle 10 \rangle$ only. Using this Hamiltonian to drive a MC simulation, the diffraction pattern shown in Fig. 7.9 (c) (iii) was achieved.

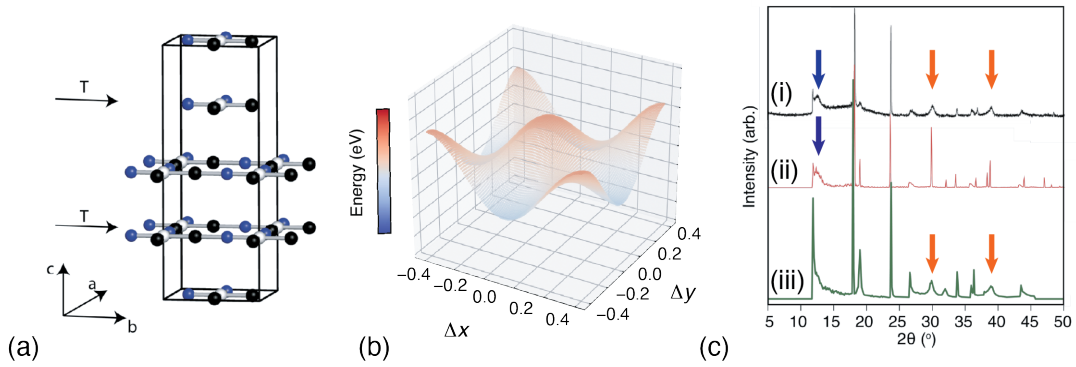

Figure 7.9: (a) Toy model used in Ref. 312. Both the first and third layers remain fixed, whilst the second and fourth layers are allowed to translate. (b) (i) Experimental PXRD pattern of $Ni(CN)_2$. (b) (ii) The Ising model fit including next-nearest neighbours and a Gaussian shear displacement. (b) (iii) The fit achieved by Ref. 312 using the toy model and only nearest-neighbour interactions. Selective peak broadening (orange arrows) is impressively achieved without the need for a Gaussian shear. The peak that arises due to next-nearest layer interactions (blue arrows), however, is not captured by this toy model). Figure adapted and reproduced with permission from Ref. 312.

The peak broadening is accurately reproduced by this toy model, which demonstrates that a PES with low curvature around its minima can capture the relevant layer shifts without requiring a global shear (orange arrows in Fig. 7.9 (c)). However, the model has clear limitations, indicating that it may be an oversimplification of the true PES of $Ni(CN)_2$. The fixing of the first and third layer positions when constructing the approximate PES is a significant simplification, as is the restriction to purely electrostatic interactions. In addition, the toy model is unable to reproduce the peak at 12.5°—this is consistent with previous work that attributed this peak to next-nearest layer interactions[311] (blue arrows in Fig. 7.9 (c)). These limitations imply that the true PES of $Ni(CN)_2$ possesses greater complexity than can be captured by a single Fourier component.

7.3 Results

7.3.1 Calculating the PES

Ideally, one should have an *ab initio* PES with respect to layer shifts. To construct our PES, single point energies of shifted layer pairs of $Ni(CN)_2$ were calculated using DFT. 121 configurations were used covering the -0.5 and $+0.5$ range of Δx and Δy shifts with an interval of 0.01 (Fig. 7.10 (a)). The two $Ni(CN)_2$ layers were separated by 3.2 Å with unit cell parameters of $a = b = 4.9$ Å as in the original discrete Ising model described in Ref. 311. The next-nearest pair of layers were kept 29 Å apart to ensure that the electrostatic interactions were kept between the layer pairs. Ultrasoft pseudo-potentials supplied as part of the CASTEP package were used together with the standard rSCAN functional. The integration of electronic states was performed using a Monkhorst–Pack grid of $7 \times 7 \times 1$ wave-vectors, a plane-wave cut-off of 1200 eV, and an electronic energy tolerance of 1^{-10} eV per atom.

This PES makes intuitive sense. When $\Delta x = 0$ and $\Delta y = 0$, there is an energy maximum: the positively charged Ni^{2+} ions lie directly above Ni^{2+} ions of the next layer, and similarly with the negatively-charged CN^- ions (Fig. 7.10 (b)). Moreover, an energy minimum occurs around when the Ni^{2+} ions reside above the CN^- ions and vice versa such as at $\Delta x = 0$ and $\Delta y = \pm 0.5$. Lastly, there are local maxima when the CN^- ions are on top of one another and the Ni^{2+} ions are shifted away such as at $\Delta x = +0.5$ and $\Delta y = +0.5$. The shape of this PES is the first point of difference with the toy model potential described previously. Indeed, for the toy model the local maxima are indistinguishable to the overall maximum since the first and third layers have been fixed (Fig. 7.9 (b)). The important detail however is the shallow well-like behaviour around the minima that allows for small layer shifts

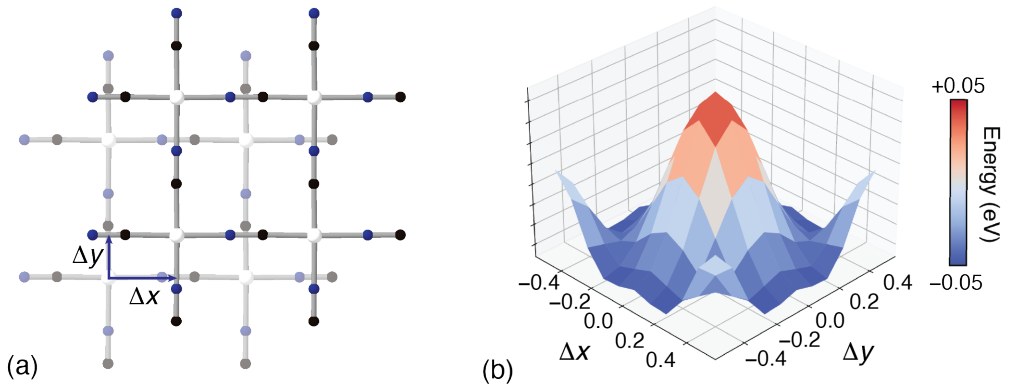

Figure 7.10: (a) Layer shifts are defined by Δx and Δy. (b) The PES of the pair of $Ni(CN)_2$ layers with respect to their layer shifts. The energies are given relative to the mean value.

between nearest-neighbours and is captured by both the toy and *ab initio* models. These allowed layer shifts are important in capturing the peak broadening found in the experimental PXRD patterns. The peak broadening can therefore be captured by these continuous pseudo-spin models, unlike the previous discrete models.

The next step is to parameterise the PES. The mapping used here is similar to the one used for the 1-D AuCN and AgCN cases. Since $Ni(CN)_2$ is periodic in both the x- and y-directions, the mapping now involves two phase angles $\theta = 2\pi\Delta x$ and $\phi = 2\pi\Delta y$. As a result, rather than an effective Hamiltonian with 2-D XY pseudo-spins, the effective Hamiltonian is now defined by four-dimensional pseudo-spins (quaternions).

7.3.2 The Fourier Components

To capture the PES shape, two Fourier components are needed. The first captures the central peak, whilst the second describes the minima. In terms of the physical mapping, the first Fourier component captures the energy difference between the overall maximum (no layer shift with Ni^{2+} and CN^- ions lying directly above like ions) and local maxima (Ni^{2+} ions shifted away from each other whilst CN^- ions remain

directly above each other). The second Fourier component captures the electrostatic interactions, where positive Ni^{2+} ions preferentially sit above the negative CN^- ions. This is similar to the BLBQ Hamiltonian where several Fourier components were needed to account for the more complex PES and the delicate balance between electrostatics and heterometallic/homometallic metallophilic interactions. In terms of the Fourier expansion of the energy, this is now expressed as follows:

$$E(\Delta\mathbf{r}) = \sum_{\mathbf{G}} \cos(2\pi\mathbf{G}\cdot\mathbf{r}), \tag{7.8}$$

where Eq.(7.8) considers $\mathbf{G} \in \langle 10\rangle$ (the first Fourier component) and $\mathbf{G} \in \langle 11\rangle$ (the second Fourier component). The first Fourier component for $Ni(CN)_2$ is analogous in form to that of the AuCN/AgCN systems. It is the summation of the cosines Δx and Δy and is plotted in Fig. 7.11 (a). Its pseudo-spin Hamiltonian is as follows:

$$\mathcal{H} = J\sum_{\langle ij\rangle}\frac{1}{2}\{\cos\{2\pi(x_i - x_j)\} + \cos\{2\pi(y_i - y_j)\}\} \tag{7.9}$$

. Using the mappings of $\theta = 2\pi\Delta x$ and $\phi = 2\pi\Delta y$, one can arrive at the following effective Hamiltonian:

$$\mathcal{H} = -J_{1a}\sum_{\langle i,j\rangle}\mathbf{p}_i\cdot\mathbf{p}_j, \quad \text{where} \quad \mathbf{p}_i = \frac{1}{\sqrt{2}}\begin{bmatrix}\cos(\theta_i)\\ \sin(\theta_i)\\ \cos(\phi_i)\\ \sin(\phi_i)\end{bmatrix}. \tag{7.10}$$

The second Fourier component is more interesting. Unlike 1-D systems, higher order Fourier components in 2-D systems cannot simply be expressed as powers of the first-order Fourier component. Indeed, in 2-D, the wave-vectors of the Fourier components can lead to differences in periodicities but also in direction, hence $\mathbf{G} \in \langle 11\rangle$. This $\pi/4$ rotation along the z-axis compared to the first Fourier component allows the second Fourier component to capture the local minima of the PES. As a result, the second Fourier component is expressed as the summation of the cosines of $\Delta x + \Delta y$ and

$\Delta x - \Delta y$ as shown in Fig. 7.11 (b). For this Fourier component, the phase angle mapping is $\alpha = 2\pi(\Delta x + \Delta y)$ and $\beta = 2\pi(\Delta x - \Delta y)$ such that the pseudo-spin Hamiltonian is:

$$\begin{aligned}\mathcal{H} &= J \sum_{\langle ij \rangle} \frac{1}{2}\{\cos\{2\pi[(x_i - x_j) + (y_i - y_j)]\} + \cos\{2\pi[(x_i - x_j) - (y_i - y_j)]\}\} \\ &= -J_{1b} \sum_{\langle i,j \rangle} \mathbf{q}_i \cdot \mathbf{q}_j \quad \text{where} \quad \mathbf{q}_i = \frac{1}{\sqrt{2}} \begin{bmatrix} \cos(\alpha_i) \\ \sin(\alpha_i) \\ \cos(\beta_i) \\ \sin(\beta_i) \end{bmatrix}.\end{aligned} \tag{7.11}$$

Combining both Fourier components together results in the following effective pseudo-spin Hamiltonian that describes two independent 1-D strings of unit quaternions:

$$\mathcal{H} = -J_{1a} \sum_{\langle i,j \rangle} \mathbf{p}_i \cdot \mathbf{p}_j - J_{1b} \sum_{\langle i,j \rangle} \mathbf{q}_i \cdot \mathbf{q}_j. \tag{7.12}$$

A least-squares fit, using a three-point Jacobian, resulted in the values shown in Table 7.1 where a is a constant term. The J_{1a}/J_{1b} ratio is 1.80, and the combined function is shown in Fig. 7.11 (d). The R^2 value is 0.869 for these parameter values.

Table 7.1: Parameter values for the DFT energy surface fit for pairs of Ni(CN)$_2$ layers

Parameters	J_{1a}	J_{1b}	a
eV	0.004079	0.007357	-4510.294

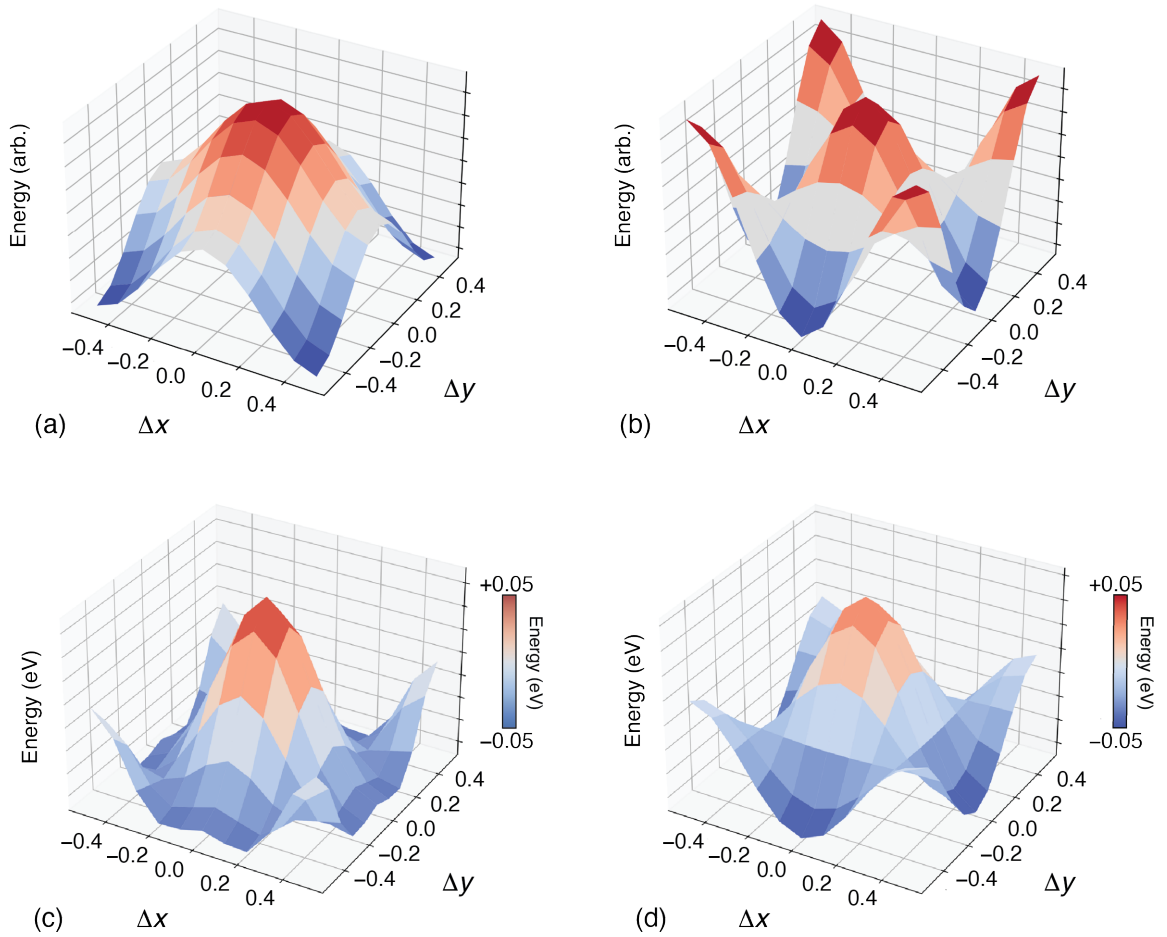

Figure 7.11: (a) The first Fourier component. This is to fit the central peak of the PES. (b) The second Fourier component. This fits the local minima. (c) The DFT-calculated PES. (d) The fit obtained using the two weighted Fourier components and a constant.

7.3.3 MC Simulations

With these DFT energy fits, we now have a pseudo-spin model that captures the effective interactions between the $Ni(CN)_2$ layers. An MC simulation can now be used to find the low-energy configurational state. There are two important considerations to keep in mind here. First, the DFT energy fits are a measure of the inter-layer interaction energy per unit area. The dimensions of the $Ni(CN)_2$ layers and their absolute total interaction energy are not known in a polycrystalline sample of $Ni(CN)_2$. Therefore, when running the MC simulation, one should not be concerned with the absolute magnitudes of J_{1a} and J_{1b}, but rather their ratios, which give a measure of the scale of the different interaction parameters. The second consideration when running an MC simulation is the temperature at which the simulation should be run at and whether the system is even under equilibrium conditions when it is formed. Here, a series of MC simulations were run at different J_{1a}/T_{eff} ratios and the overall magnitude was scaled to best match experiment. The relatively good match to experiment was taken as indicative that the $Ni(CN)_2$ was at or close to equilibrium when it was forming.

At the end of the MC simulation of chains of quarternions, each quaternion was converted back into its corresponding shifted layer of $Ni(CN)_2$. Anisotropic displacement parameters from Ref. 311 were used in the generated crystallographic information files (cifs). Their PXRD patterns could then be calculated. A series of these simulated PXRD patterns are shown in Fig. 7.12.

The best match to experiment occurred when the ratio $J_{1a}/T_{\text{eff}} = 56.7$. This optimal ratio is defined as α_{opt} and was used for the final averaged pattern (Fig. 7.13). Whilst the peaks that govern inter-layer spacing (002) and intra-layer distances (002) remain sharp, it is the mixed (hkl) peaks such as (011) and (112) that are most sensitive to

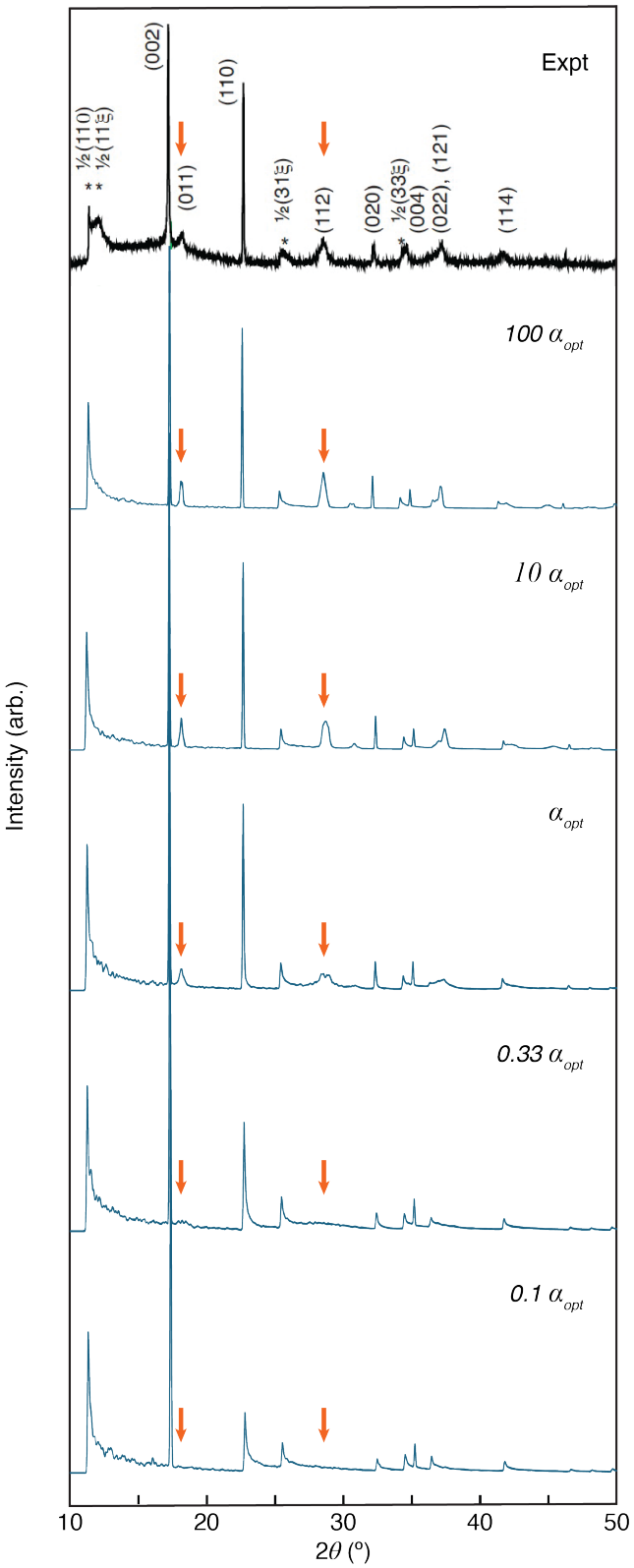

Figure 7.12: A series of simulated PXRD patterns using different magnitudes of α_{opt} for the continuous pseudo-spin nearest-neighbour model. The peaks of interest are highlighted with the orange arrows. The best match to experiment is when $J_{1a}/T_{\text{eff}} = \alpha_{\text{opt}} = 56.7$. The ratio between the interaction parameters J_{1a} and J_{1b} remain fixed throughout. This shows the sensitivity of the layer lability to the magnitude of the interaction parameters with respect to temperature. Increasing the temperature (and going down the plot) significantly broadens associated peaks such as the (011) and (112). The best match to experiment is when $J_{1a}/T_{\text{eff}} = 56.7$.

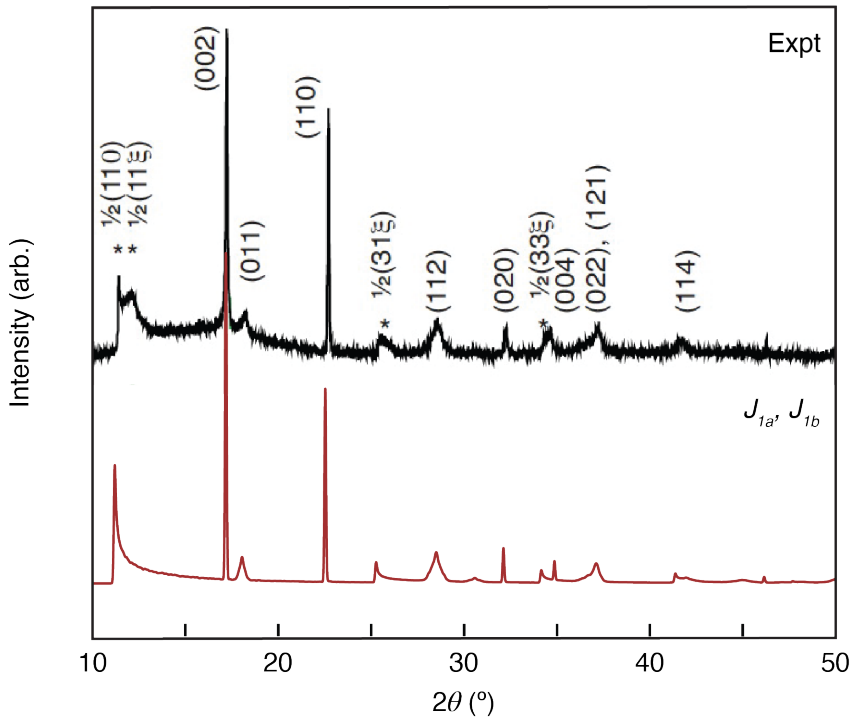

Figure 7.13: The simulated PXRD pattern (red) is compared to experimental PXRD (black). The simulated pattern is the average of 20 independent configurations obtained *via* the pseudo-spin MC outlined in the text. Anisotropic displacement parameters from Ref. 311 have also been added.

temperature. These peaks broaden significantly as temperature is increased before disappearing by $J_{1a}/T_{\text{eff}} = 0.567$. The good match in peak broadening indicates that a continuous model rather than a discrete Ising model is a good choice for modelling the stacking behaviour in $Ni(CN)_2$.

Once a most suitable J_{1a}/T_{eff} was picked, 20 independent MC simulations were run with the set of T_{eff}, J_{1a} and J_{1b}. Simulated PXRD patterns from the 20 independent configurations were averaged. The final result is shown in Fig. 7.13.

The number of peaks and many of the diffuse features match well with the powder diffraction data. A clear limitation arises for the shape of the diffuse peak at $2\theta = 12.5°$. In Ref. 311, this peak was shown to be particularly sensitive to next-nearest interactions.

Previous work used a 2nd layer correlation function, p, to describe this within the discrete model.[311] The function, p, gave the likelihood that the next-nearest neighbour layers would be of the same type (i.e., a short-range order parameter). The best match with experiment was shown to be at $p = 0.33$, indicating that the likelihood of finding unlike pairs at the next-nearest neighbour level ($A \cdots A'$) was about twice as likely as like pairs ($A \cdots A$). Previous work mentions that this slight preference may arise to prevent the same Ni^{2+} ion interacting with CN^- ions in different sheets.

7.3.4 Next-Nearest Neighbour Interactions

To account for these 2nd layer correlations, next-nearest neighbour interactions were added to the pseudo-spin model. Three layers were used to calculate the energy surface using DFT. The first two layers were arranged in a low energy configuration, whilst the third layer was allowed to move by 0.1 fractional coordinate increments in both Δx and Δy (Fig. 7.14 (a)). The same DFT parameters and box were used as for the two-layer case such that the nearest group of three layers was 26 Å away to minimise long range electrostatic effects.

Using the same Fourier components, the DFT energy surface was again parametrised, using the same least-squares fitting process with a three-point Jacobian. The effective next-nearest neighbour Hamiltonian is as follows:

$$\mathcal{H}_{nnn} = -J_{2a} \sum_{\langle\langle i,j \rangle\rangle} \mathbf{p}_i \cdot \mathbf{p}_j - J_{2b} \sum_{\langle\langle i,j \rangle\rangle} \mathbf{q}_i \cdot \mathbf{q}_j, \tag{7.13}$$

The parameters used are shown in Table 7.2 below. The best J_{2a}/J_{2b} ratio was of -0.125. The R^2 for the fit is 0.852. These Fourier components correspond to the expected preference for 'unlike' layers as next-nearest neighbours. We note that the absolute magnitudes are about an order of magnitude less than for the next-nearest neighbour

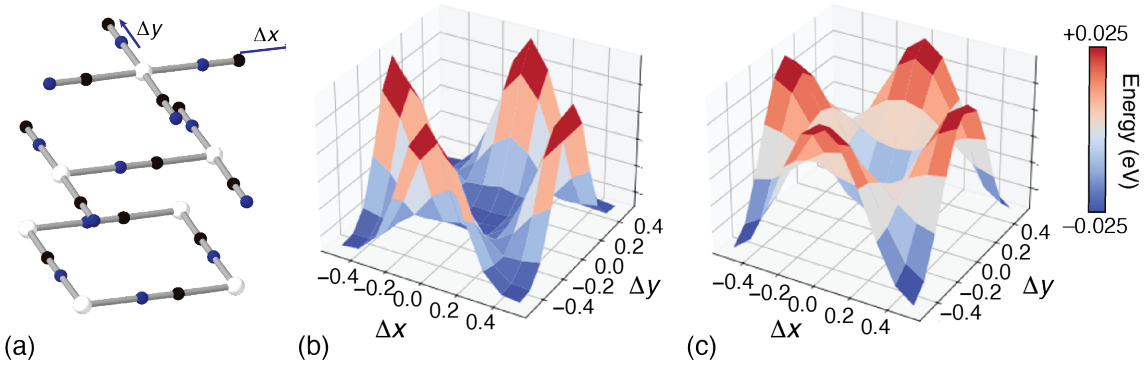

Figure 7.14: (a) Pictorial representation of the next-nearest neighbour layer shifts. (b) The PES calculated *via* DFT. (c) The fit using the two weighted Fourier components.

parameters, such that the stacking behaviour should not change in a fundamental sense.

Table 7.2: Parameter values for fit of next-nearest layer PES.

Parameters	J_{2a}	J_{2b}	a
eV	0.000824	−0.006554	−6765.497

MC simulations were run again at a series of magnitudes using the full Hamiltonian, including both nearest and next-nearest neighbour terms for 1000 quaternions (Fig. 7.15). Again, the degree of ordering and match to experiment are very sensitive to the overall magnitudes of the interaction parameters even if their ratios are fixed throughout. At high temperature, the general thermal disorder mimics that of the nearest-neighbour case, since the interaction parameters are outweighed by the thermal energy. Here, the best match was at a J_{1a}/T_{eff} ratio of 1.89 (α_{opt}), where the characteristic shoulder at 12.5° is well-replicated. This corresponds to the values at 300 K for the interaction parameters shown in Table 7.3.

Table 7.3: Exchange coupling constants used at 300 K

Parameter	J_{1a}	J_{1b}	J_{2a}	J_{2b}
(kJ mol^{-1})	4.71	8.49	0.95	−7.57

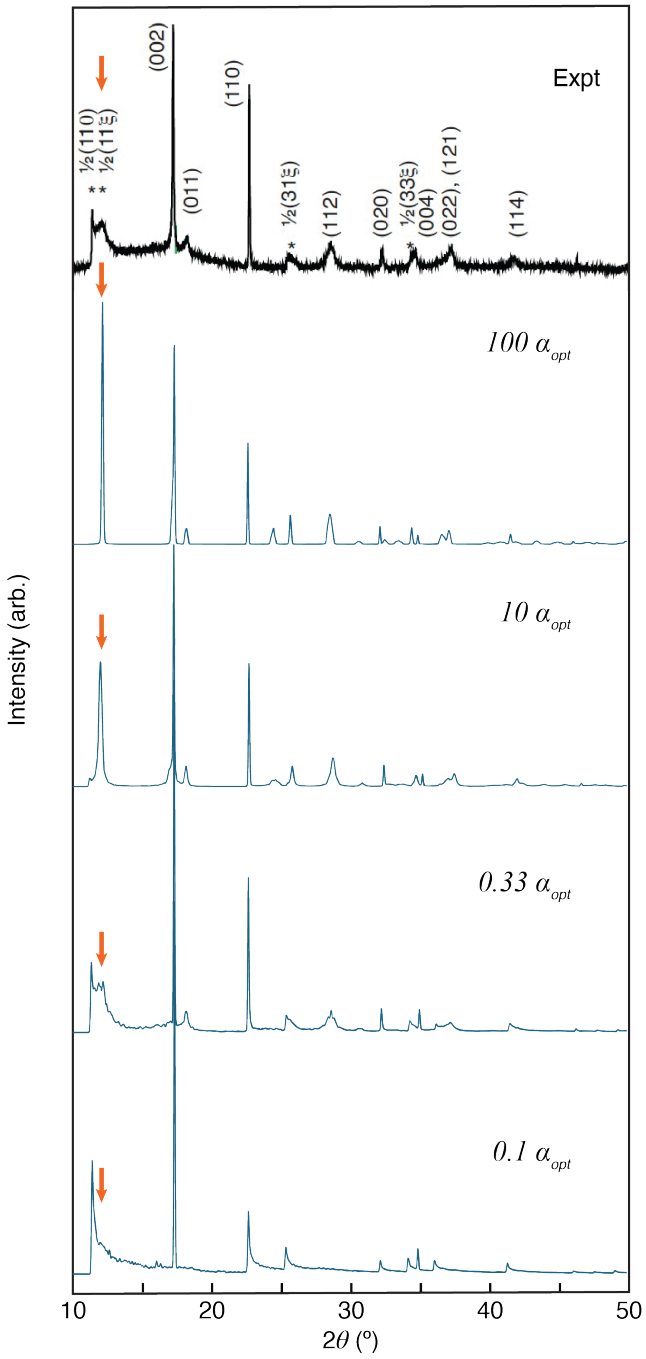

Figure 7.15: A series of simulated PXRD patterns using different magnitudes of J_{1a}/T_{eff} for the continuous pseudo-spin next-nearest neighbour model. The peak of interest is highlighted with the orange arrow. The best match to experiment is at $J_{1a}/T_{\text{eff}} = \alpha_{opt} = 1.89$ where the peak at 12.5° is well replicated. The ratio between the interaction parameters J_{1a} and J_{1b} remain fixed throughout. This shows the sensitivity of the layer shifts with respect to both the interaction parameters and temperature. Increasing the temperature (and going down the plot) significantly broadens associated peaks such as the (011) and (112).

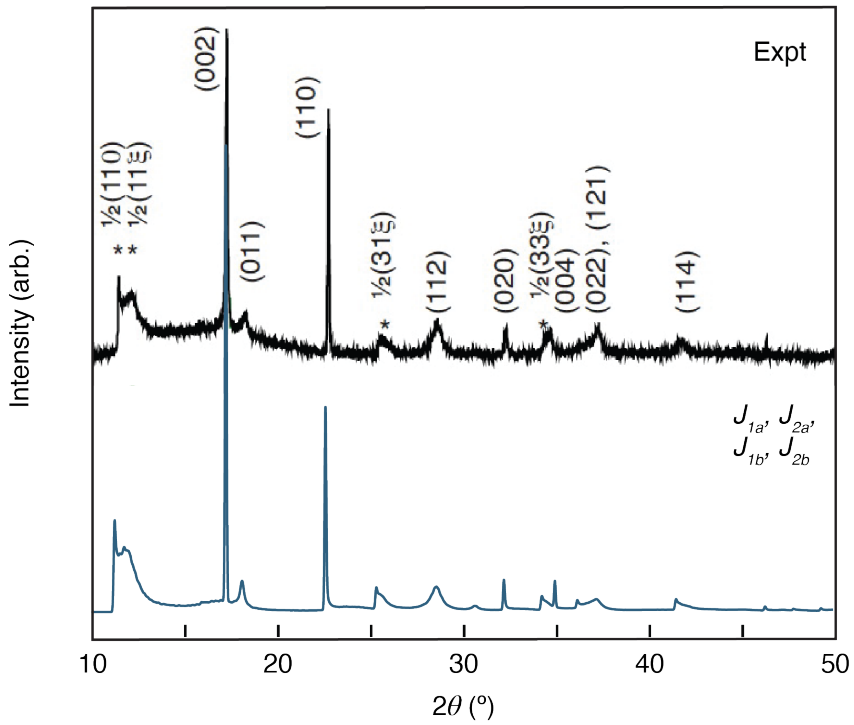

Figure 7.16: The simulated X-ray PXRD pattern including next-nearest neighbour interactions (blue) is compared to experiment (black). The simulated pattern is the average of 20 independent configurations obtained *via* the pseudo-spin MC outlined in the text. Anisotropic displacement parameters from Ref. 311 have also been added. Here, the peak at 12.5° is well-captured.

Using the best J_{1a}/T_{eff} ratio of 1.89, 20 independent configurations were run, decorated, and averaged. The final result is shown in Fig. 7.16. The peak at 12.5° is now well modelled. Indeed, the 2^{nd} layer correlation function, p, arrives at 0.34 – a very good match to the value determined empirically for the Ising model equivalent.

On the atomistic representation, it is interesting to note the concerted and wave-like character of the layer shifts (Fig. 7.17). The quaternions are in a helical state as observed for the continuous pseudo-spin models described earlier in the chapter when J_1 and J_2 are of similar magnitudes. This helical state corresponds to modest shifts between neighbouring layers. Effectively, as each layer is displaced, this has a domino effect on the displacement of its nearest and next-nearest-neighbours.

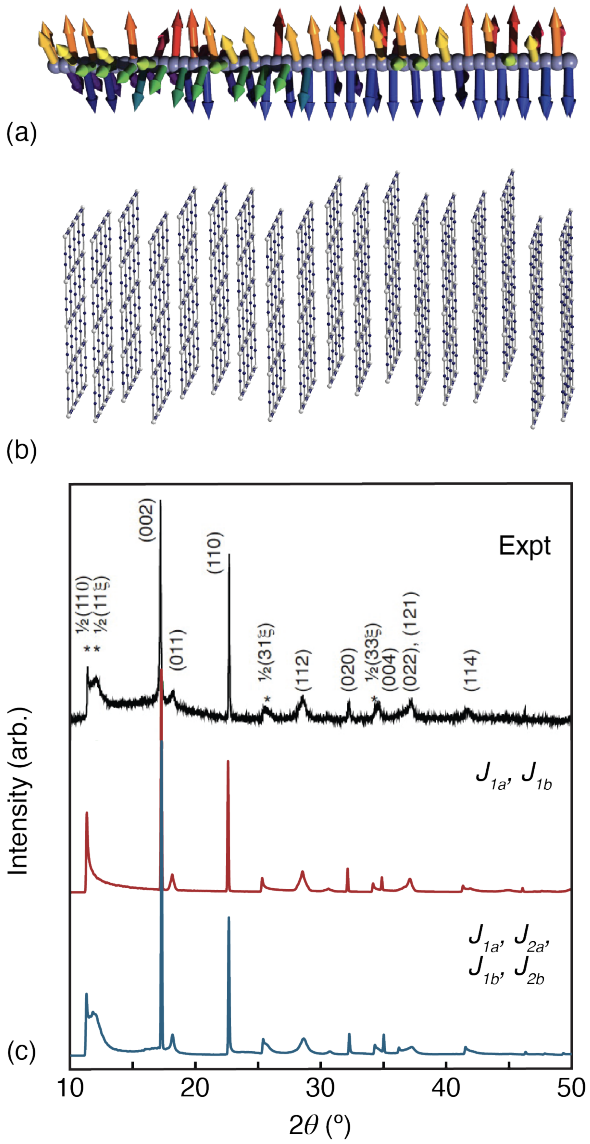

Figure 7.17: (a) A segment of a chain of quaternions in one of the final MC simulations, here represented by pairs of 2-D vectors. (b) The corresponding layer shifts of $Ni(CN)_2$ after decoration. (c) Comparison between experimental (black), nearest-neighbour (red), and next-nearest neighbour (blue) pseudo-spin simulated PXRD patterns.

Visually, this resembles frozen-in continuous sinusoidal waves propagating along the z-direction of $Ni(CN)_2$.

7.4 Outlook

The mapping of the layered structure of $Ni(CN)_2$ to 1-D quarternion chains opens up a series of possible research avenues. If the structure of $Ni(CN)_2$ is analogous to a 1-D chain of quaternions, could a similar parallel be drawn between their collective excitations? Quaternions can represent spin-$\frac{1}{2}$ particles. These can fractionalise and form two-spinon continua in their excitation spectra. The collective excitations of $Ni(CN)_2$ and its dynamics should be analogous. Perhaps the phonons in $Ni(CN)_2$ couple with the disordered stacking arrangement of the layers. Phonon broadening of modes along the z-direction could be related to the spinon continua seen in spin systems and may represent an interesting structural and chemical parallel to this quantum effect. In addition, this technique that uses both abstraction and pseudo-spin models could perhaps be applied more generally to other layered materials that exhibit disorder in their stacking behaviour. One could also use an RMC methodology to tune the effective interaction parameters to fit measured experimental data.

8
Conclusion

The original aims of this thesis were to tackle the dynamics and structural complexity of a range of systems *via* coarse-grained approaches. The low-energy dynamics of the cyanospinel family were shown to have a common quasi-RUM like optic mode at the L-point in reciprocal space involving displacements of the cation sublattice. DBP can be considered as a hybrid cristobalite, since its dynamics, TDS and phase transition are closely related to those of cristobalite. When reinterpreting the NTE behaviour of $Zn(CN)_2$ and $Cd(CN)_2$, we found a contrasting coarse-graining to so-called 'framework modes' was more effective than the RUM model. We showed that this 'framework modes' picture could be helpful more generally in abstracting the dynamics of framework materials. Lastly, the disordered layered structure of $Ni(CN)_2$ could be understood with an inter-layer potential where the effective interactions were between nearest and next-nearest layers. The wave-like layer arrangement of the ground state is indicative of the shallowness of the potential around the minima, such that small layer shifts are allowed. More broadly, the thesis has shown how coarse-graining can be effectively used to describe and select the important driving forces for different phenomena.

For each of these systems, there are several research directions. For the cyanospinels, the mixed $K_xRb_{2-x}Zn(CN)_4$ series is most exciting. These compositional-ice candidates would allow for detailed investigation in how correlated compositional disorder and low-energy lattice dynamics interact. Could specific short-range order arrangements scatter the low-energy optic mode or the acoustic phonons that are key for thermal

conductivity? For DBP, its description as a 'hybrid cristobalite' can be applied to the rest of the dimetal propionate family. The success of the hybrid perovskites lie in their compositional flexibility, structural diversity and low-energy dynamics. The dimetal propionate family shares several common features that could make it a success as well. The NTE behaviour of $Zn(CN)_2$ and $Cd(CN)_2$ can be probed further for the disordered cases. Whilst there have been shown to be minimal differences between the NTE behaviour of the fully ordered and disordered cases during MD simulations, it would be interesting to quantify the effect that cyanide ordering has on the phonon dispersion curves. The rapid development of ML potentials on disordered structures, should make the calculation of phonon dispersion curves on large, disordered supercells routine. The non-trivial interplay between short-range disorder and dynamics in real systems should become much more accessible, with DFT-like accuracy. In the same vein, the dynamics of $Ni(CN)_2$—and how its disordered layered structure interacts with particular phonon modes—should also be a rich avenue of future research. Lastly, the framework modes picture can be further developed. Immediate next steps of testing on a wider range of systems are not difficult. An iterative process of extracting from the TDS the elastic constants, deriving the acoustic component of the framework modes and then using this to further predict temperature-dependent properties is another possible future direction.

In a broader sense, the coarse-graining approach undertaken in this thesis should become more relevant than ever. The tremendous progress in computational power and experimental instruments has led to a greater ability in tackling ever more complex structures and problems. The increasing use of ML potentials with DFT-level accuracy should soon make nanoscale simulations and phonon calculations of

complex systems much more accessible.[313] Recent hybrid RMC techniques have shown the complementary nature and power of coupling scattering data with energetics.[314] Experimental techniques such as INS and TDS will therefore remain essential to scientific progress in this field. The advent of routine electron diffraction techniques is particularly exciting in using single crystal diffuse scattering approaches on a series of previously inaccessible systems. Amidst all these advances, coarse-grained approaches and the ability to rationalise cause and effect will remain crucial in materials design.

Crystallography has progressed greatly over the last one hundred years since Laue's first experiment. Crystal structure solutions have become routine, yet the picture, at least for the general crystallographer, remains predominantly static. Decoding the dynamics and disorder of systems and their interplay has tremendous potential. Precise phonon band engineering could have extraordinary repercussions. The future of this dynamic field is bright.

Bibliography

[1] C. Bailey, *The Greek Atomists and Epicurus*, Clarendon Press, p. 332 (1928)

[2] Lucretius, *Of the Nature of Things*, transl. William Ellery Leonard, J.M. Dent & Sons Ltd, II. 321–322 (1916)

[3] Lucretius, *De Rerum Natura*, II. 317–322.

[4] A. Einstein, *Ann. Phys* **327**, 180 (1907)

[5] P. Debye, *Ann. Phys.* **4**, 789 (1912)

[6] M. Von Laue, "Concerning the detection of X-ray interferences," Nobel Lecture (1920). Available at: `https://www.nobelprize.org/prizes/physics/1914/laue/lecture/`.

[7] P. Debye, *Ann. Phys* **348**, 49 (1913)

[8] I. Waller, *Z. Phys.* **17**, 398 (1923)

[9] I. Waller, *Theoretical Studies on the Interference and Dispersion Theory of X-rays*, Ph.D. thesis, Uppsala University (1925)

[10] M. T. Dove, *Structure and Dynamics: An Atomic View of Materials*, Oxford University Press (2003)

[11] M. Dove, *Introduction to Lattice Dynamics*, Cambridge University Press (1993)

[12] B. T. M. Willis and A. W. Pryor, *Thermal Vibrations in Crystallography*, Cambridge University Press (1975)

[13] J. D. Gale, *J. Chem. Soc., Faraday Trans.* **93**, 629 (1997)

[14] J. D. Gale, *J. Phys. Chem. B* **102**, 5423 (1998)

[15] E. Grüneisen, "Zustand des festen Körpers," In H. Geiger & K. Scheel (eds.), *Thermische Eigenschaften der Stoffe*, vol. X of *Handbuch der Physik*, 1–59, Springer (1926)

[16] M. Ducamp and F.-X. Coudert, *J. Phys. Chem. C* **125**, 15647–15658 (2021)

[17] M. T. Dove and H. Fang, *Rep. Prog. Phys.* **79**, 066503 (2016)

[18] R. Mittal, M. K. Gupta and S. L. Chaplot, *Prog. Mater. Sci.* **92**, 360–445 (2018)

[19] X. G. Zheng, H. Kubozono, H. Yamada, K. Kato, Y. Ishiwata and C. N. Xu, *Nat. Nanotechnol.* **3**, 724–726 (2008)

[20] M. Azuma, W.-T. Chen, H. Seki, M. Czapski, S. Olga, K. Oka, S. Ishiwata, M. Mizumaki, N. Kawamura, T. Watanuki, N. Ishimatsu, M. G. Tucker, J. P. Attfield and Y. Shimakawa, *Nat. Commun.* **2**, 347 (2011)

[21] T. H. K. Barron, *Phil. Mag.* **46**, 720–734 (1955)

[22] T. H. K. Barron, *Ann. Phys., NY* **1**, 77–90 (1957)

[23] G. D. Barrera, J. A. O. Bruno, T. H. K. Barron and N. L. Allan, *J. Phys.: Condens. Matter* **17**, R217–R252 (2005)

[24] D. Wendt, E. Bozin, J. Neuefeind, K. Page, W. Ku, L. Wang, B. Fultz, A. V. Tkachenko and I. A. Zaliznyak, *Sci. Adv.* **5**, eaay2748 (2019)

[25] M. T. Dove, J. Du, Z. Wei, D. A. Keen, M. G. Tucker and A. E. Phillips, *Phys. Rev. B* **102**, 094105 (2020)

[26] M. T. Dove, Z. Wei, A. E. Phillips, D. A. Keen and K. Refson, *APL Mater.* **11**, 041130 (2023)

[27] A. P. Giddy, M. T. Dove, G. S. Pawley and V. Heine, *Acta Crystallogr. A* **49**, 697–703 (1993)

[28] K. D. Hammonds, M. T. Dove, A. P. Giddy, V. Heine and B. Winkler, *Am. Mineral.* **81**, 1057–1079 (1996)

[29] A. L. Goodwin, *Phys. Rev. B* **74**, 134302 (2006)

[30] M. G. Tucker, M. T. Dove and D. A. Keen, *J. Phys.: Condens. Matter* **12**, L723–L730 (2000)

[31] M. G. Tucker, D. A. Keen and M. T. Dove, *Mineral. Mag.* **65**, 489–507 (2001)

[32] I. Swainson and M. T. Dove, *Phys. Rev. Lett.* **71**, 193–196 (1993)

[33] J. N. Grima, M. Bajada, S. Scerri, D. Attard, K. K. Dudek and R. Gatt, *Proc. R. Soc. A* **471**, 20150188 (2015)

[34] K. D. Hammonds, H. Deng, V. Heine and M. T. Dove, *Phys. Rev. Lett.* **78**, 3701–3704 (1997)

[35] K. D. Hammonds, V. Heine and M. T. Dove, *Phase Transit.* **61**, 155–172 (1997)

[36] K. D. Hammonds, V. Heine and M. T. Dove, *J. Phys. Chem. B* **102**, 1759–1767 (1998)

[37] L. Tan, V. Heine, G. Li and M. T. Dove, *Rep. Prog. Phys.* **87**, 126501 (2024)

[38] M. T. Dove, K. D. Hammonds, V. Heine, R. L. Withers, Y. Xiao and R. J. Kirkpatrick, *Phys. Chem. Miner.* **23**, 56–62 (1996)

[39] M. T. Dove, A. K. A. Pryde, V. Heine and K. D. Hammonds, *J. Phys.: Condens. Matter* **19**, 275209 (2007)

[40] V. Heine and P. R. L. Welche, *J. Am. Ceram. Soc.* **82**, 1793–1802 (1999)

[41] P. R. L. Welche, V. Heine and M. T. Dove, *Phys. Chem. Miner.* **26**, 63–77 (1998)

[42] C. W. Li, X. Tang, J. A. Muñoz, J. B. Keith, S. J. Tracy, D. L. Abernathy and B. Fultz, *Phys. Rev. Lett.* **107**, 195504 (2011)

[43] C. A. Occhialini, G. G. Guzmán-Verri, S. U. Handunkanda and J. N. Hancock, *Front. Chem.* **6**, 545 (2018)

[44] K. D. Hammonds, M. T. Dove, A. P. Giddy and V. Heine, *Am. Mineral.* **79**, 1207–1209 (1994)

[45] H. Fang, A. E. Phillips, M. T. Dove, M. G. Tucker and A. L. Goodwin, *Phys. Rev. B* **88**, 144103 (2013)

[46] W. Tiano, M. Dapiaggi and G. Artioli, *J. Appl. Crystallogr.* **36**, 1461–1463 (2003)

[47] M. Dapiaggi, W. Tiano, G. Artioli, A. Sanson and P. Fornasini, *Nucl. Instrum. Methods Phys. Res. B* **200**, 231–236 (2003)

[48] L. H. N. Rimmer, M. T. Dove, B. Winkler, D. J. Wilson, K. Refson and A. L. Goodwin, *Phys. Rev. B* **89**, 214115 (2014)

[49] K.-P. Bohnen, R. Heid, L. Pintschovius, A. Soon and C. Stampfl, *Phys. Rev. B* **80**, 134304 (2009)

[50] M. K. Gupta, R. Mittal, S. L. Chaplot and S. Rols, *J. Appl. Phys.* **115**, 093507 (2014)

[51] A. K. A. Pryde, K. D. Hammonds, M. T. Dove, V. Heine, J. D. Gale and M. C. Warren, *J. Phys.: Condens. Matter* **8**, 10973–10982 (1996)

[52] A. K. A. Pryde, K. D. Hammonds, M. T. Dove, V. Heine, J. D. Gale and M. C. Warren, *Phase Transit.* **61**, 141–153 (1997)

[53] A. K. A. Pryde, M. T. Dove and V. Heine, *J. Phys.: Condens. Matter* **10**, 8417–8428 (1998)

[54] L. H. N. Rimmer, K. Refson and M. T. Dove, *Phys. Chem. Chem. Phys.* **25**, 16753–16762 (2023)

[55] M. Baise, P. M. Maffettone, F. Trousselet, N. P. Funnell, F.-X. Coudert, and A. L. Goodwin, *Phys. Rev. Lett.* **120**, 265501 (2018)

[56] W. Cochran, *Phys. Rev. Lett.* **3**, 412–414 (1959)

[57] W. Cochran, *Adv. Phys.* **9**, 387–423 (1960)

[58] W. Cochran, *Adv. Phys.* **10**, 401–420 (1961)

[59] H. T. Stokes and D. M. Hatch, *Phase Transitions* **34**, 53–67 (1991)

[60] B. Berge, J. P. Bachheimer, G. Dolino, M. Vallade and C. M. E. Zeyen, *Ferroelectrics* **66**, 73–84 (1986)

[61] M. Vallade, B. Berge and G. Dolino, *J. Physique I* **2**, 1481–1495 (1992)

[62] F. S. Tautz, V. Heine, M. T. Dove and X. Chen, *Phys. Chem. Miner.* **18**, 326–336 (1991)

[63] K. D. Hammonds, A. Bosenick, M. T. Dove and V. Heine, *Am. Mineral.* **83**, 476–479 (1998)

[64] S. Simpson and M. S. Senn, *Chem. Mater.*, (in press) (2025)

[65] H. L. B. Boström, *CrystEngComm* **22**, 961–968 (2020)

[66] D. M. Hatch and S. Ghose, *Phys. Chem. Miner.* **17**, 554–562 (1991)

[67] D. R. Peacor, *Z. Kristallogr.* **138**, 274–298 (1973)

[68] W. Nieuwenkamp, *Z. Kristallogr.* **96**, 454–458 (1937)

[69] M. J. Sanders, M. Leslie and C. R. A. Catlow, *J. Chem. Soc., Chem. Commun.*, 1271–1273 (1984)

[70] S. A. Wells, M. T. Dove, M. G. Tucker and K. Trachenko, *J. Phys.: Condens. Matter* **14**, 4645–4657 (2002)

[71] J. D. Axe and G. Shirane, *Phys. Rev. B* **1**, 342–348 (1970)

[72] P. A. Fleury, J. F. Scott and J. M. Worlock, *Phys. Rev. Lett.* **21**, 16–19 (1968)

[73] S. U. Handunkanda, E. B. Curry, V. Voronov, A. H. Said, G. G. Guzmán-Verri, R. T. Brierley, P. B. Littlewood and J. N. Hancock, *Phys. Rev. B* **92**, 134101 (2015)

[74] T. J. B. Holland, E. C. R. Green and R. Powell, *J. Metamorph. Geol.* **40**, 587–600 (2021)

[75] D. C. Palmer, E. K. H. Salje and W. W. Schmahl, *Phys. Chem. Miner.* **16**, 714–719 (1989)

[76] L. Wiehl and S. Hausshühl, *Z. Kristallogr.* **156**, 117–126 (1981)

[77] D. A. Keen, *Cryst. Rev.*, **26**, 143–201 (2020)

[78] R. Xu, *X-ray Thermal Diffuse Scattering and its Studies of Lattice Dynamics*, DPhil thesis, University of Illinois (2010)

[79] M. Born, *Rep. Prog. Phys.* **9**, 294 (1942)

[80] K. Lonsdale, *Proc. Phys. Soc.* **54**, 314 (1942)

[81] J. C. Aston, *X-Ray Thermal Diffuse Scattering at High Pressures*, DPhil thesis, University of Edinburgh (2022)

[82] T. R. Welberry and T. Weber, *Crystallogr. Rev.* **22**, 2 (2015)

[83] A. Förster, S. Brandstetter, and C. Schulze-Briese, *Phil. Trans. R. Soc. A* **377**, 20180241 (2019)

[84] S. P. Meisburger, D. A. Case, and N. Ando, *Nat. Commun.* **11**, 1271 (2020)

[85] S. P. Meisburger, W. C. Thomas, M. B. Watkins, and N. Ando, *Chem. Rev.* **117**, 7615–7672 (2017)

[86] W. H. Zachariasen, *Nature* **145**, 1019 (1940)

[87] W. Friedrich, *Phys. Z.* **14**, 1082 (1913)

[88] G. D. Preston, *Proc. R. Soc. A.* **172**, 116 (1939)

[89] H. Faxén, *Z. Phys.* **17**, 266 (1923)

[90] J. Laval, *C. R. Acad. Sci.* **207**, 169 (1938)

[91] J. Laval, *C. R. Acad. Sci.* **208**, 1512 (1939)

[92] J. Laval, *Bull. Soc. Franç. Minér.* **64**, 1 (1941)

[93] P. Olmer, *Acta Cryst.* **1**, 57 (1948)

[94] H. Curien, *Acta Cryst.* **5**, 393 (1952)

[95] E. H. Jacobsen, *Phys. Rev.* **97**, 654 (1955)

[96] R. E. Joynson, *Phys. Rev.* **94**, 851 (1954)

[97] E. Sándor and W. A. Wooster, *Acta Cryst.* **13**, 339 (1960)

[98] S. C. Prasad and W. A. Wooster, *Acta Cryst.* **8**, 506 (1955)

[99] H. Cole, *J. Appl. Phys.* **24**, 482 (1953)

[100] N. Boccara, *C. R. Hebd. Seances Acad. Sci.* **250**, 1025 (1960)

[101] E. Prince and W. A. Wooster, *Acta Cryst.* **4**, 191 (1951)

[102] DECTRIS Ltd., "Technical Specifications: EIGER R 1M Detector Systems," Document Version 1.3.8 (2018). Available at: `https://www.dectris.com/en/support/manuals-docs/eiger-r-for-laboratory/eiger-r-1m/`

[103] Z. Wu, H. Hong, R. Aburano, P. Zschack, P. Jemian, J. Tischler, H. Chen, D.-A. Luh, and T.-C. Chiang, *Phys. Rev. B* **59**, 3283 (1999)

[104] M. Holt, P. Czoschke, H. Hong, P. Zschack, H. K. Birnbaum, and T. C. Chiang, *Phys. Rev. B* **66**, 064303 (2002)

[105] B. Wehinger, A. Bosak, H. T. Dang, P. T. Jochym, J. Ła.zewski, M. Krisch, P. Piekarz, and K. Parlinski, *J. Phys.: Condens. Matter* **25**, 275401 (2013)

[106] B. Wehinger, A. Bosak, G. Piccolboni, K. Refson, D. Chernyshov, A. Ivanov, A. Rumiantsev, and M. Krisch, *J. Phys.: Condens. Matter* **26**, 115401 (2014)

[107] B. Wehinger, D. Chernyshov, M. Krisch, S. Bulat, V. Ezhov, and A. Bosak, *J. Phys.: Condens. Matter* **26**, 265401 (2014)

[108] B. Wehinger, A. Bosak, P. T. Jochym, J. Ła.zewski, P. Piekarz, and K. Parlinski, *J. Phys.: Condens. Matter* **27**, 305401 (2015)

[109] E. M. Schmidt, S. Thomas, J. M. Bulled, A. Minelli, and A. L. Goodwin, *Acta Crystallogr. Sect. B* **78**, 385 (2022)

[110] B. Wehinger, A. Bosak, and P. T. Jochym, *Phys. Rev. B* **93**, 014303 (2016)

[111] B. Wehinger, A. Mirone, M. Krisch, and A. Bosak, *Phys. Rev. Lett.* **118**, 035502 (2017)

[112] J. Büscher, A. Mirone, M. Stękiel, D. Spahr, W. Morgenroth, E. Haussühl, V. Milman, A. Bosak, O. Ivashko, M. von Zimmermann, A.-C. Dippel, and B. Winkler, *J. Appl. Crystallogr.* **54**, 287 (2021)

[113] A. Mirone and B. Wehinger, *AB2TDS – An Open Source Package for Calculating Lattice Dynamics Properties*, (2013). Available at: `http://ftp.esrf.fr/scisoft/AB2TDS/Introduction.html`

[114] A. Mirone and B. Wehinger, *TDS2EL2 – An Open Source Package for Quantitative and Model-Free Analysis of Thermal Diffuse X-ray Scattering from Single Crystals*, (2017). Available at: `http://ftp.esrf.eu/scisoft/TDS2EL/index.html`

[115] S. J. Clark, M. D. Segall, C. J. Pickard, P. J. Hasnip, M. J. Probert, K. Refson and M. C. Payne, *Z. Kristallogr.* **220**, 567–570 (2005)

[116] K. Refson, S. J. Clark and P. R. Tulip, *Phys. Rev. B* **73**, 155114 (2006)

[117] A. Togo, L. Chaput, T. Tadano and I. Tanaka, *J. Phys.: Condens. Matter* **35**, 353001 (2023)

[118] A. Togo, *J. Phys. Soc. Jpn.* **92**, 012001 (2023)

[119] T. Kamencek, S. Wieser, H. Kojima, N. Bedoya-Martínez, J. P. Dürholt, R. Schmid, and E. Zojer, *J. Chem. Theory Comput.* **16**, 2716–2735 (2020)

[120] X. Gonze and C. Lee, *Phys. Rev. B* **55**, 10355 (1997)

[121] J. A. M. Paddison, *Acta Crystallogr. A* **75**, 14–24 (2019)

[122] R. Xu and T. C. Chiang, *Z. Kristallogr. Krist.* **220**, 1009 (2005)

[123] M. D. Le, G. F. Reiter, et al., *Nucl. Instrum. Methods Phys. Res. A* **1056**, 168646 (2023)

[124] O. Arnold, J. Zikovsky, et al. *Nucl. Instrum. Methods Phys. Res. A* **764**, 156–166 (2014)

[125] Mantid Project, Mantid: Manipulation and Analysis Toolkit for Instrument Data (2013), http://dx.doi.org/10.5286/SOFTWARE/MANTID.

[126] R. L. Fair, A. J. Jackson, D. J. Voneshen, D. B. Jochym, M. D. Le, K. Refson and T. G. Perring, *J. Appl. Crystallogr.* **55**, 1689–1700 (2022)

[127] R. L. Fair and A. J. Jackson, Euphonic: Phonon and inelastic neutron scattering simulation, https://euphonic.readthedocs.io.

[128] A. R. Leach, *Molecular modelling: principles and applications*, Pearson Education (2001)

[129] P. Hohenberg and W. Kohn, *Phys. Rev.* **136**, B864 (1964)

[130] W. Kohn and L. J. Sham, *Phys. Rev.* **140**, A1133 (1965)

[131] D. C. Langreth and M. J. Mehl, *Phys. Rev. B* **28**, 1809 (1983)

[132] J. Sun, A. Ruzsinszky, and J. P. Perdew, *Phys. Rev. Lett.* **115**, 036402 (2015)

[133] J. P. Perdew, A. Ruzsinszky, G. I. Csonka, O. A. Vydrov, G. E. Scuseria, L. A. Constantin, X. Zhou and K. Burke, *Phys. Rev. Lett.* **100**, 136406 (2008)

[134] A. P. Bartók and J. R. Yates, *J. Chem. Phys.* **150**, 161101 (2019)

[135] B. G. Pfrommer, M. Cote, S. G. Louie and M. L. Cohen, *J. Comput. Phys.* **131**, 233–240 (1997)

[136] P. P. Ewald, *Ann. Phys.* **369**, 253 (1921)

[137] A. Galántai, *J. Comput. Appl. Math.* **124**, 25–44 (2000)

[138] M. E. J. Newman and G. T. Barkema, *Monte Carlo Methods in Statistical Physics*, Oxford University Press (1999)

[139] D. A. Keen and A. L. Goodwin, *Nature* **521**, 303–309 (2015)

[140] S. Ehrling, E. M. Reynolds, V. Bon, I. Senkovska, T. E. Gorelik, J. D. Evans, M. Rauche, M. Mendt, M. S. Weiss, A. Pöppl, E. Brunner, U. Kaiser, A. L. Goodwin, and S. Kaskel, *Nat. Chem.* **13**, 568–574 (2021)

[141] E. G. Meekel, E. M. Schmidt, L. J. Cameron, A. D. Dharma, H. J. Windsor, S. G. Duyker, A. Minelli, T. Pope, G. O. Lepore, B. Slater, C. J. Kepert, and A. L. Goodwin, *Science* **379**, 357–361 (2023)

[142] A. A. Markov, *Dynamic Probabilistic Systems*, John Wiley and Sons (1971)

[143] R. G. Melko and B. C. den Hertog, *Phys. Rev. Lett.* **87**, 067203 (2001)

[144] A. P. Thompson, S. J. Plimpton, et al. *Comput. Phys. Commun.* **271**, 108171 (2022)

[145] R. G. Dickinson, *J. Am. Chem. Soc.* **44**, 774–784 (1922)

[146] A. Sequeira and R. Chidambaram, *Acta Crystallogr.* **20**, 910–915 (1966)

[147] B. Ziegler and D. Babel, *Z. Naturforsch. B* **46**, 47–49 (1991)

[148] L. H. Jones, *Spectrochim. Acta* **17**, 188–200 (1961)

[149] L. A. Woodward and H. F. Owen, *J. Chem. Soc.* 1055–1059 (1959)

[150] L. H. Jones and B. I. Swanson, *J. Chem. Phys.* **63**, 5401–5411 (1975)

[151] M. Werker and U. Ruschewitz, *Z. Naturforsch. B* **74**, 781–786 (2019)

[152] L. D. C. Bok and J. G. Leipoldt, *Z. Anorg. Allg. Chem.* **344**, 86 (1966)

[153] P. N. Gerlach and B. M. Powell, *J. Chem. Phys.* **85**, 6004–6009 (1986)

[154] S. Hausshühl, D. Bunthoff and W. Michaelis, *Solid State Commun.* **34**, 765–767 (1980)

[155] V. V. Ivanov, N. V. Paschenko, P. B. Senyushkin and V. M. Talanov, *J. Struct. Chem.* **35**, 608–612 (1994)

[156] R. Ikeda, D. Nakamura and M. Kubo, *J. Phys. Chem.* **72**, 2982–2985 (1968)

[157] S. Saruwatari, R. Ikeda, D. Nakamura and M. Kubo, *J. Magn. Reson.* **9**, 503–509 (1973)

[158] S. Hausshühl, *Acta Crystallogr. A* **32**, 160–162 (1976)

[159] W. Krasser and S. Hausshühl, *Solid State Commun.* **20**, 191–193 (1976)

[160] E. Hellner, H. Ahsbahs, G. Dehnicke and K. Dehnicke, *Ber. Bunsenges. Phys. Chem.* **77**, 266–272 (1973)

[161] H. Ahsbahs, *Z. Kristallogr.* **149**, 151–152 (1979)

[162] D. Adams, M. Gerrard and P. Hatton, *Solid State Commun.* **39**, 229–232 (1981)

[163] H. T. Stokes, D. M. Hatch and B. J. Campbell, ISODISTORT, ISOTROPY Software Suite, iso.byu.edu.

[164] B. J. Campbell, H. T. Stokes, D. E. Tanner and D. M. Hatch, *J. Appl. Crystallogr.* **39**, 607–614 (2006)

[165] B. M. Powell and P. N. Gerlach, *Phys. Rev. B* **40**, 2426–2431 (1989)

[166] K. H. Schmidt, *Spectrochim. Acta* **33A**, 369–376 (1977)

[167] Y. Morioka, I. Nakagawa and T. Shimanouchi, *Spectrochim. Acta* **30A**, 479 (1974)

[168] D. M. Adams and R. E. Christopher, *Inorg. Chem.* **12**, 1609 (1973)

[169] L. H. Jones, *Inorg. Chem.* **13**, 2289 (1974)

[170] A. G. Sharpe, *The Chemistry of Cyano Complexes of the Transition Metals*, Academic Press, London, England (1976)

[171] A. Sequeira, *Acta Crystallogr.* **18**, 291–292 (1965)

[172] P. Klüfers, H. Fuess, S. Haussühl, *Z. Kristallogr.* **156**, 255–263 (1981)

[173] A. A. Coelho, J. S. O. Evans, I. R. Evans, A. Kern and S. Parsons, *Powder Diffr.* **26**, S22–S25 (2011)

[174] H. J. Monkhorst and J. D. Pack, *Phys. Rev. B* **13**, 5188–5192 (1976)

[175] S. T. Bramwell and M. J. Harris, *J. Phys.: Condens. Matter* **10**, L215–L220 (1998)

[176] T. Fennell, P. P. Deen, A. R. Wildes, K. Schmalzl, D. Prabhakaran, A. T. Boothroyd, R. J. Aldus, D. F. McMorrow and S. T. Bramwell, *Nat. Phys.* **15**, 60–64 (2019)

[177] P. W. Anderson, *Phys. Rev.* **102**, 1008–1013 (1956)

[178] M. J. Whitaker and C. Greaves, *J. Solid State Chem.* **215**, 171–176 (2014)

[179] A. Simonov and A. L. Goodwin, *Nat. Rev. Chem.* **4**, 657–675 (2020)

[180] K. Stadnicka and A. M. Glazer, *Acta Crystallogr. B* **40**, 139–145 (1984)

[181] K. Aizu, *J. Phys. Soc. Jpn.* **27**, 387–396 (1969)

[182] A. Sawada, Y. Ishibashi and Y. Takagi, *J. Phys. Soc. Jpn.* **43**, 195–203 (1977)

[183] A. M. Glazer, K. Stadnicka and S. Singh, *J. Phys. C: Solid State Phys.* **14**, 5011–5029 (1981)

[184] B. T. Matthias and J. P. Remeika, *Phys. Rev.* **107**, 1727–1728 (1957)

[185] K. Stadnicka and A. M. Glazer, *Acta Crystallogr. B* **36**, 2977–2981 (1980)

[186] S. Seki, M. Momotani and K. Nakatsu, *J. Chem. Phys.* **19**, 1061–1062 (1951)

[187] S. Seki, M. Momotani, K. Nakatsu and T. Oshima, *Bull. Chem. Soc. Jpn.* **28**, 411–416 (1955)

[188] N. Nakamura, H. Suga, H. Chihara and S. Seki, *Bull. Chem. Soc. Jpn.* **41**, 291–296 (1968)

[189] H. Kameyama, Y. Ishibashi and Y. Takagi, *J. Phys. Soc. Jpn.* **38**, 1703–1707 (1975)

[190] K. Gesi and K. Ozawa, *J. Phys. Soc. Jpn.* **38**, 467–470 (1975)

[191] A. Sawada, T. Kikugawa and Y. Ishibashi, *J. Phys. Soc. Jpn.* **46**, 871–875 (1979)

[192] A. Avramenko, *Barocaloric Effects in Barium-Dicalcium Organic Salts*, Ph.D. thesis, University of Cambridge (2019)

[193] A. Fitz, *Ber. Dtsch. Chem. Ges.* **13**, 1312–1316 (1880)

[194] L. P. Biefeld and P. M. Harris, *J. Am. Chem. Soc.* **57**, 396–399 (1935)

[195] I. Nitta and T. Watanabe, *Sci. Pap. Inst. Phys. Chem. Res. (Tokyo)* **26**, 164–172 (1935)

[196] S. Singh and A. M. Glazer, *Acta Crystallogr. A* **37**, 804–808 (1981)

[197] T. N. Sairam and S. V. Bhat, *Phase Transit.* **54**, 227–233 (1995)

[198] T. R. Welberry, *Acta Crystallogr. B* **38**, 1921–1927 (1982)

[199] A. F. Wright and A. J. Leadbetter, *Philos. Mag.* **31**, 1391–1401 (1975)

[200] I. P. Swainson and M. T. Dove, *J. Phys.: Condens. Matter* **7**, 1771–1788 (1995)

[201] M. G. Tucker, M. P. Squires, M. T. Dove and D. A. Keen, *J. Phys.: Condens. Matter* **13**, 403–423 (2001)

[202] S.V. Bhat, V. Dhar and R. Srinivasan, *J. Phys. Soc. Jpn.* **50**, 2312–2317 (1981)

[203] S.V. Bhat, V. Dhar and R. Srinivasan, *Indian J. Pure Appl. Phys.* **21**, 516–520 (1983)

[204] G. L. Hua, T. R. Welberry, R. L. Withers and J. G. Thompson, *J. Appl. Crystallogr.* **21**, 458–465 (1988)

[205] L. C. Erhard, J. Rohrer, K. Albe and V. L. Deringer, *npj Comput. Mater.* **8**, 90 (2022)

[206] M. Parrinello and A. Rahman, *J. Appl. Phys.* **52**, 7182–7190 (1981)

[207] D. E. Damby, E. W. Llewellin, C. J. Horwell, B. J. Williamson, J. Najorka, G. Cressey and M. Carpenter, *J. Appl. Crystallogr.* **47**, 1205–1215 (2014)

[208] A. J. Leadbetter and A. F. Wright, *Philos. Mag.* **33**, 105–112 (1976)

[209] M. A. Mosesman and K. S. Pitzer, *J. Am. Chem. Soc.* **63**, 2348–2356 (1941)

[210] R. B. Sosman, *The Phases of Silica* (Rutgers University Press, New Brunswick, 1965)

[211] W. W. Schmahl, I. P. Swainson, M. T. Dove and A. Graeme-Barber, *Z. Kristallogr.* **201**, 125–145 (1992)

[212] I. P. Swainson, M. T. Dove and D. C. Palmer, *Phys. Chem. Miner.* **30**, 353–365 (2003)

[213] D. R. Spearing, I. Farnan and J. F. Stebbins, *Phys. Chem. Miner.* **19**, 307–321 (1992)

[214] C. S. Sundaram, K. Ganesan, J. Ramakrishna, K. Chandrasekhar and V. S. S. Sastry, *Phase Transit.* **5**, 169–186 (1985)

[215] W. A. Dollase, *Z. Kristallogr.* **121**, 369–377 (1965)

[216] E. Shugam and H. Zhdanov, *Acta Physicochim. URSS* **20**, 247–252 (1945)

[217] B. F. Hoskins and R. Robson, *J. Am. Chem. Soc.* **112**, 1546–1554 (1990)

[218] C. S. Coates, R. A. Ewings, S. G. MacLeod, N. P. Funnell, E. E. McCabe, M. G. Tucker, J. A. M. Paddison and A. L. Goodwin, *Nat. Commun.* **12**, 2272 (2021)

[219] D. J. Williams, D. E. Partin, F. J. Lincoln, J. Kouvetakis and M. O'Keefe, *J. Solid State Chem.* **134**, 164–169 (1997)

[220] A. L. Goodwin and C. J. Kepert, *Phys. Rev. B* **71**, 140301(R) (2005)

[221] K. W. Chapman, P. J. Chupas and C. J. Kepert, *J. Am. Chem. Soc.* **127**, 15630–15636 (2005)

[222] J. W. Zwanziger, *Phys. Rev. B* **76**, 052102 (2007)

[223] T. A. Mary, J. S. O. Evans, T. Vogt and A. W. Sleight, *Science* **272**, 90–92 (1996)

[224] J. Bulled, *Disorder–Property Relationships in Magnetic and Pseudospin Framework Materials*, D.Phil. thesis, University of Oxford (2023)

[225] F.-X. Coudert, *Chem. Mater.* **27**, 1905–1914 (2015)

[226] C. Pantea, I. G. Spulber, A. Migliori, J. B. Betts, Y. Zhao, L. L. Daemen, H. K. Kim, R. A. Fisher, J. L. Smith, H. H. Hsieh and B. J. Gibbons, *Phys. Rev. B* **73**, 214118 (2006)

[227] N. F. Dow, and B. W. Rosen, Contract Report NASA-CR-1324, *NASA* (1969)

[228] I. Sideridou, D. S. Achilias, E. Kyrikou, *Biomaterials* **25**, 3087–3097 (2004)

[229] T. Legero, T. Kessler, and U. Sterr, *J. Opt. Soc. Am. B* **27**, 914–919 (2010)

[230] K. Takenaka, *Sci. Technol. Adv. Mater.* **13**, 013001 (2012)

[231] C. P. Romao, K. J. Miller, C. A. Whitman, M. A. White and B. A. Marinkovic, Negative Thermal Expansion (Thermomiotic) Materials, in *Comprehensive Inorganic Chemistry II (Second Edition)*, J. Reedijk and K. Poeppelmeier, Elsevier, pp. 127–151, (2013)

[232] J. Chen, L. Hu, J. Deng and X. Xing, *Chem. Soc. Rev.* **44**, 3522–3567 (2015)

[233] S. J. Hibble, A. M. Chippindale, E. J. Bilbé, E. Marelli, L. H. N. Rimmer, A. C. Hannon, M. G. Tucker, M. T. Dove and A. L. Goodwin, *J. Am. Chem. Soc.* **135**, 16478–16488 (2013)

[234] H. Fang, M. T. Dove, L. H. N. Rimmer, and A. J. Misquitta, *Phys. Rev. B* **88**, 104306 (2013)

[235] J. Wang, Q. Gao, A. Sanson, Q. Sun and E. Liang, *Inorg. Chem.* **61**, 13239–13246 (2022)

[236] Y.-N. Sun, L. Wang and C. Wang, *Dalton Trans.* **54**, 764–773 (2025)

[237] D. F. Gibbons, *Phys. Rev.* **112**, 136–140 (1958)

[238] J. S. Shah and M. E. Straumanis, *Solid State Commun.* **10**, 159–162 (1972)

[239] C. H. Xu, C. Z. Wang, C. T. Chan and K. M. Ho, *Phys. Rev. B* **43**, 5024–5027 (1991)

[240] H. Adenstedt, *Ann. Phys.* **418**, 69–96 (1936)

[241] K. Yang, J. Xiao, J. Luo, S. Li, S. Wei, and H. Deng, *New J. Phys.* **21**, 123015 (2019)

[242] P. Hohenberg and W. Kohn, *Phys. Rev.* **136**, B864–B871 (1964)

[243] W. Kohn and L. J. Sham, *Phys. Rev.* **140**, A1133–A1138 (1965)

[244] D. R. Hamann, *Phys. Rev. B* **88**, 085117 (2013)

[245] M. C. Payne, M. P. Teter, D. C. Allan, T. A. Arias and J. D. Joannopoulos, *Rev. Mod. Phys.* **64**, 1045–1097 (1992)

[246] S. Baroni, P. Giannozzi and A. Testa, *Phys. Rev. Lett.* **58**, 1861–1864 (1987)

[247] C. S. Coates, J. W. Makepeace, A. G. Seel, M. Baise, B. Slater and A. L. Goodwin, *Dalton Trans.* **47**, 7263–7271 (2018)

[248] R. I. Smith, S. Hull, M. G. Tucker, H. Y. Playford, D. J. McPhail, S. P. Waller and S. T. Norberg, *Rev. Sci. Instrum.* **90**, 115101 (2019)

[249] I.-K. Jeong, T. Proffen, F. Mohiuddin-Jacobs and S. J. L. Billinge, *J. Phys. Chem. A* **103**, 921–924 (1999)

[250] I.-K. Jeong, R. H. Heffner, M. J. Graf and S. J. L. Billinge, *Phys. Rev. B* **67**, 104301 (2003)

[251] A. L. Goodwin, C. J. Kepert, *Phys. Rev. B* **71**, 140301 (2005)

[252] M. G. Tucker, D. A. Keen, M. T. Dove, A. L. Goodwin and Q. Hui, *J. Phys.: Condens. Matter* **19**, 335218 (2007)

[253] A. Sanson, F. Rocca, G. Dalba, P. Fornasini, R. Grisenti, M. Dapiaggi and G. Artoli, *Phys. Rev. B* **73**, 214305 (2006)

[254] K. W. Chapman, M. Hagen, C. J. Kepert and P. Manuel, *Physica B* **385-386**, 60–62 (2006)

[255] P. Ding, E. J. Liang, Y. Jia and Z. Y. Du, *J. Phys.: Condens. Matter* **20**, 275224 (2008)

[256] C. S. Coates, J. M. Bulled, E. M. Schmidt, C. L. Hobday, R. A. Ewings, M. G. Tucker, S. E. Dutton and A. L. Goodwin, *arXiv*:2302.09963 (2023)

[257] I. E. Collings, M. G. Tucker, D. A. Keen, L. R. Louca, A. L. Goodwin, J. A. M. Paddison, T. D. Bennett and A. K. Cheetham, *J. Am. Chem. Soc.* **135**, 7610–7619 (2013)

[258] M. T. Dove, *Phil. Trans. R. Soc. A* **377**, 20180222 (2019)

[259] N. Lock, Y. Wu, M. Christensen, L. J. Cameron, V. K. Peterson, A. J. Bridgeman, C. J. Kepert, B. B. Iversen, *J. Phys. Chem. C* **114**, 16181–16190 (2010)

[260] W. Zhou, H. Wu, T. Yildirim, J. R. Simpson, A. R. H. Walker, *Phys. Rev. B* **78**, 054114 (2008)

[261] N. Lock, M. Christensen, Y. Wu, V. K. Peterson, M. K. Thomsen, R. O. Piltz, A. J. Ramirez-Cuesta, G. J. McIntyre, K. Noren, R. Kutteh, C. J. Kepert, G. J. Kearley, B. B. Iversen, *Dalton Trans.* **42**, 1996–2005 (2013)

[262] A. Berlie and H. Cavaye, *Phys. Chem. Chem. Phys.* **23**, 2899–2907 (2021)

[263] J.-W. Cao, J.-Y. Chen, X.-L Qin, X.-L. Zhu, L. Jiang, Y. Gu, X.-H Yu, P. Zhang, *Molecules* **24**, 3135 (2019)

[264] T. Kamencek, N. Bedoya-Martínez, and E. Zojer, *Phys. Rev. Mater.* **3**, 116003 (2019)

[265] T. C. Nicholas, CHIC. Available at: `https://github.com/tcnicholas/chic`

[266] T. C. Nicholas, A. L. Goodwin, V. L. Deringer, *Chem. Sci.* **11**, 12580–12588 (2020)

[267] H. Li, M. Eddaoudi, M. O'Keeffe, and O. M. Yaghi, *Nature* **402**, 276–279 (1999)

[268] E. G. Meekel and A. L. Goodwin, *CrystEngComm* **23**, 2915–2922 (2021)

[269] E. G. Meekel, P. Partridge, R. A. I. Paraoan, J. J. B. Levinsky, B. Slater, C. L. Hobday and A. L. Goodwin, *Nat. Mater.* **23**, 1245–1251 (2024)

[270] G. C. Xu, X. M. Ma, L. Zhang, Z. M. Wang, S. Gao, *J. Am. Chem. Soc.* **132**, 9588–9590 (2010)

[271] G.-C. Xu, W. Zhang, X.-M. Ma, Y.-H. Chen, L. Zhang, H.-L. Cai, Z.-M. Wang, R.-G. Xiong, S. Gao, *J. Am. Chem. Soc.* **133**, 14948–14951 (2011)

[272] W. Li, J. S. G. Gutzler, M. R. Probert, J. C. P. Gabriel, R. S. Forgan, C. A. Murray, S. J. Teat, S. K. Callear, G. S. MacLeod, G. J. McIntyre, C. M. Robertson, J. A. K. Howard and A. K. Cheetham, *J. Am. Chem. Soc.* **134**, 11940–11943 (2012)

[273] J. M. M. Lawler, P. Manuel, A. L. Thompson, P. J. Saines, *Dalton Trans.* **44**, 11613–11618 (2015)

[274] T. J. Hitchings, H. M. Wickins, L. G. Burley, S. C. Capelli, F. Demmel, A. E. Phillips, P. Hodgkinson, P. J. Saines, *Chin. J. Chem.* **43**, 1190-1198 (2025)

[275] A. L. Goodwin, D. A. Keen, M. G. Tucker, *Proc. Natl. Acad. Sci. U.S.A.* **105**, 18708–18713 (2008)

[276] M. Bhogra, A. L. Goodwin, A. K. Cheetham and U. V. Waghmare, *Phys. Rev. B* **108**, 214106 (2023)

[277] P. Bak, *Rep. Prog. Phys.* **45**, 587–629 (1982)

[278] W. Selke, *Phys. Rep.* **170**, 213–264 (1988)

[279] E. Ising, *Z. Phys.* **31**, 253–258 (1925)

[280] D. G. Petti and A. H. Cottrell, in *Electron Theory in Alloy Design*, pp. 164–166, The Institute of Materials, London (1992)

[281] M. Ruffino, G. C. G. Skinner, E. I. Andritsos and A. T. Paxton, *Proc. R. Soc. A.* **476**, 20200319 (2020)

[282] A. Breidi, J. D. T. Allen and A. Mottura, *Materialia* **35**, 102080 (2024)

[283] X. Zhang, B. Grabowski, F. Körmann, A. V. Ruban, Y. Gong, R. C. Reed, T. Hickel and J. Neugebauer, *Phys. Rev. B* **98**, 224106 (2018)

[284] R. J. Elliott, *Phys. Rev.* **124**, 346–353 (1961)

[285] M. E. Fisher, W. Selke, *Phys. Rev. Lett.* **44**, 1502–1505 (1980)

[286] G. S. Zhdanov, Z. V. Minervina, *C. R. Acad. Sci. URSS* **48**, 182–184 (1945)

[287] G. S. Zhdanov, Z. V. Minervina, *J. Phys. USSR* **10**, 422–424 (1946)

[288] M. E. Fisher, W. Selke, *Philos. Trans. R. Soc. London A* **302**, 1–44 (1981)

[289] P. M. Duxbury, W. Selke, *J. Phys. A: Math. Gen.* **16**, L741–L746 (1983)

[290] P. Bak, J. von Boehm, *Phys. Rev. B* **21**, 5297–5308 (1980)

[291] J. B. Thompson, in *Structure and Bonding in Crystals. II*, edited by M. O'Keeffe and A. Navrotsky, pp. 167–188, Academic Press, New York (1981)

[292] G. D. Price, J. Yeomans, *Acta Crystallogr. B* **40**, 448–454 (1984)

[293] H. Horiuchi, M. Akaogi, H. Sawamoto, *Adv. Earth Planet. Sci.* **12**, 391–395 (1982)

[294] B. G. Hyde, T. J. White, M. O'Keeffe, A. W. S. Johnson, *Z. Kristallogr.* **160**, 53–62 (1982)

[295] C. B. Ma, *Contrib. Mineral. Petrol.* **45**, 257–279 (1974)

[296] M. Akaogi, S. Akimoto, K. Horioka, K. Takahashi, H. Horiuchi, *J. Solid State Chem.* **44**, 257–267 (1982)

[297] G. D. Price, *Phys. Chem. Miner.* **10**, 77–83 (1983)

[298] R. M. Hornreich, *J. Magn. Magn. Mater.* **15-18**, 387–388 (1980)

[299] H. De Raedt, B. De Raedt, *Phys. Rev. B* **19**, 2585–2596 (1979)

[300] W. Selke, *Z. Phys. B* **27**, 81–86 (1977)

[301] A. Wiedenmann, P. Burlet, H. Scheuer, P. Convert, *Solid State Commun.* **38**, 129–132 (1981)

[302] S. Gao, L.-F. Lin, P. Laurell, Q. Chen, Q. Huang, C. dela Cruz, K. V. Vemuru, M. D. Lumsden, S. E. Nagler, G. Alvarez, E. Dagotto, H. Zhou, A. D. Christianson, M. B. Stone, *Phys. Rev. B* **109**, L020402 (2024)

[303] A. B. Cairns, M. J. Cliffe, J. A. M. Paddison, D. Daisenberger, M. G. Tucker, F.-X. Coudert and A. L. Goodwin, *Nat. Chem.* **8**, 442–447 (2016)

[304] S. J. Hibble, G. B. Wood, E. J. Bilbé, A. H. Pohl, M. G. Tucker, A. C. Hannon and A. M. Chippindale, *Z. Kristallogr.* **225**, 457–462 (2010)

[305] G. A. Bowmaker, B. J. Kennedy and J. C. Reid, *Inorg. Chem.* **37**, 3968–3974 (1998)

[306] S. J. Hibble, S. M. Cheyne, A. C. Hannon and S. G. Eversfield, *Inorg. Chem.* **41**, 1042–1044 (2002)

[307] S. J. Hibble, A. C. Hannon and S. M. Cheyne, *Inorg. Chem.* **42**, 4724–4730 (2003)

[308] M. Žukovič and T. Idogaki, *Physica B* **329–333**, 1055–1056 (2003)

[309] A. M. Chippindale, S. J. Hibble, E. J. Bilbé, E. Marelli, A. C. Hannon, C. Allain, R. Pansu and F. Hartl, *J. Am. Chem. Soc.* **134**, 16387–16400 (2012)

[310] S. Hibble, A. Chippindale, A. Pohl, A. Hannon, *Angew. Chem. Int. Ed.* **46**, 7116–7119 (2007)

[311] A. L. Goodwin, M. T. Dove, A. M. Chippindale, S. J. Hibble, A. H. Pohl, A. C. Hannon, *Phys. Rev. B* **80**, 054101 (2009)

[312] E. H. Wolpert, *Structural Analogues of Complex Magnetic Phases*, D.Phil. thesis, University of Oxford (2020)

[313] Y. Zhou, W. Zhang, E. Ma, V. L. Deringer, *Nature Electronics* **6**, 746–754 (2023)

[314] T. C. Nicholas, A. E. Stones, A. Patel, F. M. Michel, R. J. Reeder, D. G. A. L. Aarts, V. L. Deringer, A. L. Goodwin, *Nature Chemistry* **16**, 36–41 (2024)

A Appendix

A.1 Cyanospinel Rietveld Refinements

Table A.1: Crystallographic parameters for the cubic $Fd\bar{3}m$ structure of $K_2Zn(CN)_4$ at room temperature from the Rietveld fits in Chapter 3.

a (Å)	12.5484(1)			
α (°)	90			
V (Å^3)	1975.91(1)			
Z	8			
Space group	$Fd\bar{3}m$			
Atom	x	y	z	U_{iso} (Å^2)
Zn	0	0	0	0.0008(6)
K	0.625	0.625	0.625	0.0008(6)
C	0.3801	0.3801	0.3801	0.071(3)
N	0.3827	0.3827	0.3827	0.071(3)

Table A.2: Crystallographic parameters for the cubic $Fd\bar{3}m$ structure of $Rb_2Zn(CN)_4$ at room temperature from the Rietveld fits in Chapter 3.

a (Å)	12.9092(2)			
α (°)	90			
V (Å^3)	2151.30(1)			
Z	8			
Space group	$Fd\bar{3}m$			
Atom	x	y	z	U_{iso} (Å^2)
Zn	0	0	0	0.0346(5)
Rb	0.625	0.625	0.625	0.0578(5)
C	0.3398(3)	0.3398(3)	0.3398(3)	0.061(2)
N	0.3916(2)	0.3916(2)	0.3916(2)	0.061(2)